Three - Phase Slim DC - Link PMSM/SynRM Sensorless Drive

Yang, Feng

DOI (link to publication from Publisher):
10.5278/vbn.phd.eng.00016

Publication date:
2017

Document Version
Publisher's PDF, also known as Version of record

THREE-PHASE SLIM DC-LINK PMSM/SYNRM SENSORLESS DRIVE

BY
YANG FENG

DISSERTATION SUBMITTED 2017

AALBORG UNIVERSITY
DENMARK

Three-Phase Slim DC-Link PMSM/SynRM Sensorless Drive

by

YANG FENG

A Dissertation Submitted to
the Faculty of Engineering and Science at Aalborg University
in Partial Fulfillment for the Degree of
Doctor of Philosophy in Electrical Engineering

AALBORG UNIVERSITY
DENMARK

October 2017

Dissertation submitted

Dissertation submitted: 2017. October. 27

PhD supervisor: Prof. Frede Blaabjerg
Aalborg University

Co-supervisors: Associate Prof. Xiongfei Wang
Aalborg University

Associate Prof. Pooya Davari
Aalborg University

PhD committee: Associate Professor Erik Schaltz
Aalborg University

Professor Jiabin Wang
University of Sheffield

Professor Bojoi Iustin Radu
Politehnico Torino

PhD Series: Faculty of Engineering and Science, Aalborg University

Department: Department of Energy Technology

ISSN (online): 2446-1636
ISBN (online): 978-87-7210-096-8

Published by:
Aalborg University Press
Skjernvej 4A, 2nd floor
DK – 9220 Aalborg Ø
Phone: +45 99407140
aauf@forlag.aau.dk
forlag.aau.dk

Printed in Denmark by Rosendahls, 2017

Abstract

Variable speed drive with low cost diode rectifier has been widely used in many applications, which may significantly increase grid current harmonics. On another side, the low power motor drive makes up the largest market share, where the physical cost is one of the key concerns besides the reliability. With this end, the scheme of slim dc-link motor drive has been attracted many attentions. However, the slim dc-link drive suffers from instability and harmonics issues, especially when fed by a soft grid condition. Literature survey shows that most of the works are carried out to study active damping control to solve the instability issue but only few researches have discussed the harmonics issue related to this. Moreover, most of studies are based on sensor control, and very few have considered the sensorless control.

The aim of the PhD project is to estimate the effect of distorted dc-link voltage, and to determine how to solve both challenging issues, i.e., system instability and harmonic issues, in a sensorless controlled slim dc-link drive. To this end, three main research questions are defined: 1) What are the mechanisms of the active damping control to affect the two aforementioned issues? 2) What is the influence by using the sensorless control, or what is the system mathematic model under sensorless control? 3) Also, how to solve the two challenge issues completely without deteriorating the motor torque and speed performance?

These research questions are answered through theoretical analysis, experimental tests and simulations. Chapter 2 gives an overview of the state-of-the-art active damping control methods. Chapter 3 develops a general mathematical model for the sensor controlled motor drive system by using the principle of transfer function matrix. Chapter 4 investigates the active damping control for the slim dc-link motor drive system with reference to the above mentioned technique challenges, and demonstrates the corresponding pros and cons. The first question is answered in this chapter. Chapter 5 proposes a mathematic model for the sensorless controlled slim dc-link motor drive as well as investigates the active damping control based on the obtained model. In this process, both the first and second research questions are discussed simultaneously. Chapter 6 proposes an active circuit scheme for the sensorless controlled slim dc-link drive. The principle is discussed, and verified by simulation results for answering the third research question.

On this basis, it is recommended that the active damping control can be used where a moderate shaft performance is required but with a strong grid condition, while the proposed active circuit scheme can be used where the high shaft performance is required. Further research could be done to identify other potential constraints or other improved solutions for the sensorless controlled slim dc-link drive. It is concluded finally that new solutions have been achieved to accommodate the slim dc-link drive.

Dansk Resume

Variabel hastighedsdrev med lavkostdiode-ensretter har været meget anvendt i mange applikationer, hvilket kan øge strømforbrugets harmoniske strømforbrug væsentligt. På en anden side gør lavmotormotordrevet den markedsandel, hvor den fysiske pris er en af de vigtigste bekymringer Udover slutningen blev ordningen med slanke dc-link-motordrev foreslået. Imidlertid lider den slanke dc-linkdrev det aktuelle problem og indgangsstrøm harmoniske problem, især fodring med en blød gittertilstand. at de fleste af værkerne udføres for at studere aktiv dæmpningskontrol for at løse det aktuelle problem, men kun et par undersøgelser er implementeret for harmonikaspørgsmålet. Desuden er de fleste af undersøgelserne baseret på den sensorerede kontrol, og meget få anser den sensorløse kontrol.

Formålet med ph.d.-projektet er at estimere effekten af forvrænget DC-spænding og at bestemme, hvordan man løser både udfordrende problemer, dvs. ustabiliteten og harmonikken i en sensorløs styret slank DC-drev. Med henblik herpå raffineres tre hovedforskningsspørgsmål som følger: 1) Hvad er mekanismen for den nyeste aktive dæmpningskontrol for at påvirke de to ovennævnte problemer? 2) Hvad er systemmatematisk model under sensorløs kontrol? 3) Hvordan løser de to udfordringsproblemer helt uden at forringe motorens drejningsmoment og hastighed ydeevne?

Disse forskningsspørgsmål besvares gennem den teoretiske analyse og de eksperimentelle test eller simulering. Kapitel 2 giver et overblik over de nyeste aktive dæmpningskontrolmetoder. Kapitel 3 udvikler en generel matematisk model til det sensorstyrede motordrevne system ved at anvende princippet om overføringsfunktionsmatrix. Kapitel 4 undersøger den aktive dæmpningskontrol for det slanke dc-link motordrevsystem med henvisning til ovennævnte teknikproblemer og viser de tilsvarende fordele og ulemper. I dette kapitel besvares det første spørgsmål. Kapitel 5 foreslår en matematisk model for det sensorløse styrede slanke dc-link motordrev for det første. Herefter undersøger den den aktive dæmpningskontrol baseret på den opnåede model. I denne proces er det 2. forskningsspørgsmål løst. Kapitel 6 foreslår et aktivt kredsløbsskema for det sensorløse styrede slanke dc-linkdrev. Princippet er udkastet diskuteret, og de verificerede simuleringsresultater er vist, at det tredje forskningsspørgsmål besvares.

På denne baggrund anbefales det, at den aktive dæmpningskontrol kan anvendes, hvor den moderate aksel ydeevne er påkrævet, men med en stærk gittertilstand, mens det foreslåede aktive kredsløbsskema kan anvendes, hvor højaksel ydeevne er påkrævet. Yderligere forskning kunne implementeres for at identificere de andre potentielle begrænsninger eller andre forbedrede løsninger til det sensorløse styrede slanke dc-linkdrev. Det ville give meget hjælp til hele drevsystemet ydeevne og muligheden for at blive udbredt.

Acknowledgements

I would like to thank my supervisor Prof. Frede Blaabjerg for the continuous support and guidance, also his patience to comment all of the papers and the thesis.

I would like to thank my co-supervisors, Assoc. Prof. Xiongfei Wang and Dr. Pooya Davari, for the useful discussion and review. Also, I would like to thank Assoc. Prof. Kaiyuan Lu, Assoc. Prof. Laszlo Mathe for the valuable discussion, Dr. Dong Wang for the great discussion and help during the research, Dr. JunBum Kwon for great help in the harmonic state-space model.

I also would like to give thanks to my committee members, Associate Professor Erik Schaltz, Professor Jiabin Wang and Professor Bojoi Iustin Radu, for the valuable comments.

I would like to thank Dr. Haofeng Bai, Dr. Zi'an Qin, and Dr. Chuan Xie for the good discussion on the control, thank Prof. Stig Munk-Nielsen and Prof. Francesco Iannuzzo for knowledge sharing of the IGBT power module. I also would like to thank PhD Qian Wu, PhD Hechao Wang for the discussion on the motor and the office roommate joys. I give thanks to associate Prof. Huai Wang, Doc. Yongheng Yang, Doc. Dongsheng Yang for the helps, and also to all the research group members. Moreover, I give thanks to Ms. Tina Larsen, Ms. Corina Busk, and Ms. Hanne Munk Madsen for the department matters. Also, thanks to the colleagues in the Department of Energy Technology for the friendly work environment.

Thank my friends in Danfoss PE, Ulrik Jæger and Henrik Lorenzen, for the technical and local culture discussions, and continuous encouragement. Also, I give thanks to my friends, Assoc. Prof. Wei Fan, Dr. Lishuai Jing, Dr. Xiaoxu Zhang, Dr. Xiaodong Duan, Dr. Yanbo Wang, Assoc. Prof. Yongming Xia, and Dr. Dao Zhou, and some friends in China for their concern.

Finally, I give special thanks to my family, particularly to my wife Jie for the consistent encouragement and support, and my son for our cheering and laughing.

Table of contents

List of figures

List of tables

Chapter 1. Introduction

This chapter firstly discusses the background of this research project, followed by its scope and objectives. In addition, the thesis organization is outlined to give a better overview about the flow of this research work.

1.1. Background

A variable speed drive (VSD) is an electronic unit which can adjust the speed and torque to meet shaft load demands of an electric motor. Apart from that, the drive system helps to save energy. Driven from the stringent regulations of carbon emission, industrialization and increasing urbanization, the ac motor drive market is expected to continuous growing strongly in the following years. According to the market research [54], the ac motor drive market is forecasted to grow with a rate of 7.0% from 2016 to 2021, i.e. from around $ 15.72 Billion in 2016 to $ 22.07 Billion in 2021. The main applications include compressor, fans, pumps, conveyors and extruders. The low power drive below 40 kW will make up the largest chunk of the market.

In conventional three-phase VSD systems, the general structure includes a diode rectifier stage with a dc-link stage, followed by an inverter, as shown in Figure 1-1. The choke(s) can be located in the dc-side or ac-side of the diode rectifier. A large electrolytic aluminum capacitor tank is employed to obtain a low ripple dc-link voltage. This structure is still widely used due to the low cost diode rectifier.

However, because of the nonlinear characteristic of diode rectifier, the ac-side current are thus far from sinusoidal [2] which may lead to harmonic distortion. Its value can be estimated from the relationship between the power factor (PF), total harmonic distortion (THD_i) of the input current, and the displacement angle ϕ, as given in (1.1). It can be seen that the PF is decided by the value of $\cos\phi$ and THD_i.

$$PF = \cos\phi \frac{1}{\sqrt{1 + THD_i^2}} \tag{1.1}$$

The smoothing function of dc-choke has a high impact on the harmonic performance of the input current, as shown in Figure 1-2 [4]. It shows the system PF and THD_i are improve along with the dc-choke inductance increasing. Moreover, the shape input current waveform gradually changes from the pulse, the saddle, to the square-wave ultimately. In the end, the conduction angle of each phase current will reach to $2\pi/3$, the displacement angle will be close to zero (q.v.(1.1) when $cos\,\phi = 1$), and THD_i will be reduced down to 30% [5], [6], which is very close to the results in Figure 1-2. It also can be seen that when increasing the dc-choke value linearly even nonlinearly [7], [8], it gives benefits to reduce the harmonic distortion, but only helps slightly to increase the power factor.

When a large amount of VSD is operated, a large amount of harmonics distortion will be produced which are harmful for the grid like the power loss increasing, or signal interference [3]. Meanwhile, the PF goes down so that a high power rating transformer is required. Therefore, the international standards on harmonic distortion limitation have been presented as the access criteria for many national and regional market, such as IEC 61000-3-2 with input current > 16 A, IEC 61000-3-12 with input current > 16 A and ≤ 75 A, or IEEE-519 (defined the THD requirement of mains voltage).

1.2. Scheme to Improve Harmonic Performance

To obtain a high harmonic performance, quite a number of methods have been proposed by introducing an active power stage feasible for the motor drive system. Typically, the input current under some of these schemes is improved to be sinusoidal, or quasi-sinusoidal, or square waveform [9]. While, a low cost and easy applicable scheme is desired to improve the input current quality of the three-phase VSD. For some moderate requirement applications, the saddle input current still be a feasible solution due to low cost. For high-end application, the sinusoidal input current is an ideal target but the cost will be extravagant. The square-wave input current is a compromise between the input current quality and the cost.

In this section, three types of well-known scheme are discussed according to their operation principle and the complexity, which are: (1) three-phase PWM Rectifier, (2) (hybrid) harmonic injection, (3) electronic (smoothing) inductor.

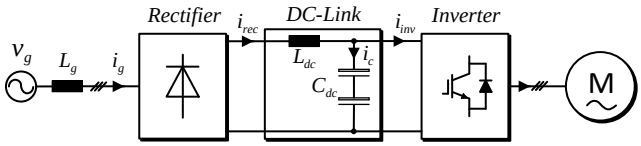

Figure 1-1 General block diagram of a conventional drive system

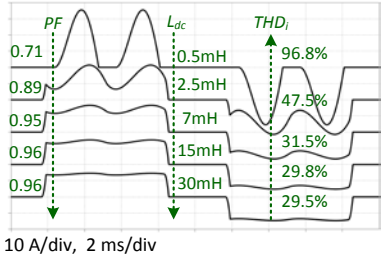

Figure 1-2 Input current impacted by different dc-choke value in a conventional drive [4].

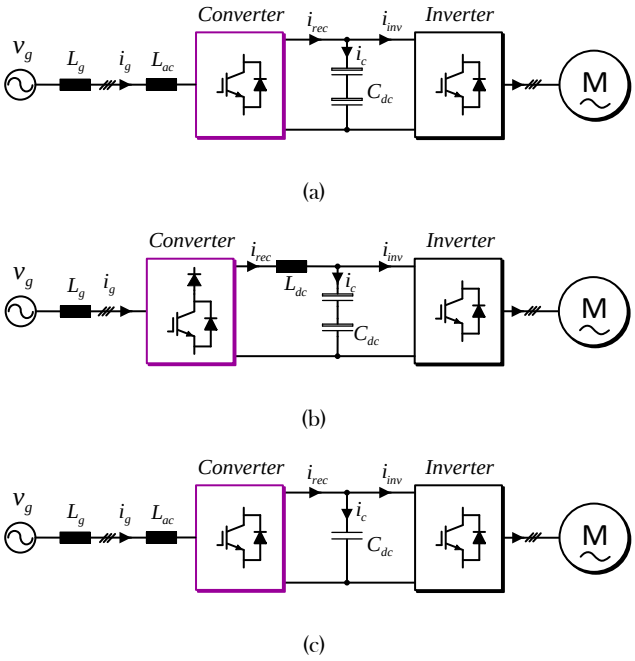

Figure 1-3 Basic circuit topologies of three-phase PWM rectifier in a drive system. (a) Boost-type. (b) Buck-type. (c) Boost-type with a small dc-link capacitor

1.2.1. Three-Phase PWM rectifier

For high power and high performance applications, this scheme is desired by using three-phase pulse width modulation (PWM) rectifier to replace the diode rectifier, so that the sinusoidal input current can be obtained. The basic principle is shown in Figure 1-3 (a) and (b), where the topology of a front-end PWM rectifier can be employed by a Boost-type circuit [10]-[12] or Buck-type circuit [13]-[15]. The power flow can be easily realized to flow bi-directional if using the Boost-type topology. Reversal of the power flow direction also can be implemented in the Buck-type topology PWM rectifier, but some modifications needs to be done [16].

As stated in [17], the benefits by using Buck-type rectifier include the inherent short-circuit protection, simple inrush current control and regulated step-down output voltage. However, in contrast, Boost-type circuit is usually used due to the high efficiency, low input current distortion, and low EMI emissions [17]. Besides the regulator the output voltage (or dc-link voltage) under power control theory [18], the PWM rectifier can minimize the input current harmonics. Some typical control methods can be adopted, such as the resonant controller [11], the repetitive controller [12].

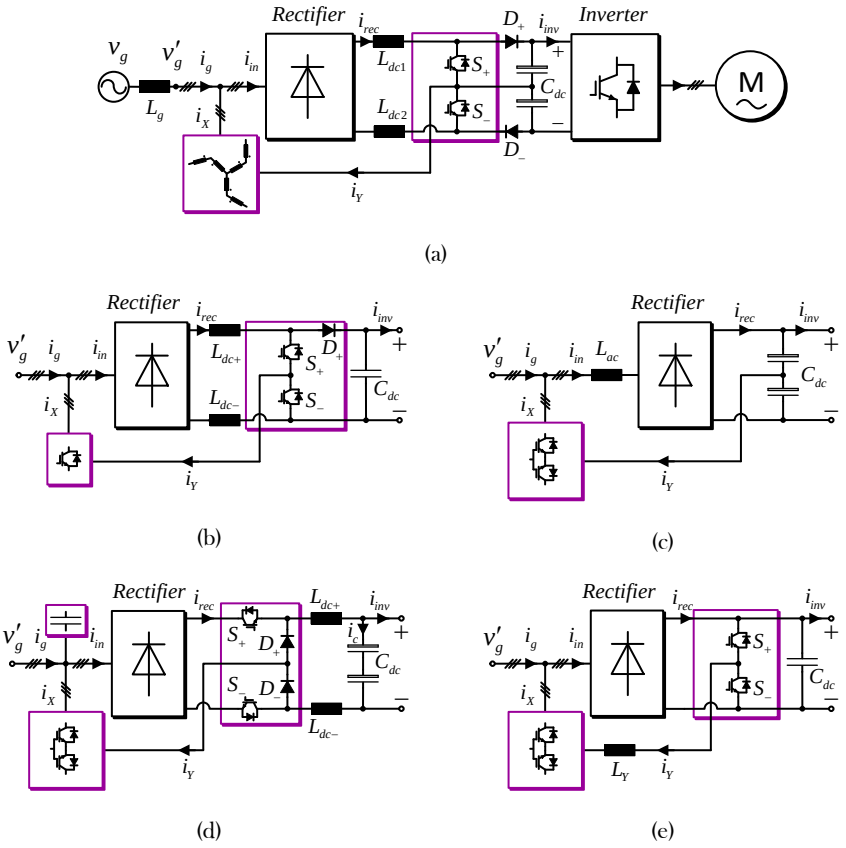

Figure 1-4 Basic circuit of harmonic injection scheme. (a) Basic Minnesota rectifier [27]. (b) Basic dual-Boost rectifier [29]. (c) Basic Vienna rectifier [30]. (d) Basic Swiss rectifier [31]. (e) Basic Korea rectifier [32].

It is worth to remind that in the three-phase Boost-type rectifier, the attention needs to be paid to the turn-on losses of the switches and the severe recovery problem suffered by the diode [17]. Thanks to the soft switching technique, this issue can be alleviated by using either the zero-voltage transition (ZVT) technique for the unidirectional power flow application [19], or the three-phase ZVT technique for the bidirectional power flow application [20]. In addition, with the emerging of wide band-gap material, the silicon carbide (SiC) switches and diode can be employed as an optional method to relieve this issue and to improve the system efficiency [20].

Considering the electrolytic capacitor in dc-link is bulky and costly, a feasible control strategy was proposed in order to reduce the charge/discharge current of the dc-link capacitor. Thereby, the electrolytic capacitors can be replaced by the film capacitor with a small capacitance [22], [23]. In the meantime, the benefits of PWM rectifier

can still be kept, such as a good input harmonic performance, a regulated dc-link voltage and the capability of bidirectional power flow.

Regarding shortcomings in the PWM rectifier, the high cost, complicated control strategy, efficiency and electromagnetic interference (EMI) [24] are deserved concerns.

1.2.2. (Hybrid) Harmonic Injection

The scheme started to attract high interest after the Minnesota rectifier [25] was presented in 1992. It improves the input current to be sinusoidal or quasi-sinusoidal. Following this passive third harmonic scheme, some hybrid harmonic injection schemes have also been proposed. The basic circuits are shown in Figure 1-4 (a).

It can be seen from the input current waveforms in Figure 1-2 that there is no current flowing in some time intervals in a fundamental frequency cycle. The basic idea of the passive third harmonic injection of Minnesota rectifier is to inject the third harmonic to patch the input current [25]-[27]. The injection current i_Y is produced from a network composed by active switches (q.v. Figure 1-4 (a), the S1 and S2), then injected into the input current in front of diode rectifier via an injection network, such as the Zig-Zag transformer as shown in Figure 1-4 (a). In this way, the input current becomes quasi-sinusoidal (cf. Figure 5-10 in [5]). One of the shortcomings of the passive injection network is that it shows a relatively large volume and weight. Another shortcoming is the injected third harmonic current increases the current stress of the dc-link capacitor, so that the lifetime of aluminum electrolytic capacitor becomes worse [28].

Some other attractive injection methods have also been presented in recent decades, which are known as the dual-boost rectifier [29], followed by the Vienna rectifier [30], the Swiss rectifier [31], and the Korea rectifier [32]. In these active injection networks, only the method of dual-boost rectifier uses the unidirectional switches, the other three adopt the bidirectional switches. In these topologies, the Swiss rectifier can step down the rectified voltage. The Korea rectifier is the one using a slim dc-link capacitor, although it cannot regulate the output dc voltage.

One concern of the harmonic injection scheme is the complicated control strategy due to a high number of introduced active switches. Also, these power switches are closed to the grid, the EMI filter thus needs a careful design [6], [33].

1.2.3. Electronic (Smoothing) Inductor

Besides the manipulation in the ac-side of rectifier, it is possible to modify the ac-input current by properly controlling the dc-link current. The typical example is the so-called electronic (smoothing) inductor (EI/ESI) technique. It is realized by introducing

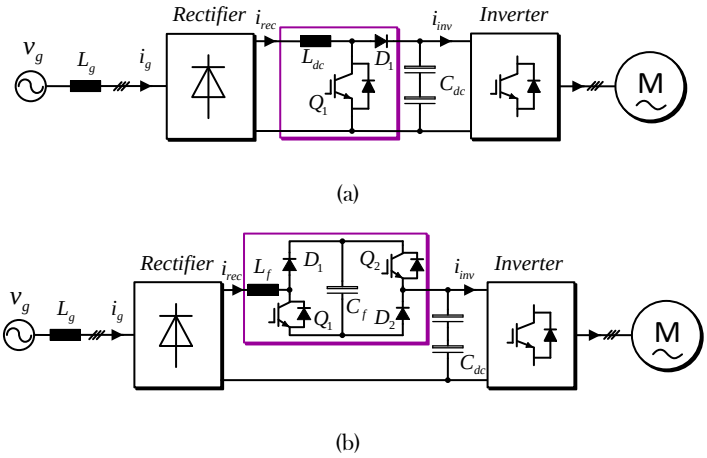

Figure 1-5 Principle of electronic (smoothing) inductor (EI/ESI) scheme.

(a) EI with a Boost converter (CCM). (b) ESI with an Asymmetry Half-Bridge.

a dc-dc power converter to emulate a dc-choke with infinite value [4], [37]. Thereby, the resulting input current is a square-wave shape as in above discussion.

Specifically, the Electronic Inductor (EI) scheme [4] is realized by combining a three-phase diode rectifier with a Boost converter [34], whose principle circuit is shown in Figure 1-5 (a). The Boost circuit operates at Continuous Conduction Mode (CCM), and the dc-link is mapped with $2\pi/3$ input current via the switching function of the diode rectifier [34]. A verified example by using such EI scheme in the motor drive can be found in [35], where the THD and PF of the resulting input current will be 29% and 0.95 respectively, which is close to the value as mentioned above. In addition, another benefit by using EI is the controllable output dc voltage, although it is always higher than the rectified voltage.

Interestingly, if extending to a three-level Boost topology [4], [34], [36], the voltage stress becomes half so that the lower voltage rating power switches can be chosen. Also, it doubles the switching frequency on the inductor L_{dc}, and a lower inductor current ripple is obtained.

An alternative way to modify the dc-link current is to use the electric smoothing inductor (ESI) scheme proposed in [37], as shown in Figure 1-5 (b). An asymmetric Half-Bridge (HB) circuit is used to emulate the passive dc-choke in the conventional drive. In this ESI scheme, the resulting PF and THD_i are same as above, but the voltage stress in this active circuit is much lower (40-60V) [9]. Besides, the HB is allowed to run at high switching frequency to reduce its total size further [37].

The potential drawback of the EI is: (1) the high power loss due to the operation is processed in the whole power flow routine; (2) the turn-on loss for the main switch

and reverse recovery of rectifier diode D_1 needs to be paid more attention to. While, the disadvantages of the ESI are: (1) a large capacitor C_f is needed even compared with dc-link capacitor [4]; (2) the current THD is highly influenced by the grid impedance [4]; (3) the voltage utilization of the motor drive is lower than the conventional drive due to the voltage drop on the ESI [9].

1.2.4. Other Schemes

It is true that there are other solutions to settle the harmonics issue from grid side, such as the passive harmonic filters [38], the active power filter (APF) [39], but they are usually costly so they will not be discussed in the thesis.

1.3. Metallized Polypropylene Film Capacitors

On the other hand, reliability is also highly important to be considered in terms of motor drive application. The above mentioned schemes to improve the harmonics performance are carried out in the conventional VSD together with the relatively large aluminum electrolytic dc-link capacitors. Besides the large dimension and high cost, another inevitably weakness is the low lifetime electrolytic capacitor which determines the whole VSD system reliability performance. According to an industry-based survey [40] and a practical drive design [41] show that the aluminum electrolytic capacitor in dc-link ranks as the second most fragile component, following the first most fragile component which is the power devices. However, with the technology improvement on the power device [42], [43], the package [44], [45] and the thermal-process material [46], the reliability of power device is significantly boosted. Therefore, the weakness of electrolytic capacitor used in the dc-link remains a prominent concern in the motor drive.

Figure 1-6 shows the three types of common used commercial capacitor in the motor

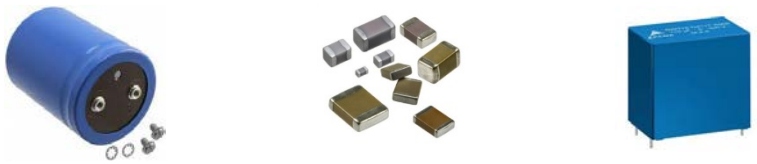

(a) (b) (c)

Figure 1-6 Commercial capacitor candidates. (a) Aluminum cap. (Al-caps). (b) Multi-Layer Ceramic cap. (MLC-caps). (c) Metallized Polypropylene Film cap. (MPPF-caps).

Note: pictures are obtained from the websites,

(a) https://i.stack.imgur.com/dVltg.png.
(b) https://diychip.ru/1uf_500v_smd.
(c) https://en.tdk.eu/blob/168386/a4af8a383cf10be157ef96b721081d8c/epcos-film-mkp-hd-with-new-voltages-produktbild-HighResolutionData.jpg.

Table 1-1 Comparison of three types of capacitors [48]

	Capacitance	Voltage	Ripple current	ESR and DF	Freq. range	Cap stability	Volt. derating	Temperature	Reliability	Energy density
Al-caps	++	+	−	−	−	+	+	+	−	++
MLC-caps	−	−	+	+	++	−	−	++	++	+
MPPF-caps	+	++	++	++	++	++	++	−	+	−

(Note: + means good, ++ means very good, - means bad.)

drive application. Table 1-1 shows a performance comparison between the aluminum capacitor (Al-cap), multi-layer Ceramic capacitor (MLC-cap), and the metallized polypropylene Film Capacitors (MPPF-cap). The MLC-caps have smaller size and wide operation frequency range. But this type of capacitor has high cost and mechanical sensitivity [48], and is thus not considered in the application of dc-link capacitor. By comparison, the Al-cap has the highest energy density but also the highest ESR, and low ripple current processing capability. The film capacitor has the compromised performance with low ESR so that it can easily tolerate larger current ripple. In addition, the cost of film capacitor is only 1/3 of Al-cap in terms of ripple current (USD/A) [49].

1.4. Scope and Objectives

A sinusoidal input current is desired in a motor drive, but the cost will be a challenge. Indeed, a square-wave or a saddle-wave input current is enough in most applications if only with moderate requirement. For instance, the current distortion for an industrial motor drive is 48% and 46% in terms of THD and partial weighted harmonic distortion (PWHD) according to the requirement in IEC 61000-3-12. Therefore, it is meaningful to find a low cost, high reliability motor drive solution for this kind of applications. The slim dc-link motor drive is thus chosen as the target in this research project.

The motor drive using the film capacitor is referred to as the slim or small dc-link drive [50] whose principle diagram is shown in Figure 1-7. Similar as the EI/ESI

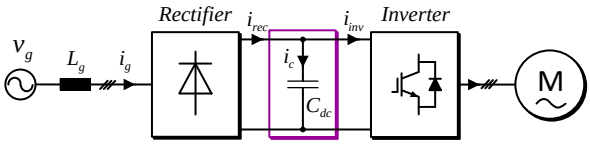

Figure 1-7 General block diagram of a conventional drive system

scheme, the slim dc-link drive also modify the dc-link current to improve THD_i but by using a film capacitor with very low capacitance. Based on this principle, some industrial products have already been available in the market [52], [53].

However several technical issues are resulted in such kind of drive system after using a film capacitor in the dc-link. Extensive research on the slim dc-link drive have been done, however, few comprehensive theoretical analysis and complete solutions have been given to the critical technique issues regarding the harmonic performance and system stability.

This dissertation will address the practical challenges of slim dc-link drive with special focus on the system instability and harmonics performance, especially considering the effect of a soft grid condition (or large grid inductance), which is common in the real applications due to the long power cables together with a large power transformer impedance. The obtained results from both theoretical analysis and its relevant laboratory experiment will provide a good insight into the impact by the introduced film capacitor. Furthermore, a new methodology will be presented with reference to state-of-the-art active damping control methods to stabilize such a drive system under sensored control. In addition, the proposed methodology is applied to a drive system under sensorless control through introducing a sensorless controlled system model which has never been investigated before. Finally, to solve the above mentioned challenging issues thoroughly, the principle of a new solution will be briefly discussed, as well as part of the verified results will be shown.

1.4.1. Hypotheses

The theoretical analyses are performed under the following hypothesis:

- The fundamental frequency of low voltage distribution network is 50Hz. Therefore the frequency range of the harmonic analysis is [50, 2000] Hz.
- The power losses of the drive system are neglected.
- The voltage modulation index is in the linear zone, and the nonlinearity of PWM switching of the inverter is omitted.

1.4.2. Scope

This project studies a cost-effective and high reliable three-phase low voltage electrical motor drive system equipped with a film capacitor in the dc-link. The synchronous reluctance machine (SynRM) is used for the theoretical analysis and experiments. The obtained analysis results can easily be extended to the permanent magnet synchronous machine (PMSM) drive system, as well as the induction machine drive system. A field oriented control (FOC) algorithm is adopted in the slim dc-link motor drive.

1.4.3. Objective

The main objectives of this project are based on above hypothesis:

1) The introduced film capacitor leads to a large voltage variation in the dc-bus, how does the voltage variation impacts the drive system stability performance?
2) The introduced film capacitor adversary affects the grid current harmonics performance in the case of a large grid inductance, what is the mechanism?
3) Using active damping control can improve such slim dc-link drive performance, what are the pros and cons under the sensored control and the sensorless control respectively?
4) Is there any possible method to overcome the disadvantage of active damping control, feasible for the slim dc-link drive?

1.5. Thesis Organization

The thesis is organized as follows:

Chapter 1 briefly introduces background, scope and objectives of this research work. Also, the thesis organization is briefly described.

Chapter 2 gives an overview of the studies of the slim dc-link drive. Especially it discusses the critical issues in terms of instability and harmonics. It presents also the state-of-the-art research results, and analyses their pros and cons in brief.

Chapter 3 presents a generalized large-signal modeling method for the drive system by using the concept of transfer function matrix. In this model, besides the equal bandwidth, it also considers the case of two different bandwidth of the dq-axis current controllers. Subsequently, based on the obtained model, some practical issues are discussed with respect to the current and speed controller design.

Chapter 4 deduces a generalized small-signal mathematical model for the slim dc-link drive under sensored control. The proposed model takes into account the impact of the dc-bus voltage, the current loop and the speed loop. Moreover, the state-of-the-art active damping control methods are fully investigated with respect to their impact on the instability and harmonics performance. Also, some practical considerations are discussed.

Chapter 5 proposes a generalized small-signal mathematical model for a sensorless controlled slim dc-link drive. Notably, the modeling process includes the function of a stator flux observer and a phase locked loop (PLL). Thereafter, the influence on the system stability and harmonic issues are estimated comprehensively by both the dc-bus voltage and the active damping control methods.

Chapter 6 proposes an active circuit scheme to solve both challenging issues simultaneously in the slim dc-link drive. The principle is discussed, and some of the verified simulation results are shown as well.

Chapter 7 concludes the research work, and gives some recommendations for future work.

1.6. List of Publications

The scientific papers from this project are listed as given below:

Journal Papers

- **Y. Feng**, D. Wang, F. Blaabjerg, X. Wang, P. Davari, and K. Lu, "Investigation of the active damping control for three phase slim dc-link drive system," to be submitted.

Conference Papers

- **Y. Feng**, D. Wang, F. Blaabjerg, "Input admittance model of sensorless controlled slim dc-link drive," in Proc. IEEE EPE-2018, in review.
- **Y. Feng**, D. Wang, F. Blaabjerg, X. Wang, K. Lu, and P. Davari, "Active damping control for three-phase slim dc-link drive system – overview and investigation," in Proc. IEEE IFEEC-ECCE Asia 2017, pp. 1-6, Jun. 2017.
- **Y. Feng**, J. B. Kwon, X. Wang, and F. Blaabjerg, "Input harmonic analysis of slim dc-link drive using harmonic state space," in Proc. IEEE IFEEC-ECCE Asia 2017, pp. 1-6, Jun. 2017.
- **Y. Feng**, J. B. Kwon, X. Wang, and F. Blaabjerg, "Harmonic coupling analysis of multi-drive system with slim dc-link drive," in Proc. IEEE Ind. Symposium on Ind. Electro. (ISIE), 2017, pp. 1-6, Jun. 2017.
- **Y. Feng**, L. Mathe, K. Lu, F. Blaabjerg, X. Wang, K. Lu, and P. Davari, "Analysis of harmonics Suppression by Active Damping Control on Multi Slim DC-link Drives," in Proc. IEEE IECON-2016, pp. 5001-5006, Nov. 2016.
- M. Laszlo, **Y. Feng**, D. Wang, "Linear modeling of the three-phase diode front-Ends with reduced capacitance considering the continuous conduction mode," in Proc. IEEE IECON-2016, pp. 5007-5012, Nov. 2016.
- D. Wang, K. Lu, P. O. Rasmussen, L. Mathe, **Y. Feng**, "Voltage modulation using virtual positive impedance concept for active damping of small dc-link drive system," in Proc. IEEE ECCE-2015, pp. 20-24, Oct. 2015.

Chapter 2. Overview of Slim DC-link Drive

As mentioned in last chapter, the slim dc-link motor drive is the result of using the film capacitor to replace the electrolytic capacitor [50], and the topology is shown in Figure 2-1. When using the film capacitor, the drive system will be more economical, and more reliable because of the lower power loss in the capacitor due to its low Equivalent Series Resistor (ESR) [48], [54], [55]. When the dc-bus voltage exceeds 550 V, at least two electrolytic capacitors are needed in series to handle the voltage together with balanced resistors, while one standard film capacitor can match this requirement for its much higher rated voltage [55]. Furthermore, the film capacitor is able to handle large current ripples, and without explosion risks [55]. In some cases the choke(s) in the ac- or dc- side and the inrush-current-limitation circuit can be removed. These attracting merits make it possible to realize a compact hardware along with a good thermal design.

Figure 2-2 shows the test results in a 2 kW slim dc-link drive. The input current is a quasi-square-wave, whose THD is around 35.3%. In this drive, only the film capacitor is used in the dc-link, and without any choke at the ac-side or dc-side. Obviously, compare with conventional drive, both the cost, weight and volume of the dc-link can

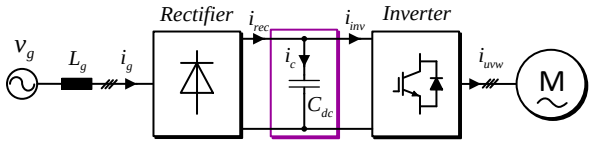

Figure 2-1 Block diagram of a conventional drive system

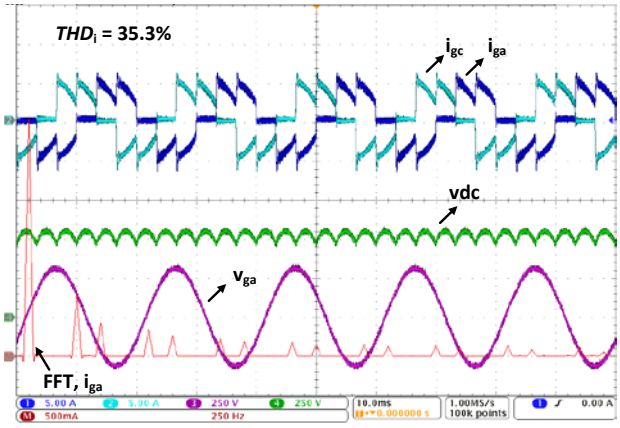

Figure 2-2 Waveform of a slim dc-link drive under ideal grid including spectrum of the current

be reduced [56], therefore the slim dc-link drive may become a competitive candidate.

Over the last three decades, some research efforts have been devoted to slim dc-link motor drive. An over-modulation control method has been presented in [57] to improve the voltage utilization and to achieve a less sensitivity to dc-link voltage. A feed-forward modulation method is investigated by processing the real-time dc-link voltage to improve the input current qualities [58]. A comparison in [59], between slim dc-link drive and conventional drive, gives an overview on the required design considerations in a slim dc-link drive. The slim dc-link drive performance influenced by the unbalanced grid has been studied in [60]. A protection method is proposed in [61] to overcome the over-voltage/current problems in the motor regeneration mode in an electric vehicle application. A field weakening strategy is studied in [62] by decoupling the fluctuation and maximum utilization of the dc-link voltage so that the operating speed can be extended above the base speed without any instability problems.

Besides, some attentions have been paid to the system instability issue in the slim dc-link drive, especially in the case of having large grid impedance (a high L_g as shown in Figure 2-1). However, there is only a few researches turn to the grid harmonic issues in recent years in terms of harmonics issue in the soft grid condition. The following sections will give a brief overview of the state-of-the-art techniques in terms of these two challenging issues in the slim dc-link drive.

2.1. Instability Issue in Slim DC-link Drive

It is a common practice to tightly control the motor drive in order to obtain a high dynamic and good control performance system [63]. Under this situation, the inverter-feed motor load behaves as a Constant Power Load (CPL) and the motor drive will present a Negative incremental Impedance (NI) characteristic which can make the drive system unstable [63], [64]. In order to maintain the CPL, the dc-link current deceases when the dc bus voltage increases, which is main concept behind the NI characteristic [66], [67]. Another factor which is relevant to instability issue is the reduced dc-link capacitance of the film capacitor [68].

This phenomenon can be easily understood from the equivalent second-order circuit as shown in Figure 2-3 (a), where R_g and L_g are the grid resistor and grid inductor separately, and v_{in} is the equivalent voltage source. The dc-link current can be equalized as a current source i_{inv} under the motor controller, as shown in Figure 2-3 (b). Its characteristic equation is expressed in (2.1), and Figure 2-4 shows the system poles change with different values of C_{dc}. It can be seen that the poles tend to enter into the right half plane (RHP) with the gradually decreased C_{dc}, which means the system will become unstable. In reality, thanks to the diode's one-way flow characteristic, this circuit will enter a stable limit cycle but with a large oscillation ripples in the dc-link voltage [60].

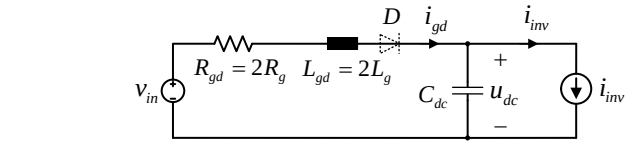

(a)

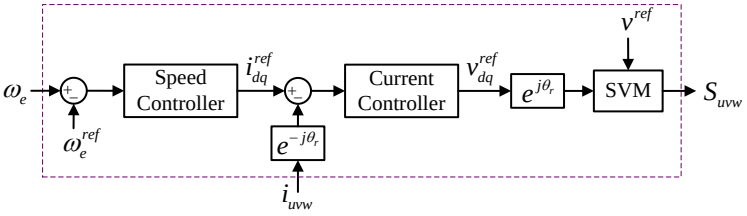

(b)

Figure 2-3 (a) Simplified equivalent circuit model of the drive [68], where the diode D is switched on when the current i_{gd} is positive. (b) Block diagram of the motor controller.

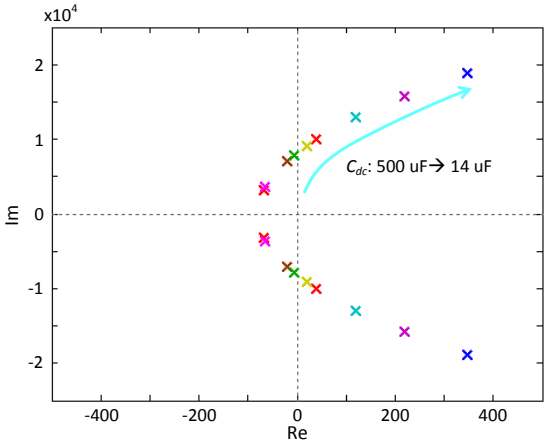

Figure 2-4 Distribution of the system poles with different C_{dc}

$$s^2 + \left(\frac{R_{gd}}{L_{gd}} - \frac{P_L}{C_{dc}U_{dc}^2}\right)s + \frac{1}{L_{gd}C_{dc}}\left(1 - \frac{R_{gd}P_L}{U_{dc}^2}\right) = 0 \qquad (2.1)$$

To overcome the NI based instability issue, one method is to increase dc-link capacitance, which is consistent with the analysis from Figure 2-4. However, it may in turn lead to higher harmonic distortion on the input current, as well as increase the cost, the space and weight. Another technique to make the system stable is to add an adequate damping of the resonance. The passive damping approach [69], [70] could impair the power density, increase the cost, and require parameter tuning under

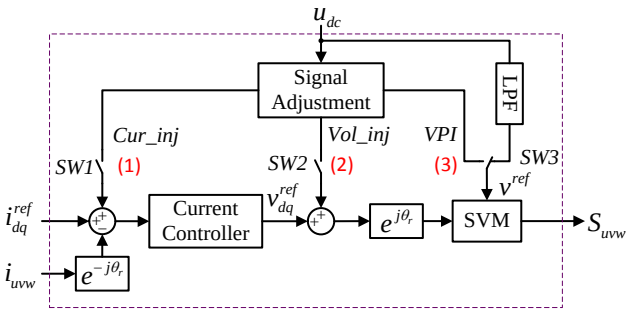

Figure 2-5 Principle to classify the active damping control.

(where i_{uvw} and i_{dq}^{ref} are the motor current and its reference separately, θ_r is the rotor position, u_{dc} is the dc-link voltage, LPF is a low-pass filter, and PWM is the switching logic to the inverter.)

different condition. Therefore the active damping schemes could be more promising, which include both the active damping control scheme and the active circuit scheme.

2.1.1. Active Damping Control

Active damping control, as the name implies, adopts an active signal (dc-bus voltage variation) into the motor controller to stabilize the drive system. According to where to inject the active signal into the motor controller, as shown in Figure 2-5, the active damping method can be divided into three categories: (1) Current (Torque) reference injection (Cur_inj), (2) Stator Voltage reference injection (Vol_inj), (3) PWM reference injection (VPI).

2.1.1.1 Current Reference Injection (Cur_inj)

According to author's knowledge, the first study to use "active damping" control was proposed in a motor drive under Direct Torque Control (DTC) [71]. The basic idea behind this method to compensate the NI instability is to intentionally form a variable power ripple, proportional to the sensed dc-link voltage variation ripple, and superimpose it with the original torque reference. Alternatively, it can be realized as well by sensing the dc-link capacitor current variation in order to obtain the dc-link voltage variation information [72]. In summary, the principle can be intuitively understood by changing the SW1 state to inject the correction term into current reference as shown in Figure 2-5. Note that the correction term is the output of the signal adjustment block (SA).

Later on, [63] set forth an active damping control method in an Induction Motor (IM) drive under FOC in an electric propulsion system. It was implemented through a nonlinear control algorithm to modify the torque reference. Thereby, the effect of this

method is to change the NI characteristic of the inverter into a Positive Impedance (PI) characteristic. This nonlinear active damping control method was further studied in the literature [73]–[75].

In [76], another nonlinear control algorithm was investigated to stabilize the system. This active damping control method was similar with [71] but with tricky manipulation to act as an extra equivalent virtual capacitor on the dc-link. The proposed approach was realized by modifying the torque reference current (i.e. q-axis current reference).

By comparing the relatively complicated nonlinear control algorithm, a simple linear control algorithm was proposed to stabilize the NI instability for a vector controlled traction drive [77]. This stability control strategy is realized by feeding a portion of dc-link voltage variation into the torque reference current to stabilize the system. The intuitive way to understand this idea is that it introduces an extra equivalent virtual positive impedance to mitigate the inherent NI characteristic. Also, [78], [79] applied the same principle to study future on the brushless dc-motor drive and PMSM motor drive respectively.

The common disadvantage of this type of method is the current controller, which may weaken the damping effect when its bandwidth is lower than the slim dc-link resonant frequency [51], [83]-[86].

2.1.1.2 Voltage Reference Injection (Vol_inj)

This approach can be intuitively understood by changing the SW2 state as shown in Figure 2-5. It superimposes the correction term into the *dq*-axis stator voltage reference. Specifically, it can choose either one of the d- and q-axis voltage references or both to inject into.

Following that, the stability of the system was improved by directly injecting the correction term into the *d*-axis voltage reference only [82]. Notably, a high-pass Filter (HPF) was used in SA to remove dc component of the measured dc-link voltage. By comparison, [83] proposed to superimpose the correction term into the *q*-axis stator voltage only, and a band-pass Filter (BPF) is used to obtain the correction term. Thanks to the BPF, the influences on the torque performance and system dynamic become less when using the Vol_inj. An optional Vol_inj method was proposed in [51] by injecting an extra component to the d-axis stator voltage vector, where the superposition component was proportional to the difference between the dc-link voltage and estimated source voltage. In this method, an extra Luenberger-type estimator was needed to estimate the grid voltage and current, so it seems more complicated.

Although the above active damping methods can stabilize the drive system, their performance is significantly dependent on the motor parameters [51], [82], [83] or the

grid parameters [51]. More recently, another Vol_inj method with motor parameter-free was presented in [84]. Similarly, it can be realized by injecting a correction term into either one of the d- and q- axis voltage references or both, without requiring any filtering techniques (i.e. the HPF or BPF).

From the impedance point of view, the above Vol_inj methods are based on adding an equivalent virtual resistance in parallel with the dc-link capacitor [80]-[84], or the grid inductance [51], to enlarge the system damping factor. The limitation of this type of scheme is that the system operating point is dependent on the gain in terms of the sensored dc-link voltage variation.

2.1.1.3 PWM Reference Injection (VPI)

Space vector pulse width modulation (SVM) is often used in the motor drive to produce the switching logic PWM to the inverter. The reference of this PWM block often uses the measured dc-link voltage averaged by an LPF. When using the VPI control, this reference will be modified which can be understood by changing the SW3 state in Figure 2-5.

In the slim dc-link drive, the dc-link voltage consists of at least two groups of signal included, which are the rectifier component and the resonant component. The original idea proposed in [85] to compensate the resonant was realized by reconstructing the measured dc-link voltage, and then sent to PWM block as the reference voltage. The reconstruction process started with the separation of two components via a BPF, and reversed the resonant part by introducing a proper delay, and finally recombined them together. In this method, it requires that the resonant frequency of the resonant component must be two times larger than the frequency of rectifier part, which is also one of the limitations of this method in [85]. Another disadvantage is that the half period time needs to be detected in real time for signal reversing, so that large memory is required.

To overcome these shortcomings, another scheme was proposed in [86] to realize active damping. In this scheme, the dc-link voltage was deemed as a combination of dc and ac component, so that both the signal separation and reconstruction were processed via an LPF. Also, the ac component reversing was realized without resonant frequency detection.

One more of this type of methods by adding damping pulses was presented in [87]. Its purpose was to make the load more like a resistive load when comparing with other methods. The idea is good, however, the control parameter is decided by the system parameter, and more skills are needed when carefully designing the amplitude and width of the damping pulse. In addition, a second-order generalized integrator (SOGI) based frequency-locked loop (FLL) is used so that the complexity of the control is increased.

In summary, the VPI control is actually equivalent to a feedforward compensation control. Its effect is also equivalent to the Vol_inj control when the correction term is injected into both d- and q- axis voltage vector simultaneously, i.e. equivalent to [80]. The disadvantage of VPI is the torque performance is degraded in a certain degree, similar to the two other types of method in this sense.

2.1.2. Active Circuit

In [88], a dc-link shunt compensator was proposed to compensate the diode rectifier current in a slim dc-link drive. This compensator was realized by a Boost converter in parallel with the dc-link capacitor. It operates in CCM so that it can be deemed to equalize a current source. Thanks to the compensator, it can not only make the drive system operate in stable, but it can also obtain a satisfactory grid current harmonic performance.

However, there are still some potential limitations by using this scheme. Besides the increased cost, the input current harmonic performance will be a problem when feeding from large grid impedances and its control strategy is dependent on the system parameters.

2.2. Harmonics Issues and their Analysis

As discussed above, the dc-link voltage is fluctuating in the slim dc-link drive. Similar dc-link voltage variation phenomenon was noticed in a PWM inverter [89] from more than three decades ago, where such fluctuation deteriorates the harmonic performance of the output voltage. The proposed solution is based on feedforward concept to improve the harmonic performance. Soon, a profound theoretical analysis on the feedforward control was given in [90] in terms of its mechanism to reject the dc-link voltage variation, and improve the inverter output-end harmonic performance. Later on, [91] borrowed this control method into a motor drive to deal with both the dc-link voltage variation and inverter nonlinearities simultaneously. Interestingly, these studies are already started to minimize the value of dc-link capacitor thirty years ago.

During the same period, [50] proposed the original slim dc-link drive to improve the grid harmonic performance. As mentioned before, its grid harmonic performance is satisfied in an ideal grid condition (i.e. strong grid). However, the input harmonic performance will become worse in the case of a large grid inductance (i.e. soft grid) [75], [84]-[86]. The reason behind this phenomenon is the slim dc-link drive is much sensitive with respect to the grid impedance [92], [93], and its harmonic characteristic is unpredictable for different R_{sce} [93]. To certain degree, the active damping control, i.e. feed-forward control, can also alleviate the input harmonic distortions while stabilizing the drive system [75], [84]-[86].

Moreover, different power load levels lead to different harmonic emissions [94], [95]. In high load condition, the current harmonic distortion will decrease since the damping effect is increased. In addition, the harmonic performance may also be impacted by the FOC controller bandwidth [95], which will give detailed analysis in later chapters in this thesis.

The following will give an overview of harmonic analysis methods, and schemes to improve the harmonic performance in a slim dc-link drive.

2.2.1. Input Harmonics Analysis Method

In a motor drive, the time-domain method based on software tools are often used, for instance PSpice or Saber [96], [97]. In this way, accurate results can be obtained by using a detailed model. However, a relatively long simulation time and large computer memory are generally required, no matter how accuracy of the analysis.

Another method was proposed based on Fourier or double-Fourier analysis theory [2], [98]–[100]. This frequency domain method is a compromise between calculation time

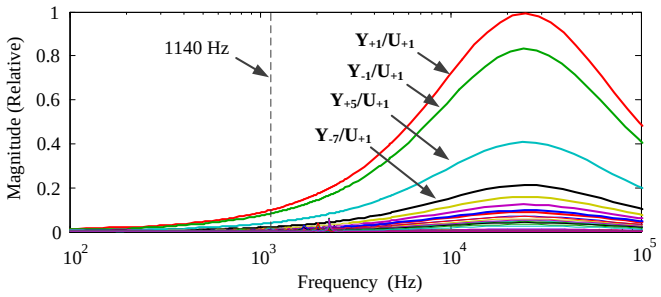

(a)

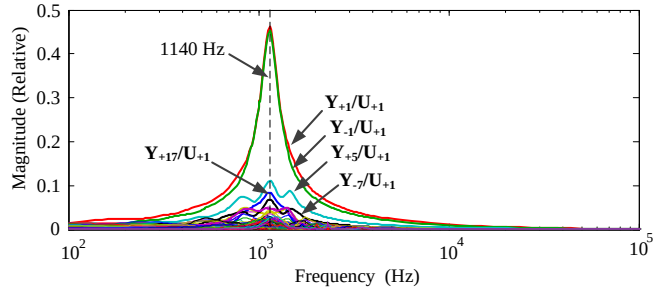

(b)

Figure 2-6 Grid harmonic admittance of slim dc-link drive [92], (a) Without grid impedance. (b) With grid impdeance (0.7 mH).

and accuracy. There are two disadvantages by using this method. The first is that the resulting input current harmonics do not have enough accuracy that the commutation effect in the diode rectifier is omitted. The second is two separated procedures have to be used for two different conduction modes of the diode rectifier (i.e. CCM and discontinuous conduction mode (DCM)).

Furthermore, a dynamic phasor (DP) model is proposed in [101] for the diode rectifier based on the generalized averaging concept [102]. Actually, the DP is the time-varying Fourier coefficient which can give insight into how a specific frequency

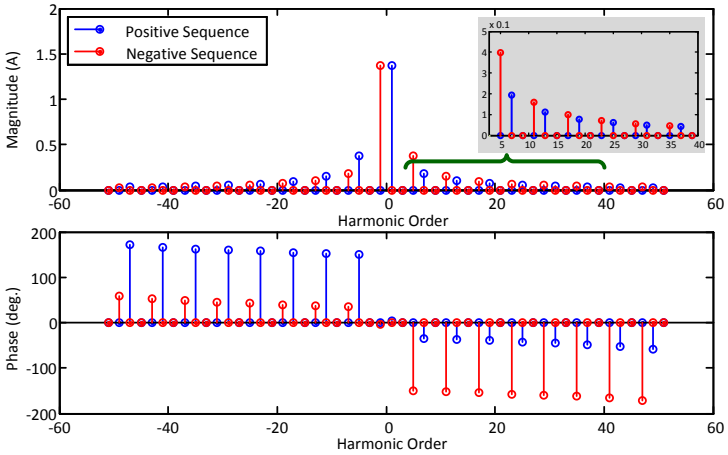

(a)

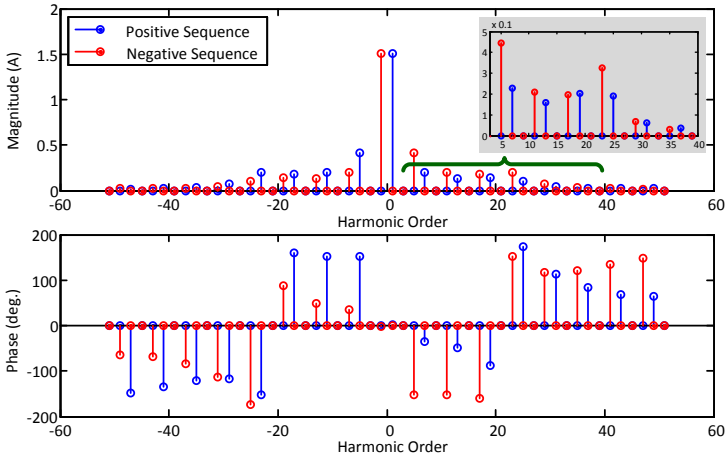

(b)

Figure 2-7 FFT results of input current of slim dc-link drive [92]. (a) Without grid impedance. (b) With grid impdeance (0.7 mH).

component changes in the time domain [101]. In this model, however, the commutation of diode rectifier is neglected, and the frequency coupling between the low frequency and high frequency cannot be seen due to the adopted moving average window function [101]. Theoretically, the slim dc-link drive is a typical linear time periodical (LTP) system [103]. It has been verified that the harmonic state space (HSS) method, which is based on the LTP theory, is a useful way to do harmonic analysis in the power electronics converter [104] , [105]. Also, a simple HSS model has been built for a locomotive converter with diode rectifier stage [106] but without the consideration of the commutation as well. Therefore, the detailed HSS model was proposed to overcome the aforementioned problems [92], [107]. In the proposed model, they fully considered the commutation effect of the diode rectifier and built the model by using a "Dirac-comb" function [105]. The validation results have shown that the HSS model can describe the harmonic variation under different switching instants caused by different loads, as well as the harmonics coupling, in a single drive unit [92] or two-drive system [107]. As shown in Figure 2-6, the grid harmonic admittance frequency characteristic can be obtained by using the proposed model in [92]. Figure 2-7 shows the fast-Fourier transformation (FFT) analysis of the input current. According to these results, the mechanism on how the grid impedance impacts the harmonic distortion can be seen, also on which critical order harmonics can be influenced.

2.2.2. Harmonic Performance Improvement

Some studies have been attempted to solve the harmonic issues in a single drive. The active damping control was naturally chosen as first trial when estimating the system stability control. It was found that it can improve the harmonic performance [75], [84]–[86], such as in the case the THD of 44% was obtained in a conventional drive but 40% was obtained in a slim dc-link drive by using the Cur_inj method [75], or in another case the THD was improved from 78% to 41.5% after using the Vol_inj method in a slim dc-link drive [84]. In fact, using the active damping control helps to reduce the harmonic sources value or to increase the harmonic impedances [108].

Another method was from the study of an improved ESI scheme proposed in [109]. Compared with same scheme in [37], the difference is that the electrolytic capacitor is replaced by a film capacitor. In [37] and [110], it was claimed that the harmonics performance can be improved but there was no real verified results. In this approach, the shortcomings as mentioned in last chapter still exist [4], [9].

Also, the method was the aforementioned dc-link shunt compensator as described in [88]. Besides keeping system operate stable, the compensator can improve the grid current harmonics in order to satisfy the standard IEC 61000-3-12. However, the drive performance may be sensitive to the grid impedance variation.

2.3. Summary

In this chapter, two main challenging issues with reference to the system instability and harmonics performance of the slim dc-link drive are reviewed. The relevant solutions are discussed in brief, and their advantages and disadvantages are given in order to outline the state-of-the-art achievements. Also, the methods to do harmonic analysis are discussed.

Chapter 3. Generalized Model of PMSM/SynRM Drive System under FOC

3.1. Introduction

It is well known that the cross-coupling term between d- and q-axis is desired to be decoupled when designing a controller. This chapter uses the transfer function matrix (TFM) method to build the model of current control loop, and extends it to the speed control loop. In this model, the PWM delay and the dc-link voltage are considered, as well as the non-identical bandwidth of current controller between d- and q- axis. In addition, it is found that the varied dq-axis inductor impacts the decoupling effect even with a decoupling block. Finally, the speed loop model is discussed as well.

3.2. System Model

The principle of the FOC controller is shown in Figure 3-1, where ω_e and ω_e^{ref} represent the electrical rotor speed and its reference command, θ_r represents the rotor position, F_ω and F_i represent the speed controller and current controller, W and λ represent the decoupling function block and the permanent magnetic flux linkage, i_{dq}^c and v_{dq}^c represent the dq-frame current and voltage in the controller, $v_{\alpha\beta}^c$ represents the $\alpha\beta$-frame voltage in the controller, S_{uvw} represents the switching logic of the converter, v_{dc} and i_{uvw} represent the dc-link voltage and motor stator current, SVM represents the space vector modulation module.

In order to reduce the complexity, the slim dc-link drive model is built with the following assumptions: (1) there is no power loss in the diode rectifier and inverter; (2) the modulation index is in the linear zone.

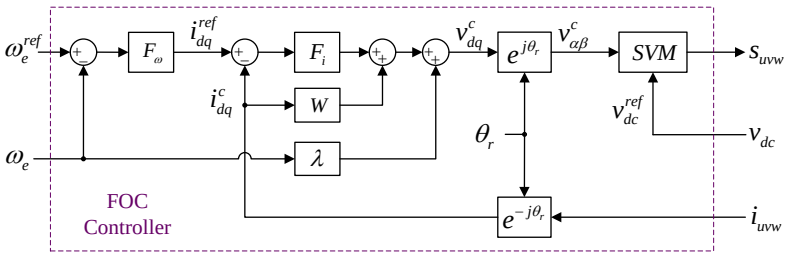

Figure 3-1 FOC Controller of the VSD

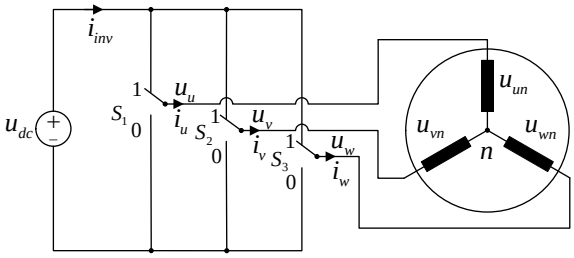

Figure 3-2 Voltage source inverter with the three-phase motor

3.2.1. Effect of DC-Link Voltage

To find the effect of the dc-link voltage, the relation between the motor stator voltage and the dc-link voltage must be founded.

3.2.1.1 Voltage Vector in Three Phase Inverter

As well known in an ideal ac drive, the three-phase sinusoidal voltages are applied to each of the motor phase winding to generate the sinusoidal currents. The motor drive circuit behaves as a voltage source inverter (VSI) which can be deemed as an ideal switch in each leg, as shown in Figure 3-2. The switching function S_i of the each switch is defined as,

$$S_i(t) = \begin{cases} 1 \\ 0 \end{cases}, i = \{1, 2, 3\} \tag{3.1}$$

The line-line voltage in respect to the dc-bus voltage can be expressed as (3.2) [111].

$$\begin{bmatrix} u_{uv}(t) \\ u_{vw}(t) \\ u_{wu}(t) \end{bmatrix} = \begin{bmatrix} S_1(t) - S_2(t) \\ S_2(t) - S_3(t) \\ S_3(t) - S_1(t) \end{bmatrix} u_{dc}(t) \tag{3.2}$$

In the application of the operation frequency is much lower than the switching frequency of the switchers, the idea switching function can be modeled by the average model [111] whose value is the duty-cycle of each switching, denoted as $d_i(t)$.

$$\begin{bmatrix} u_{uv}(t) \\ u_{vw}(t) \\ u_{wu}(t) \end{bmatrix} = \begin{bmatrix} d_1(t) - d_2(t) \\ d_2(t) - d_3(t) \\ d_3(t) - d_1(t) \end{bmatrix} u_{dc}(t) \tag{3.3}$$

Considering the relation between the phase voltage and line-line voltage of the three p hase circuit, the relation between phase voltage and dc-bus voltage can be derived.

$$\begin{bmatrix} u_{un}(t) \\ u_{vn}(t) \\ u_{wn}(t) \end{bmatrix} = \frac{1}{3}\begin{bmatrix} 2 & -1 & -1 \\ -1 & 2 & -1 \\ -1 & -1 & 2 \end{bmatrix}\begin{bmatrix} d_1(t) \\ d_2(t) \\ d_3(t) \end{bmatrix} u_{dc}(t) \tag{3.4}$$

where n is neutral point of the motor stator winding. In the following, the voltage vector can be obtained naturally by using the Clark transformation.

$$v_{\alpha\beta}(t) = \underbrace{\frac{1}{3}\underbrace{\begin{bmatrix} 1 & -\frac{1}{2} & -\frac{1}{2} \\ 0 & \frac{\sqrt{3}}{2} & -\frac{\sqrt{3}}{2} \\ \frac{1}{2} & \frac{1}{2} & \frac{1}{2} \end{bmatrix}}_{C_{3/2}}\begin{bmatrix} 2 & -1 & -1 \\ -1 & 2 & -1 \\ -1 & -1 & 2 \end{bmatrix}\begin{bmatrix} d_1(t) \\ d_2(t) \\ d_3(t) \end{bmatrix}}_{d(t)} u_{dc}(t) \tag{3.5}$$

where $C_{3/2}$ represents the Clark transfermation, $d_i(t)$ represents the duty-cycle of each leg in the inverter.

3.2.1.2 Sampling Effect in Pulse Width Modulation (PWM)

The effect of PWM is a discrete digitalization function to process the input signal, as shown in Figure 3-3. A set of latch-based model is used for mimicking the sampling effect, which includes a sampler together with a Zero-Order Holder (ZOH), especially when a micro controller, such as Digital Signal Processor (DSP), is used [112].

While, the total transfer function of sampling effect can be obtained with the sampling period T_s [112]. The sampling delay of the sampling process is reasonably approximated as half of the sampling period T_s [113].

$$\frac{v_o(s)}{v_{in}(s)} = \frac{1 - e^{-sT_s}}{sT_s} \approx e^{-s\frac{T_s}{2}} \tag{3.6}$$

Therefore, to obtain a high accuracy voltage vector, the desired duty-cycle $d(t)$ shall be high accuracy. It thus requires considering the sampling delay at least when processing the duty-cycle command $d^c(t)$ to obtain the desired duty-cycle $d(t)$.

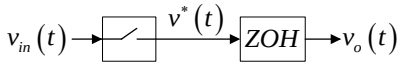

Figure 3-3 Model of the sampling effect [112].

3.2.1.3 Voltage Vector in terms of DC-Link Voltage

On the other hand, the duty-cycle command $d^c(t)$ as the input is the ratio of the current controller output $v_{\alpha\beta}^c(t)$ and sensing voltage $u_{dc}(t)$, which can be expressed,

$$d^c(t) = \frac{v_{\alpha\beta}^c(t)}{u_{dc}(t)} \tag{3.7}$$

According to previous discussion, it can be known that there exists sampling delay due to the function of ZOH during the sampling process in PWM. Specifically, regarding the dc-bus voltage $u_{dc}(t)$, it is one of the quantities to calculate the duty-cycle command. Often, a Low-Pass filter (LPF) is employed to filter out the noise pollution. From another view, this sensing with LPF can be deemed that an equivalent HPF is used to obtain the variation component of the dc-bus voltage. While either the LPF or HPF will introduce a time delay. Therefore, $d(t)$ can be approximated as (3.8) by multiplied (3.6) and (3.7), where t_d represents the time delay whose value equals to at least the sampling time delay.

$$d(t) \approx \frac{v_{\alpha\beta}^{ref}(t-t_d)}{u_{dc}(t-t_d)} \tag{3.8}$$

After linearized this equation in the form of first-order Taylor series expansion, it can be simplified as

$$d(t) = \frac{D(t)}{U_{dc0}} v_{\alpha\beta}^{ref}(t) - \frac{v_{\alpha\beta0}^{ref}}{U_{dc0}^2} D(t) A_{HPF}(t) u_{dc}(t) \tag{3.9}$$

where $D(t)$ and $A_{HPF}(t)$ represent the PWM sampling delay and HPF respectively, and the subscripts 0 means the steady-state operation point.

By substituted (3.9) into (3.5), linearize the equation at the steady-state operation point of the dc-bus voltage and desired voltage vector reference, then it can be obtained [114],

$$v_{\alpha\beta}(t) = D(t) v_{\alpha\beta}^{ref}(t) + \frac{v_{\alpha\beta0}^{ref}}{U_{dc0}} \big(1 - D(t) A_{HPF}(t)\big) u_{dc}(t) \tag{3.10}$$

When using Laplace transformation, (3.10) will be expressed as,

$$v_{\alpha\beta}(s) = D(s) v_{\alpha\beta}^{ref}(s) + \frac{v_{\alpha\beta0}^{ref}}{U_{dc0}} \left(1 - \underbrace{D(s) A_{HPF}(s)}_{\dot{D}\dot{A}}\right) u_{dc}(s) \tag{3.11}$$

For the sake of the simplification, the notation (s) is omitted so that (3.11) can be expressed as

$$v_{\alpha\beta} = Du_{\alpha\beta}^{ref} + \frac{v_{\alpha\beta0}^{ref}}{U_{dc0}}(1 - DA)u_{dc} \tag{3.12}$$

By using the Park transformation, the model in dq-frame can be obtained as well.

$$v_{dq} = Dv_{dq}^{ref} + \frac{v_{dq0}^{ref}}{U_{dc0}}(1 - DA)u_{dc} \tag{3.13}$$

3.2.2. Motor Voltage Equation

As shown in Figure 3-1, the voltage formula on the dq-frame stator can be obtained in the form of scalar notation [115] by using the reference frame transformation and inverse transformation.

$$v_{dq}(t) = e^{-j\omega_e t} \cdot v_{uvw}(t) \tag{3.14}$$

$$i_{dq}(t) = e^{-j\omega_e t} \cdot i_{uvw}(t) \tag{3.15}$$

$$\begin{cases} v_d(t) = R_s i_d(t) + \dfrac{d}{dt}\lambda_d(t) - \omega_e \lambda_q(t) \\ v_q(t) = R_s i_q(t) + \dfrac{d}{dt}\lambda_q(t) + \omega_e \lambda_d(t) \end{cases} \tag{3.16}$$

where,

$$\begin{cases} \lambda_d(t) = L_d i_d(t) + \lambda_{pm} \\ \lambda_q(t) = L_q i_q(t) \end{cases} \tag{3.17}$$

In the case of PMSM, λ_{pm} in (3.17) is a constant value, while in the case of SynRM, $\lambda_{pm} = 0$. ω_e represents the electrical rotor speed.

It is obviously to see that the coupling quantity $-\omega_e\lambda_q$, $\omega_e\lambda_d$ between d- and q- axis exists in the voltage formula. Also, it can be seen that there are two inputs and two outpus in the system of (3.16). The space vector notation [116] is used to describe this system in a convenient way.

$$v_{dq}(t) = R_s i_{\mathrm{dq}}(t) + L_{dq}\frac{d}{dt}i_{dq}(t) + \omega_e \begin{bmatrix} 0 & -L_q \\ L_d & 0 \end{bmatrix} i_{dq}(t) + \omega_e \begin{bmatrix} 0 \\ \lambda_{pm} \end{bmatrix} \tag{3.18}$$

When using the Laplace transform, the form of TFM [117], [118] can be obtained as shown in (3.19)(3.20), in which s is omitted.

$$v_{dq} = \underbrace{\left(Z_{dq} + W\right)}_{Z_m} i_{\mathrm{dq}} + \omega_e \lambda \tag{3.19}$$

$$\text{where, } Z_{dq} = R_s I + sL_{dq}, \mathrm{W} = \omega_e J L_{dq}, \lambda = \begin{bmatrix} 0 \\ \lambda_{pm} \end{bmatrix} \tag{3.20}$$

$$I = \begin{bmatrix} 1 & 0 \\ 0 & 1 \end{bmatrix}, L_{dq} = \begin{bmatrix} L_d & 0 \\ 0 & L_q \end{bmatrix}, J = \begin{bmatrix} 0 & -1 \\ 1 & 0 \end{bmatrix} \tag{3.21}$$

3.2.3. Current Controller

As shown in Figure 3-1, the voltage references, i.e. the output of current controllers, can be obtained as,

$$v_{dq}^c = F_i\left(i_{dq}^{ref} - i_{dq}^c\right) + W \cdot LF_i \cdot i_{dq}^c + \omega_e \lambda \tag{3.22}$$

where,

$$F_{id} = BW_d \left(L_d + \frac{R_s}{s}\right), F_{iq} = BW_q \left(L_q + \frac{R_s}{s}\right) \tag{3.23}$$

$$F_i = \begin{bmatrix} F_{id} & 0 \\ 0 & F_{iq} \end{bmatrix} \tag{3.24}$$

It is worth to note that the BW_d and BW_q are the bandwidth of the *d*-axis and *q*-axis current loop regulator respectively.

3.2.4. Speed Controller

The speed loop defines the reference of the current loop, as shown in Figure 3-1. The current references from the speed controller can be obtained where a traditional Proportion-Integration (PI) is used.

$$i_{dq}^{ref} = K \cdot F_\omega\left(\omega_e^{ref} - \omega_e\right) \tag{3.25}$$

where, K is a option decided by the motor type under the control of Maximum Torque-Per-Amper (MTPA).

$$K = \begin{cases} [0 \quad 1]^T, PMSM \\ [1 \quad 1]^T, SynRM \end{cases} \tag{3.26}$$

$$F_\omega = k_{pw} + \frac{k_{iw}}{s} \tag{3.27}$$

3.2.5. Electromagnetic Torque

The electromagnetic torque is the quantity to transfer electrical energy to mechanical energy, which can be expressed as ,

$$T_e = 1.5N_{pp}\lambda_{pm}i_q + 1.5N_{pp}(L_d - L_q)i_d i_q \tag{3.28}$$

where N_{pp} represents the pole-pairs. Note that the electro-magnetic torque includes two terms [119]: the first term is usually referred as the synchronous torque T_{es} which is produced by the interaction between the rotor magnet and q-axis stator current, and the second is known as the reluctance torque T_{er} which contains the motor reluctance variation. Theoretically, there is only synchronous torque in Surface- mounted PMSM (SPMSM) due to the equaled d- and q-axis inductance. There is only reluctance torque in the SynRM due to without PM in rotor. In the case of Interior PMSM (IPMSM), both types of torque exist but generally the majority is contributed by the synchronous torque.

When the bandwidth of d-axis current controller is often slower than q-axis current controller, the d-axis can be deemed as a constant value. The vector notation of the electromagnetic torque can thus be expressed as,

$$T_e = \underbrace{1.5N_{pp}\begin{bmatrix}0 & \lambda_{pm} + (L_d - L_q)I_{d0}\end{bmatrix}}_{K_T} i_{dq} \tag{3.29}$$

3.2.6. Mechanical Dynamic Equation

The mechanical dynamic equation is given by

$$T_e = T_L + (J_t s + B_v)\frac{\omega_e}{N_{pp}} \tag{3.30}$$

where $\omega_m = \frac{\omega_e}{N_{pp}}$ represents the mechanical rotor speed.

3.3. Transfer Function Matrix Model of Current Loop

3.3.1. Overview of Current Loop Model

Commonly, the current controller is designed on the dq-frame, i.e. the synchronous reference frame. It brings much convenience due to that the quantities of the voltage/current are the dc signals. The side-effect of this transformation to dq-frame is to yield the speed-dependent cross-coupling quantities between the d-axis and q-axis stator voltage, which may cause an oscillatory response to deteriorate the dynamic response of the current controller in some applications [113].

The traditional method to build the model of motor drive system is based on state equations [116], [120]. Its main con is that the system is expressed as a high-order system so that it will bring out difficulties to design current controller [121]. Two other groups methods are thus proposed to illustrate the cross-coupling component decoupling due to more convenience. The first is described as the complex space vector (CSV) [115], [121]-[125]. This group method is effective and convenient to design the current controller for the non-saliency machine or symmetric system, such as SPM, even Induction Machine (IM) [121]. While in terms of the saliency machine or asymmetric system, such as IPM or SynRM, the approach in form of TFM, or Transfer Matrix (TM), will be the good choice [117], [118], [126]. Therefore, this study adopts the principle of TFM method to meet the primary goal that a unified current control loop model is permitted to be built for both of the saliency and non-saliency machine.

While, existing decoupling methods are based on the assumption that the controllers have the same bandwidth in the d- and q-axis. Actually in the case of the low bandwidth of d-axis current controller, a fair large transient error in i_d may be introduced to exchange for a faster transient response in i_q, as point out in [127]. In addition, the inductance of L_{dq} is varied with different load current because of the characteristics of magnetic saturation and cross-coupling, as shown in Figure 3-5,

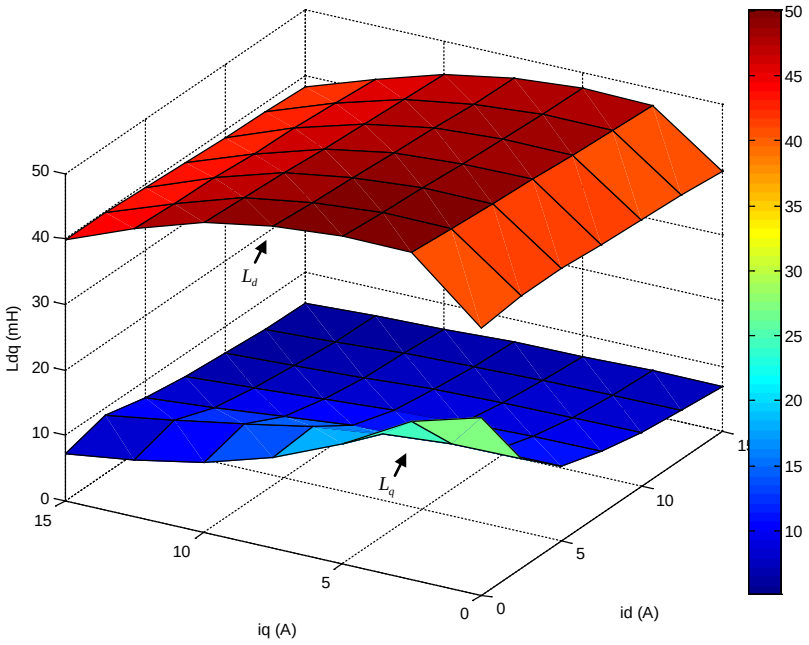

Figure 3-4 Measured inductance of L_{dq} of a target SynRM

which will reduce the decoupling effect.

The pattern of the current controller is often mentioned and performed as one-degree-of-freedom (1DOF) or two-degree-of-freedom (2DOF) [128]. Both are different names for the so-called proportional-integral (PI) controller and integral-Proportional (IP) controller in respect. In fact, the 2DOF is equivalent to the transition from a 1DOF, or PI controller, with an additional state feedback branch [117]. Therefore, the PI controller is chosen here to demonstrate the analysis. In addition, the method of the dead time compensation in [113] is also used in this study.

3.3.2. Current Loop Model without LPF

In the case of large mechanical time-constant, the impact of the mechanical dynamic can be neglected when deriving the model of current loop. The block diagram of the closed current loop without LPF is shown in Figure 3-5, where the D_c represents the delay compensation presented in [113]. The mathematic model of current loop can be derived as given in (3.31), where c is the ratio between BW_{id} and BW_{iq}.

$$G_i = G_{i_{dq}\text{-}i_{dq}^{ref}} = \frac{s\cdot BW_{iq}\begin{bmatrix} c & 0 \\ 0 & 1 \end{bmatrix} + c\cdot {BW_{iq}}^2 I}{s^2 + (1+c)BW_{iq}\cdot s + c\cdot {BW_{iq}}^2} \tag{3.31}$$

$$G_i = \begin{bmatrix} G_{idd} & G_{idq} \\ G_{iqd} & G_{iqq} \end{bmatrix} \tag{3.32}$$

Obviously, when identical bandwidths are used (i.e., $c = 1$), the transfer function (TF) in (3.31) will equal to the derived model in [125], [126], i.e., $G_i = \frac{BW_{iq}}{s+BW_{iq}} I$. It also can be seen that the current closed-loop (CL) is impacted by both two bandwidths BW_{id} and BW_{iq} simultaneously if with two non-identical bandwidths of d- and q-axis (i.e., $c \neq 1$) Considering G_i is a 2×2 TFM, each term inside is thus defined as in (3.32), where G_{idd}(or G_{iqq}) means the TF between the output and reference current in the d-axis (or q-axis); G_{idq} (or G_{iqd}) means the TF between the output current in d-axis (or q-axis) and reference current in the q-axis (or d-axis).

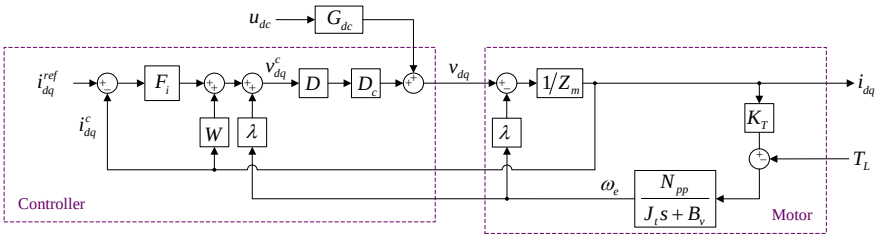

Figure 3-5 Block diagram of Current control loop without LPF

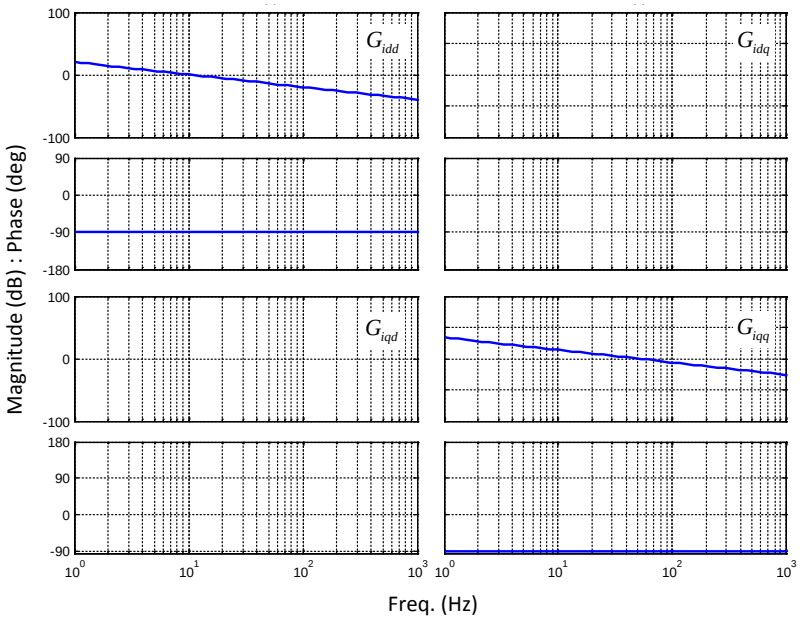

Figure 3-6 Bode diagram of G_i

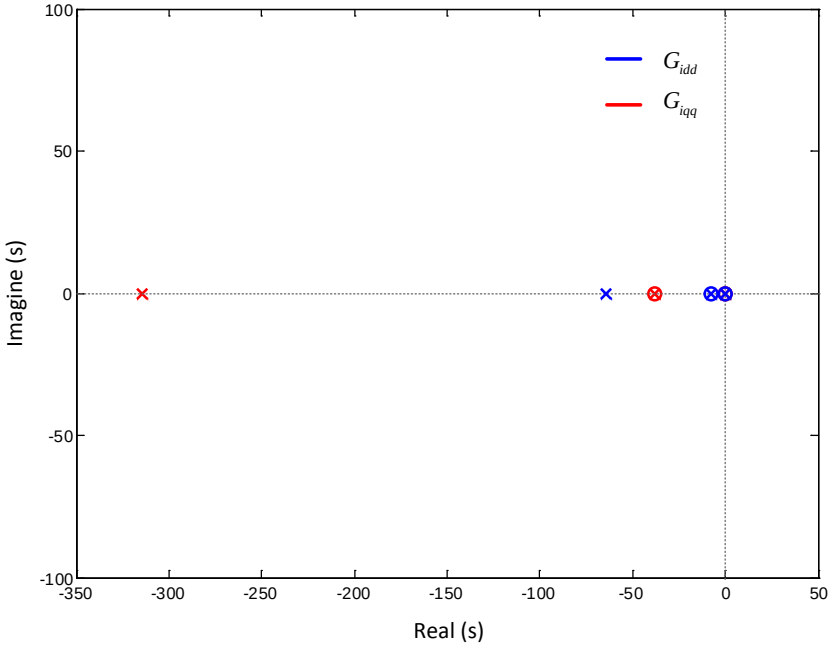

Figure 3-7 Poles and Zeros of G_{idd} and G_{iqq}

Figure 3-6 and Figure 3-7 show the Bode diagram and Zero-Pole plot in respectively for the current control loop when using two non-identical bandwidths ($BW_{id} = \frac{L_q}{L_d} BW_{iq}$). It can be observed that the transfer matrix in (3.30) becomes a 1st-order system if the estimated parameter is highly accurate, and there is no coupling between d- and q-axis because there is nothing shown in the area of back-diagonal as seen from Figure 3-6. The right-most zeros and poles in Figure 3-7 cancel each other, and the leaving left poles locate on the negative real-axis but the pole's location of d-axis is closer than of the q-axis. This means the setting-time of d-axis is quite slower than the q-axis, and there is no oscillation of the output in both axes in theoretically due to without imaginary component.

Figure 3-8 and Figure 3-9 are the Bode diagram and Zero-Pole plot in respect with a -10% inductance variation of L_d and a -30% of L_q when the rotor speed runs from 100 to 1500 rpm. By compared with Figure 3-6, one interesting result can be seen from Figure 3-8 that there come out the Bode diagrams drawn in the back-diagonal area, which means the decoupling block does not work anymore. With reference to Figure 3-9, the cancellation effect of the right-most pair of zero-pole becomes a little bit poor. The left pole moves to the right direction when the rotor speed increases. If the inductance variation is serious, some of the poles may move further close to the imaginary axis, so that the actual control bandwidth becomes lower than the desired, which is consistent with the analysis in [117], [125].

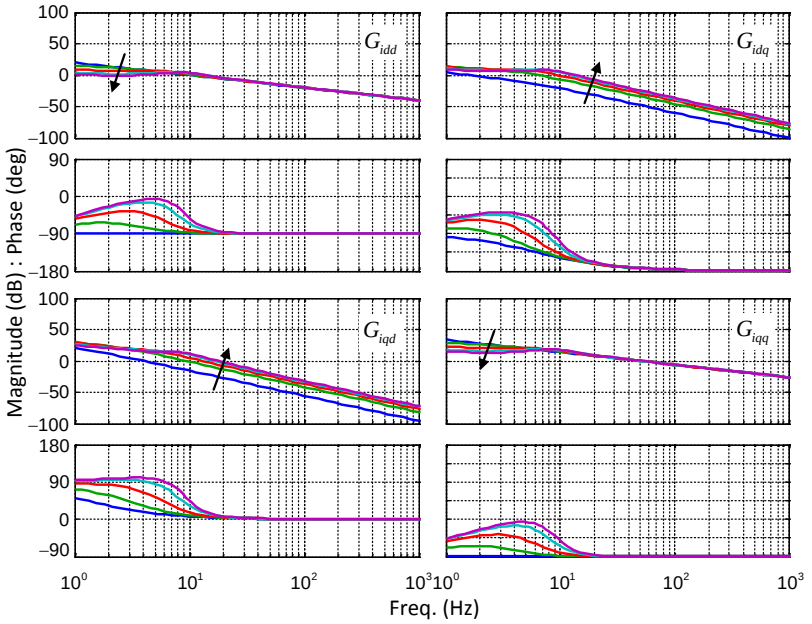

Figure 3-8 Bode diagram of G_i under the rotor speed from 100-1500 rpm

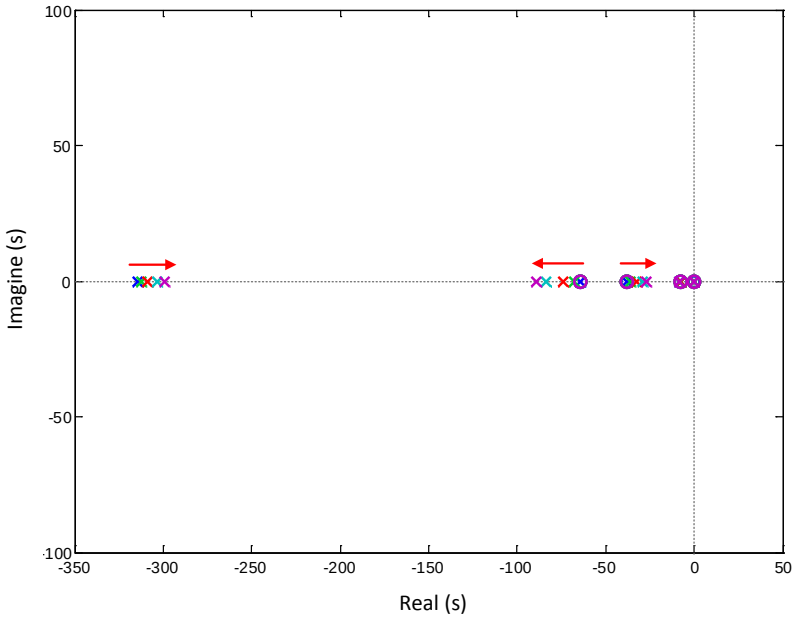

Figure 3-9 Trajectory of zeros and poles of G_{ipp} under the rotor speed from 100-1500 rpm

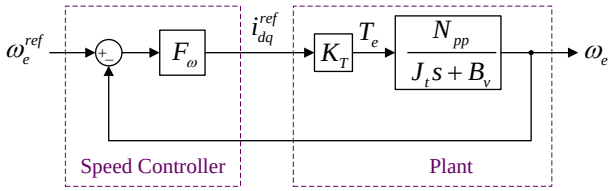

Figure 3-10 Simplified block diagram of speed loop [131]

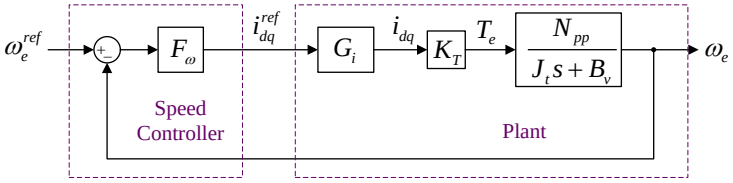

Figure 3-11 Block diagram of speed loop

3.4. Speed Loop Model

When modeling the speed loop of a motor drive, the current loop is often approximated as a unit one [131], or using a simplified 1-order system whose time

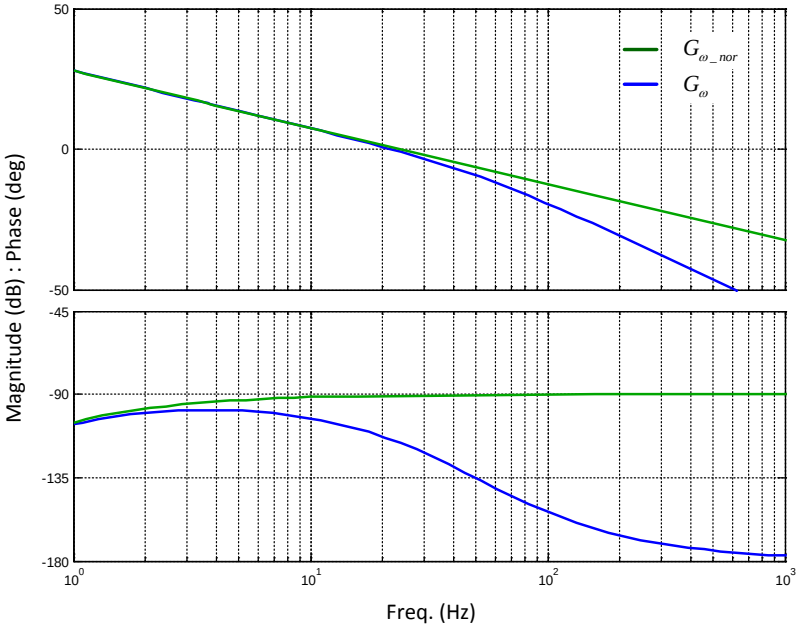

Figure 3-12 Bode diagram of speed loop under accurate L_{dq} (1500rpm)

constant is an equivalent time delay [132]. Figure 3-10 shows the simplified block diagram. The mathematical model of the closed speed loop can be obtained as,

$$G_{\omega\_nor} = \frac{F_\omega \frac{N_{pp}}{J_t s + B_v} K_T}{1 + F_\omega \frac{N_{pp}}{J_t s + B_v}} \tag{3.33}$$

One of the cons of the simplified model is hard to reflect the influence of the current loop, such as the case of the non-identical d-/q- axis current controller bandwidth. However, when building the current loop model by using TFM method, it is convenient to integrate it into the speed loop even with two non-identical bandwidths of d- and q-axis current loop as shown in Figure 3-11 which includes the inner current loop. The mathematical model of closed speed loop can be derived as (3.34).

$$G_\omega = \frac{K_T \frac{N_{pp}}{J_t s + B_v} G_i K F_\omega}{1 + K_T \frac{N_{pp}}{J_t s + B_v} G_i K F_\omega} \tag{3.34}$$

It can be seen that the simplified model in (3.33) is the same as the detailed model (3.34) on the magnitude frequency response in the low frequency zone. But at the high frequency zone, there is one more pole in the detailed model in (3.34) so that its magnitude slope tends to be -20 dB per decade more, and the phase introduces -90 degree more, i.e. goes to be -180 degree. The difference can be seen in Figure 3-12.

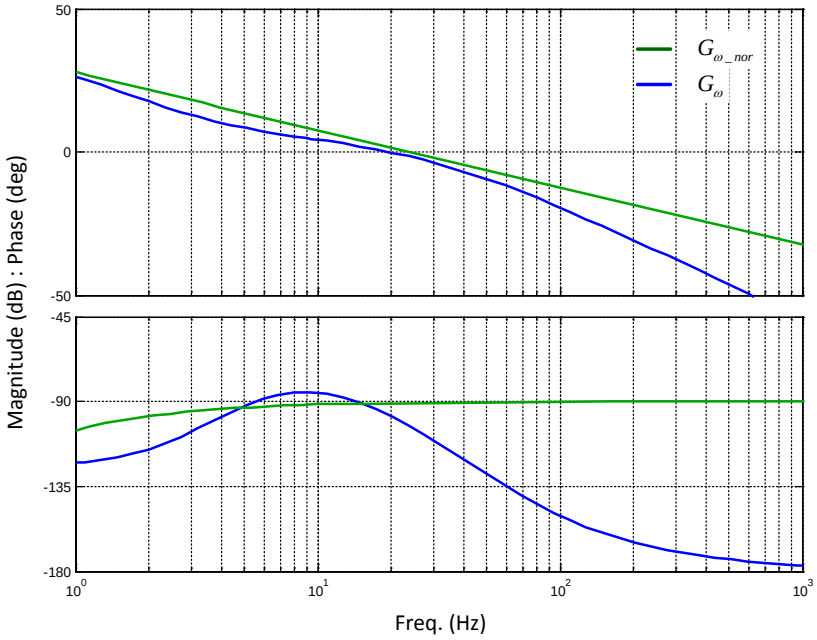

Figure 3-13 Bode diagram of speed loop under mismatched L_{dq} (1500rpm)

As discussed above, the mismatched inductance of L_{dq} leads to a degraded decoupling function, if such function is used. The current loops are thus influenced, and it will subsequently influence the speed loop performance. Based on the detailed model shown in (3.34), this phenomenon can be observed from the bode diagram as shown in Figure 3-13. By using the detailed model, the changes of both the amplitude and phase frequency characteristics can be observed between the mismatched and accuracy L_{dq}, especially at the low-end frequency zone and high-end frequency zone. However, there is no changes can be seen when using simplified model.

3.5. Summary

This chapter has been developing a unified current loop model which is feasible for the PMSM and SynRM motor drive systems by using the principle of transfer function matrix. In this model, the effect of both dc-link voltage and the current controller bandwidth are involved in as well as the impact of the mismatched dq-axis inductance. Finally, a speed loop model is discussed on a developed detailed model with the extension of using the developed unified current loop model.

Chapter 4. Investigation of Active Damping Control for Slim DC-Link Drive

4.1. Introduction

As stated in previous chapters, the slim dc-link motor drive system is a two-stage system, which can be looked at as a source-stage (i.e. rectifier stage and dc-link) followed by a load-stage (i.e. inverter with motor stage). The load-stage behaves as a CPL characteristic under the perfect current or torque control. Along with the reduced capacitance of slim dc-link capacitor, the CPL characteristic may lead to instability issues in a motor drive. One of the effective methods to stabilize such a slim dc-link drive system is to use active damping (ADMP) control methods [63], [73], [75], [82], [83], [84]-[86], [108].

To assess such drive system in terms of stability, the Routh-Hurwitz stability criterion is often adopted [73] when it is simplified to a dc system. For using use this criterion, the developed average model is simple lying where the motor load operates in a stability point (or an equilibrium point). This fact is not the case where the drive system exhibits as a nonlinear dynamic system, without consideration of the influences from the motor controller.

As an alternative, several stability criteria for the dc system have been set forth, mainly including two categories. One category is the minor-loop gain based criteria [134] that include the original Middelbrook criterion [135] and its extensions (such as the gain and phase margin (GMPM) criterion [136], the opposing argument (OA) criterion [138]), the energy source analysis consortium (ESAC) criterion [137], the general stability criterion [139] and the maximum peak criteria [140]. Another category is the coupling stability theory based criteria [141], such as passivity-based stability (PBS) criterion [142]. The first category is influenced by the power flow direction [139] while the second category is not [142]. All the criteria provide sufficient, but not necessary, conditions for the stability of a dc system [142].

One of precondition to use the above stability criteria is to build the output and input impedance of the motor drive system after it is simplified as a dc system, which is shown in Figure 4-1. With reference to the equivalent circuit, the output impedance is easily calculated by only targeting a simplified equivalent passive LC tank. Thus most efforts are needed for the input impedance deduction for its more complexities. The input admittance has been deduced by using state-space equations [143], while this method may lead to high-order mathematical models which are complex for theoretical analysis. Moreover, the input admittance has been derived in [73], [144], [145] in the frequency domain where the influence from the speed-loop is not considered.

Besides the stability issue, the input harmonic performance is another issue in the slim dc-link motor drive especially when feeding from a large grid impedance [108]. Using active damping control methods will shape the total impedance of the motor drive so that it is possible to improve the input harmonic performance. However, the side-effect by using active damping control is the harmonic performance of the motor current (or torque) and it may become worsen.

To demonstrate the detailed analysis, this chapter will build the mathematical models using the state-of-the-art active damping methods. The main contents are presented as follows:

1) The small-signal models for the input/output impedance are developed to investigate the effect of the active damping control on the system stability performance.
2) The small-signal models for the total input impedance are developed to analyze the effect of the active damping control on the input harmonic performance.
3) The sensitivity analyses are done to check the influences on the motor stator voltage, motor torque (current) and rotor speed by using active damping control.
4) The theoretical analyses are verified from the experiments and simulations on a SynRM drive system test set-up.

4.2. Small-signal Model of Motor Drive

Figure 4-1 shows the small-signal model of the simplified equivalent circuit of the slim dc-link drive system, in which the input impedance and output impedance are defined. In this section, the small-signal mathematic models of the input and output impedance will be developed, which is based on the following assumptions: (1) there is no loss in the diode rectifier and inverter; (2) the modulation index is in the linear zone.

As normal, the process to build the input impedance mathematical model is: firstly to build a small-signal model of each component by injecting a low frequency small-signal disturbance into each component model, then to collect all these small-signal models based on the power balance rule, and finally the small-signal model of the input impedance can be achieved from the relationship between the dc-link voltage

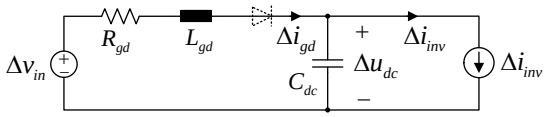

Figure 4-1 Simplified equivalent circuit, where R_{gd} and L_{gd} are the equivalent grid resistors and grid inductors respectively.

(Δu_{dc}) and the current (Δi_{inv}).

4.2.1. Three Critical Small-signal Expressions

One of important small-signal models is at the PWM component, which is the unique connection of the motor stator voltage to the voltage reference and dc-link voltage. According the model in section 3.2.1, its small-signal model can be obtained as

$$\Delta v_{dq} = D\Delta v_{dq}^{ref} + \underbrace{\frac{v_{dq0}^{c}}{U_{dc0}}(1 - DA)}_{G_{dc}} \Delta u_{dc} \tag{4.1}$$

Another critical small-signal model is the motor model, which is the control target during the current controller design. Compared with the existing model, its small-signal model can be expressed as (4.2) without neglecting the speed loop disturbance.

$$\Delta v_{dq} = Z_M \Delta i_{dq} + \underbrace{\begin{bmatrix} -L_q I_q \\ \lambda_{pm} + L_d I_d \end{bmatrix}}_{\lambda_0} \Delta \omega_e \tag{4.2}$$

The third critical small-signal model is the power balance rule of the dc-link where the expression is as given below.

$$u_{dc} i_{dc} = 1.5\left(v_d i_d + v_q i_q\right) \tag{4.3}$$

Its small-signal model is expressed in the form of (4.4).

$$\Delta u_{dc} I_{dc} + \Delta i_{dc} U_{dc} = 1.5 \begin{bmatrix} I_d \\ I_q \end{bmatrix}^T \Delta v_{dq} + 1.5 \begin{bmatrix} V_d \\ V_q \end{bmatrix}^T \Delta i_{dq} \tag{4.4}$$

4.2.2. Speed Loop, Current Loop, and Input Impedance

The small-signal models of other components, such as the current controller or speed controller, can be deduced as well by using the linearization principle, which are not listed here for the sake of simplification. Collect these models with (4.1)(4.1 and (4.2), then the expression of the small-signal models of the speed $\Delta\omega_e$ can be obtained as (4.5).

$$\Delta\omega_e = G_{\Delta\omega_e\_\Delta\omega_e^{ref}} \cdot \Delta\omega_e^{ref} + G_{\Delta\omega_e\_\Delta T_L} \cdot \Delta T_L + G_{\Delta\omega_e\_\Delta U_{dc}} \cdot \Delta U_{dc} \tag{4.5}$$

where

$$G_{\Delta\omega_e\_\Delta\omega_e^{ref}} = \frac{DF_iKF_\omega K_t G_p}{\underbrace{Z_M+(DF_iKF_\omega+(1-D)\lambda_0)K_tG_p+D(F_i-W)}_{Den\_\Delta\omega_e}} \tag{4.6}$$

$$G_{\Delta\omega_e\_\Delta T_L} = \frac{-(Z_M+D(F_i-W))G_p}{Den\_\Delta\omega_e} \tag{4.7}$$

$$G_{\Delta\omega_e\_\Delta u_{dc}} = \frac{G_{dc}K_tG_p}{Den\_\Delta\omega_e} \tag{4.8}$$

$$K_t = 1.5N_{pp}\left[\left(L_d - L_q\right)I_q \quad \lambda_{pm} + \left(L_d - L_q\right)I_d\right] \tag{4.9}$$

$$G_p = \frac{N_{pp}}{Js+B_v} \tag{4.10}$$

The expression of the small-signal models of Δi_{dq} can be obtained as (4.11).

$$\Delta i_{dq} = G_{\Delta idq\_\omega_e^{ref}} \cdot \Delta\omega_e^{ref} + G_{\Delta idq\_TL} \cdot \Delta T_L + G_{\Delta idq\_Udc} \cdot \Delta U_{dc} \tag{4.11}$$

where

$$G_{\Delta i_{dq}\_\Delta\omega_e^{ref}} = \frac{DF_iKF_\omega}{Den\_\Delta\omega_e} \tag{4.12}$$

$$G_{\Delta i_{dq}\_\Delta T_L} = \frac{(DF_iKF_\omega+(1-D)\lambda_0)G_p}{Den\_\Delta\omega_e} \tag{4.13}$$

$$G_{\Delta i_{dq}\_\Delta u_{dc}} = \frac{G_{dc}}{Den\_\Delta\omega_e} \tag{4.14}$$

By collecting these models into (4.4), a unified input impedance model can thus be obtained as (4.15) by letting the torque disturbance $\Delta T_L = 0$.

$$Y_{in} = \underbrace{-\frac{P_L}{U_{dc}^2}}_{Y_{CPL}} + \underbrace{\frac{1.5}{U_{dc}}\underbrace{\left(\begin{bmatrix}I_d\\I_q\end{bmatrix}^T\left(Z_M+\lambda_0K_tG_p\right)+\begin{bmatrix}V_d\\V_q\end{bmatrix}^T\right)}_{C_{Yctrl}}G_{\Delta idq\_\Delta Udc}}_{Y_{ctrl}} \tag{4.15}$$

The interpretation of (4.5), (4.11) and (4.15) is that the output quantities, i.e., $\Delta\omega_e$, Δi_{dq} and Y_{in} are the sum of three input quantities $\Delta\omega_e^{ref}$, ΔT_L and ΔU_{dc} with their corresponding gain, i.e. the relevant transfer function. More interestingly, the

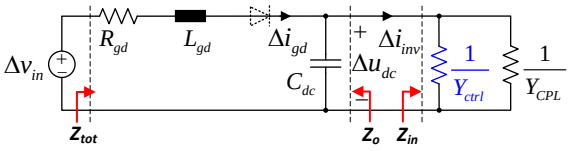

Figure 4-2 Equivalent input impedance, output impedance and total impedance

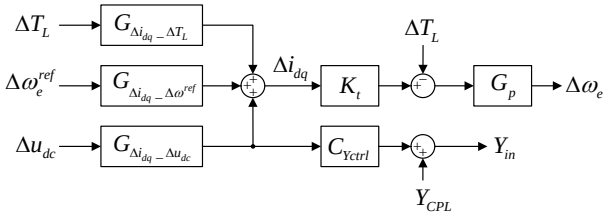

Figure 4-3 Small-signal model of motor drive system without active damping control

interpretation of (4.15) is that the input impedance involves the effect of the control loop besides the incremental negative impedance, as shown in Figure 4-2,. Further, one also can see that the difference with the model developed in [108] is the involved speed loop quantities. Figure 4-3 shows the block diagram of the small-signal model of the drive system without any active damping control method.

4.2.3. Output Impedance

As shown in Figure 4-1, the output impedance Z_o can be derived straightforward from the equivalent circuit, whose expression is presented in (4.16).

$$Z_o = \frac{sL_{gd} + R_{gd}}{s^2 L_{gd} C_{dc} + sR_{gd} C_{dc} + 1} \tag{4.16}$$

4.3. Small-signal Model of Drive System with Active Damping Control

4.3.1. Three Types of Active Damping Methods

As mentioned in Chapter 2, three-types of active damping methods are mainly studied, i.e., the Cur_inj, the Vol_inj and the VPI, whose details in the motor controller are shown in Figure 4-4. The HPF is used to filter out the dc component, and g_{iq}, g_{vq}, g_{vq} represent the gain in terms of dc-bus voltage v_{dc}. It is worth noting that the gain g_{iq} of Cur_inj is a linear quantity not a nonlinear [73], [74] so that this control strategy can be easily implemented. Regarding the first two type of active damping control (Cur_inj and Vol_inj), both d-axis and q-axis can be injected into with the dc-link voltage. For simplification, only the injection in the q-axis is discussed in this section to demonstrate the analysis, as shown in Figure 4-4 (a) and (b).

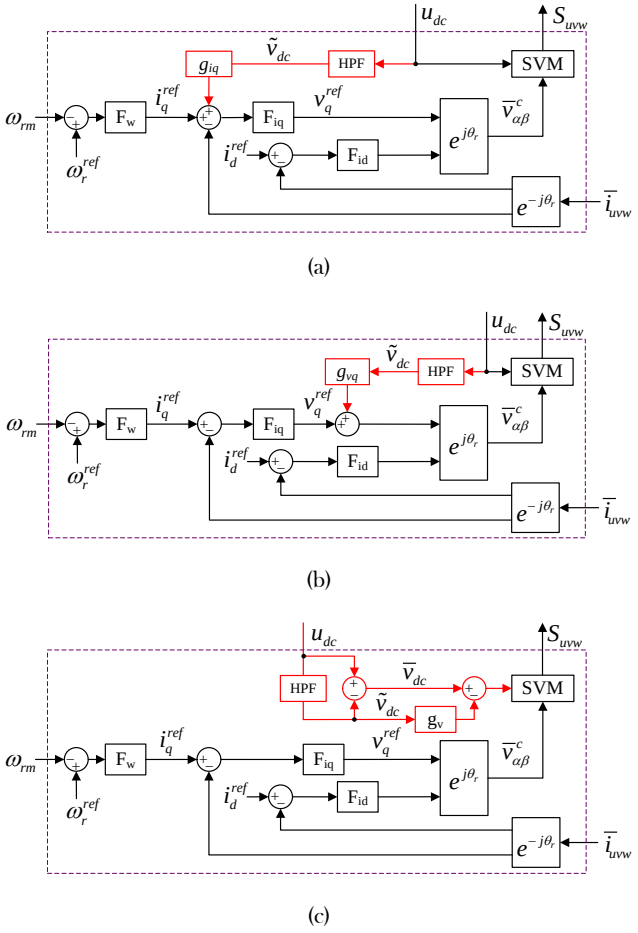

Figure 4-4 Three types of active damping control methods. (a) Current-referenc injection (Cur_inj), (b) Voltage-reference injection (Vol_inj), (c) PWM-reference injection or virtual positive impedance (VPI)

4.3.2. Modified Model using Active Damping Control

The introduced dc-bus voltage in each active damping method modifies the loop gain of the current control loop, which will shape the input impedance ultimately. Figure 4-5 shows the block diagram of the small-signal model when using active damping control. The transfer function in terms of the input Δu_{dc} is changed, which is reasonable because the introduced quantity is only from the dc-link voltage. The modified transfer function is marked as $G^{inj}_{\Delta i_{dq}\_\Delta U_{dc}}$ which can be expressed as (4.17).

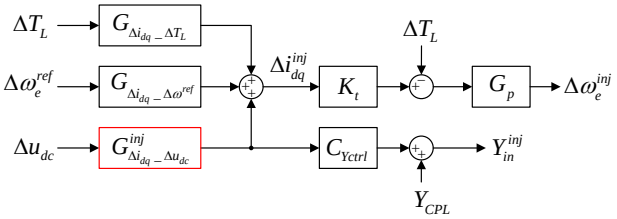

Figure 4-5 Small-signal model of motor drive system with active damping control

$$G^{inj}_{\Delta i_{dq}\_\Delta u_{dc}} = \begin{cases} \dfrac{G_{dc} + DF_i g_{iq}}{Den\_\Delta\omega_e}, & (if\ Cur\_inj) \\ \dfrac{G_{dc} + Dg_{vq}}{Den\_\Delta\omega_e}, & (if\ Vol\_inj) \\ \dfrac{G_{dc\_VPI}}{Den\_\Delta\omega_e}, & (if\ VPI) \end{cases} \tag{4.17}$$

$$G_{dc\_VPI} = \frac{v^c_{dq0}}{U_{dc0}}(1 + DA) \tag{4.18}$$

Simultaneously, the small-signal model of dq-axis current and motor speed in the case of using active damping control can be derived as:

$$\Delta i_{dq}^{inj} = G_{\Delta idq\_\omega_e^{ref}} \cdot \Delta\omega_e^{ref} + G_{\Delta idq\_T_L} \cdot \Delta T_L + G^{inj}_{\Delta i_{dq}\_\Delta u_{dc}} \cdot \Delta U_{dc} \tag{4.19}$$

$$\Delta\omega_e^{inj} = G_{\Delta\omega_e\_\Delta\omega_e^{ref}} \cdot \Delta\omega_e^{ref} + G_{\Delta\omega_e\_\Delta T_L} \cdot \Delta T_L + \underbrace{G^{inj}_{\Delta i_{dq}\_\Delta u_{dc}} K_t G_p}_{G^{inj}_{\Delta\omega_e\_\Delta U_{dc}}} \cdot \Delta U_{dc} \tag{4.20}$$

Meanwhile, the input impedance is modified as well as a unified expression is given in (4.21).

$$Y_{in}^{inj} = Y_{CPL} + \underbrace{C_{Yctrl} G^{inj}_{\Delta i_{dq}\_\Delta u_{dc}}}_{Y^{inj}_{ctrl}} \tag{4.21}$$

4.4. Analysis of Improved Stability and Input harmonics

4.4.1. Stability Analysis

According to the minor-loop gain criterion, such motor drive system can be estimated by a set of criterion as mentioned in Section 4.1. System stability can be guaranteed if the minor-loop gain does not intersect with the forbidden area defined by the criteria. Considering the fact that the ESAC criterion [137] gives the smallest forbidden area, or plays as the least conservative criterion, the ESAC criterion is chosen as the one

used in this study. Also, the PBS criterion [142] is selected as a double-check criterion seen from the passivity point of view.

Figure 4-6 shows the Nyquist diagram of the minor-loop gain in the cases with and without active damping control, whose system parameters can be seen from section 4.6. In the slim dc-link motor drive, the system behaves unstable in the case without any active damping control method, which can be seen there is intersection between the curve and the ESAC defined forbidden area (whose phase margin is 45 degree). After activating any of the active damping control methods, it is clearly seen that the intersection disappears, which means that the system goes back into a stable state condition.

Figure 4-7 shows the Nyquist diagram based on the PBS criterion for the stability double-check. Only the case of a slim dc-link drive system without any active damping control method, the trajectory enters into the left-half plane (LHP) which means the system is unstable. By contrast, the trajectories totally lie in the RHP in the case of using active damping control, which means a stable motor drive system is obtained. Therefore, the slim dc-link drive system can be operated in a stable state when using any active damping method.

The current loop bandwidth may impact on the stability performance when using active damping control. In terms of the Cur_inj method, it is generally thought that this method may not be employed due to a lower current loop bandwidth compared with the resonant frequency of LC filter [84], [133]. However, both the theoretical investigation and experimental results show that this though is not totally true. Figure 4-8 are the analysis results for each active damping method demonstrated from three different current loop bandwidth examples (i.e., Case 1: $BW_{idq} = 1\,kHz/1\,kHz$; Case 2: $BW_{idq} = 200Hz/1\,kHz$; Case 3: $BW_{idq} = 60Hz/300Hz$.). It is easily seen that the trajectory of the Cur_inj method goes very close to the forbidden area in the case of a low BW (as shown in Figure 4-8 (a)), but it is still stable. That said the Cur_inj method is still a competitive active damping method to stabilize the system. As well, the verified experimental results can be seen in the following section. In comparison, the Vol_inj method can also stabilize the drive system even at different current controller bandwidths (as shown in Figure 4-8 (b)), and there are not so much changes by using the VPI method (as shown in Figure 4-8 (c)). These results also illustrate that the last two active damping methods are insensitive to the current controller bandwidth variation to stabilize the drive system.

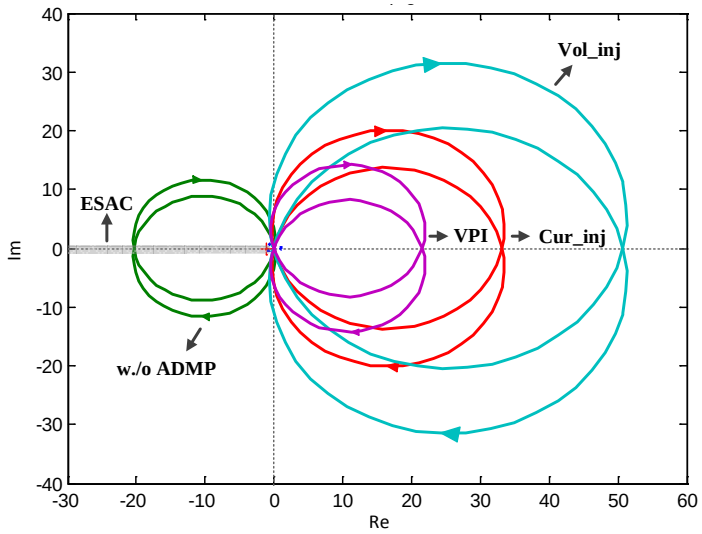

Figure 4-6 Nyquist diagram of the minor-loop gain in the case w./o and w./ active damping control. The gray area is the ESAC defined forbindden area. The blue circle is the unity-circle

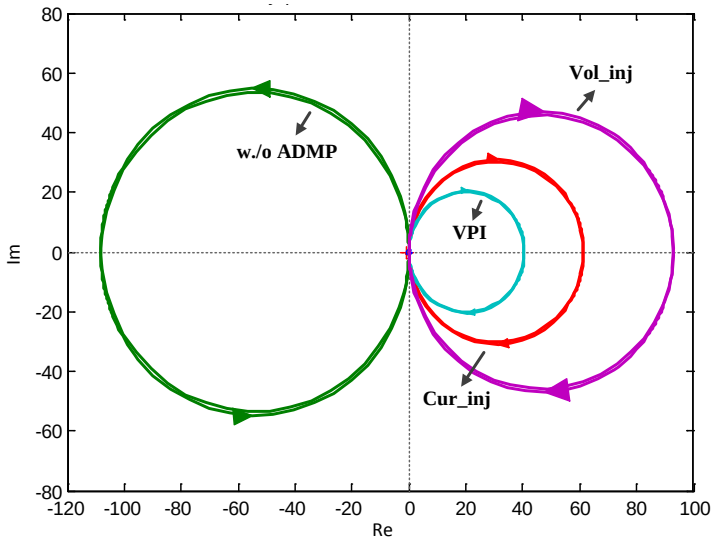

Figure 4-7 Nyquist diagram for stability analysis by using the PBS criterion.

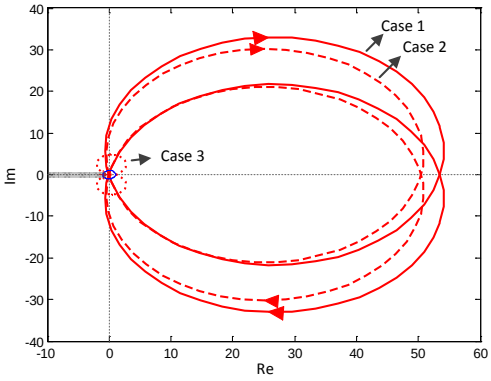

(a)

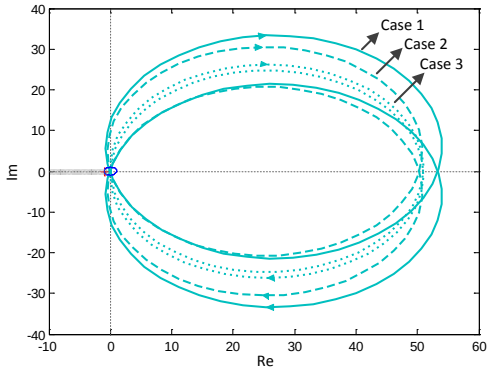

(b)

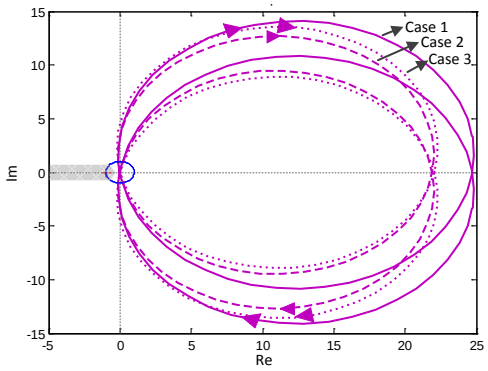

(c)

Figure 4-8 Impaction of different current loop bandwidth on the minor-loop gain where Case 1: $BW_{idq} = 1\ kHz/1\ kHz$; Case 2: $BW_{idq} = 200Hz/1\ kHz$; Case 3: $BW_{idq} = 60Hz/300Hz$. (a) Cur_inj. (b) Vol_inj. (c) VPI.

4.4.2. Input Harmonics

Using active damping control methods can improve the input harmonics performance in three-phase slim dc-link drive [73], [84]-[86], which can be explained from the impedance of view [145].

Originally, the goal by using active damping control methods is to reshape the input impedance Z_{in} so that it increases the damping factor to stabilize the whole system. A physical interpretation is that a virtual resistor is built in the load side, which will damp the resonant energy due to the resonant tank composed by L_{gd} and C_{dc}, as shown in Figure 4-1. One benefit is to flexibly achieve a stable system without the cost of extra hardware. Another is the total impedance Z_{tot}, as defined in Figure 4-2, is reshaped as well.

The input impedance Z_{in} and total impedance Z_{tot}, are shown in Figure 4-9 and Figure 4-10 with and without active damping methods. It can be seen that after using active damping control methods, the characteristic of either the input impedance or the total impedance is ultimately reshaped to behave as passive impedance with an equivalent positive resistance during the frequency range closed to resonant frequency. Specifically, the equivalent positive impedance starts from 100 Hz and gradually transforms into a pure resistor.

Expanding on this, it can also be said that the harmonic voltage sources caused by such a resonance, which is the main reason of the input harmonic issue [146], are suppressed seen from a harmonic analysis point of view. This can also be seen from the following experimental results. The reduced dc-bus harmonic voltage source will accordingly reduce the harmonic current with the increased total impedance thanks to the active damping control.

This can be explained intuitively by (4.22), deduced from [106], [146] (cf. the equations (15) and (12) respectively), which is similar as the lumped parameter principle in the electrical circuit analysis.

$$i_h = \frac{\bar{V}_s}{\bar{H}_{h,s}^{-1}} = \frac{v_h}{Z_h}\cos\Delta\theta_h \tag{4.22}$$

where $\bar{V}_s$ is the harmonics voltage source $[\ldots\ v_{-1}\ v_0\ v_{+1}\ \ldots]^{\mathrm{T}}$, $\bar{H}_{h,s}$ is the h-row quantities of the harmonic coupling matrix, v_h is defined as the synthetic h-order harmonic voltage source, Z_h is defined as the synthetic h-order harmonic impedance and $\Delta\theta_h$ is defined as the phase angle between v_h and Z_h.

After using active damping control, the resonance is suppressed so that the harmonic voltage source v_h is decreased in the middle frequency range (i.e. [100, 1000] Hz), which also can be seen from the following experimental results. Therefore, although

Z_h is reduced in the range of 50-600 Hz as shown in Figure 4-10, the harmonic current i_h, close to the resonant frequency (i.e., around 700 Hz), is still decreased because the ratio between the greatly decreased v_h (mainly caused by LC resonance) and slightly increased Z_h is reduced.

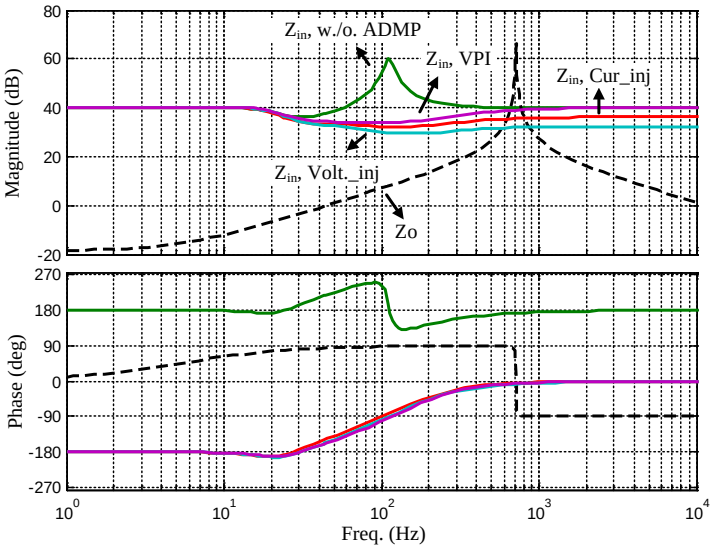

Figure 4-9 Input impedance Z_{in} in the cases w./ and w./o active damping

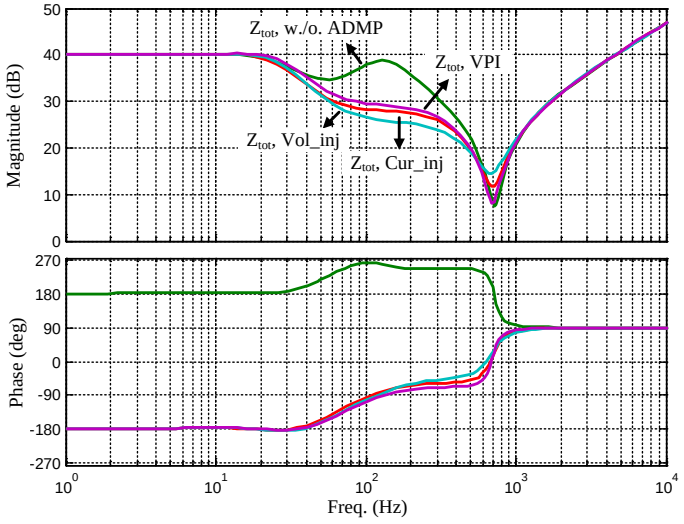

Figure 4-10 Total impedance Z_{tot} in the cases of w./ and w./o active damping

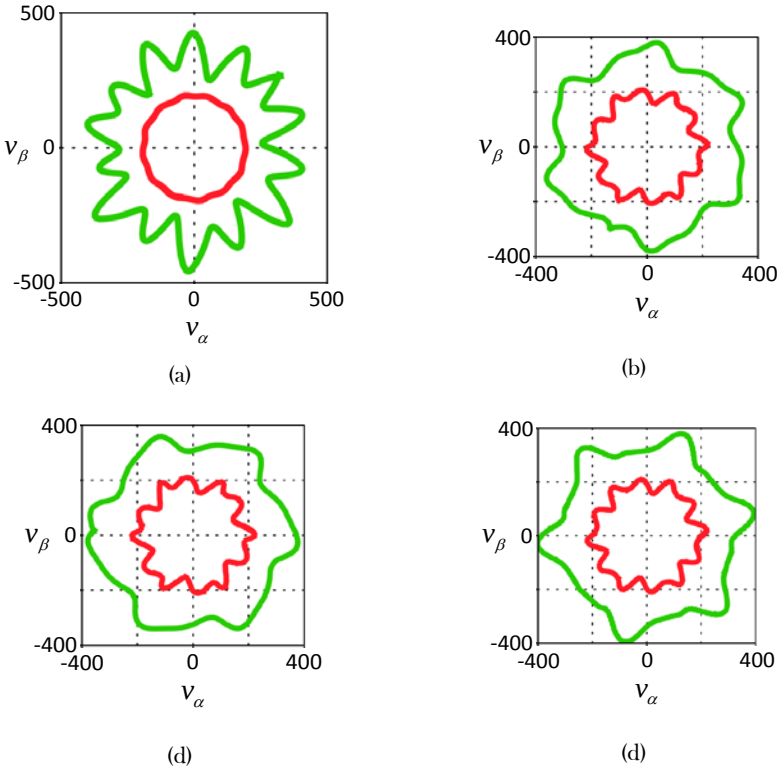

Figure 4-11 Stator voltage influenced by active damping methods. Green: dc-bus voltage. Red: stator voltage command. (a) Original. (b) Cur_inj. (c) Vol_inj. (d) VPI.

4.5. Sensitivity Analysis

4.5.1. Stator Voltage Sensitivity Analysis

Once using the active damping method, the dc-link voltage is effectively suppressed. The harmonics on the dc-bus contents mainly $6k$ times of fundamental frequency quantities. This induced harmonics will be added into the voltage command on dq-axis v_{dq}^c when any of the active damping control method is adopted. The v_{dq}^c may be expressed as shown in (4.23).

$$v_{dq}^c = V_{dq0}^c + \sum_{k=1}^{n} V_{dq6k}\, exp\left(6k\omega_g t + \theta_{6k}\right) \tag{4.23}$$

where $k = 1, 2, 3, \ldots$. The motor stator voltage will be obtained to be the same as the voltage command due to the good closed-loop control, whose expression is as given in (4.24). Therefore, the stator voltage on $\alpha\beta$-frame can be derived by using the inverse Park transformation, as shown in (4.26).

$$v_{dq} = V_{dq} + \sum_{k=1}^{n} V_{dq6k}\, exp\left(6k\omega_g t + \theta_{6k}\right) \tag{4.24}$$

$$\begin{cases} v_\alpha = V_{\alpha 0} \pm \dfrac{1}{2}\displaystyle\sum_{k=1}^{n} V_{d6k} \cos\left(\left(6k\omega_g \pm \omega_e\right)t + \theta_{6k}\right) \pm \dfrac{1}{2}\sum_{k=1}^{n} V_{q6k} \sin\left(\left(6k\omega_g \pm \omega_e\right)t + \theta_{6k}\right) \\ v_\beta = V_{\beta 0} + \dfrac{1}{2}\displaystyle\sum_{k=1}^{n} V_{d6k} \sin\left(\left(6k\omega_g \pm \omega_e\right)t + \theta_{6k}\right) - \dfrac{1}{2}\sum_{k=1}^{n} V_{q6k} \cos\left(\left(6k\omega_g \pm \omega_e\right)t + \theta_{6k}\right) \end{cases} \tag{4.25}$$

Expanding (4.26), the expression may be rearranged as shown in (4.25). It can be seen from (4.25) that the $\left(6k\omega_g \pm \omega_e\right)th$ harmonics appear in the stator voltage which comes from the induced harmonics from the dc-bus voltage. Figure 4-11 shows the simulation results under different active damping control methods. The stator voltage command is still a cycle but with certain alternating components due to the induced harmonics.

$$v_{\alpha\beta} = V_{\alpha\beta} + \left(\sum_{k=1}^{n} V_{dq6k}\, exp\left(6k\omega_g t + \theta_{6k}\right)\right) exp(\omega_e t) \tag{4.26}$$

4.5.2. Torque/Speed Sensitivity

Besides the stator voltage, the electrical torque and rotor speed are influenced as well by using active damping control. This is because that the "polluted" stator voltage will be subsequently transmitted to the motor current, and then electrical torque and speed when using the active damping control. To elaborate on this, the corresponding transfer functions are developed on the torque and speed sensitivity, which can be described as (4.27) and (4.28) respectively.

$$S_{T_e} = \begin{cases} K_t G_{\Delta i_{dq}\_\Delta u_{dc}} & (if\ w./o\ ADMP) \\ K_t G^{inj}_{\Delta i_{dq}\_\Delta u_{dc}} & (if\ w./\ ADMP) \end{cases} \tag{4.27}$$

$$S_{\omega_e} = \begin{cases} K_t G_p G_{\Delta i_{dq}\_\Delta u_{dc}} & (if\ w./o\ ADMP) \\ K_t G_p G^{inj}_{\Delta i_{dq}\_\Delta u_{dc}} & (if\ w./\ ADMP) \end{cases} \tag{4.28}$$

According to the analysis in [108], the active damping control will introduce an extra component into the transfer function of the electrical torque sensitivity. Such extra component is the product of the band-pass filter (BPF) function and another gain-dependent quantity, whose forms just changes a little bit in terms of different active damping methods.

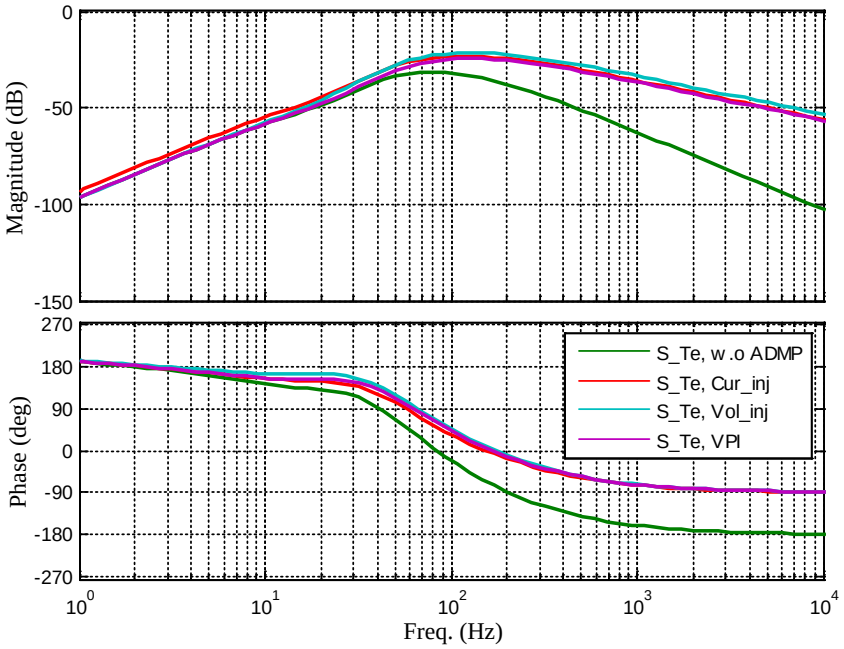

Figure 4-12 Electrical torque sensitivity analysis under different active damping methods

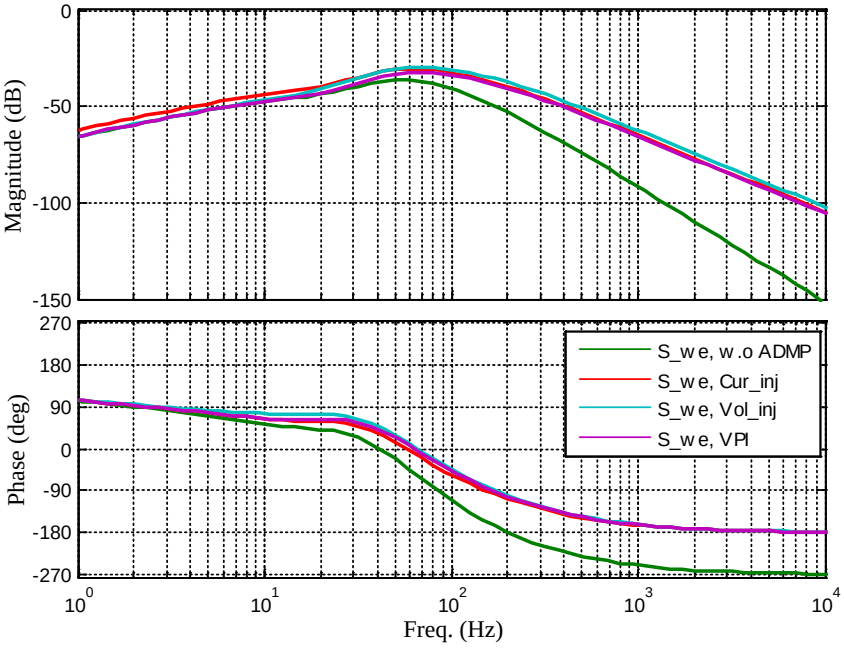

Figure 4-13 Electrical speed sensitivity analysis under different active damping methods

Figure 4-12 shows the frequency response of the torque sensitivity in the cases with and without active damping control. In the low frequency region, where the equivalent positive resistor behaviour does not appear, the torque sensitivity is same for both cases with and without active damping control. In the middle to high frequency region, the torque sensitivity is increased when using active damping control. Even with the increased sensitivity, the maximum sensitivity is still below -20 dB. Note that the results are based on the target to achieve a similar damping effect on dc-link voltage, and therefore a similar sensitivity is observed for each active damping method. Besides, when considering the voltage variation as shown in Figure 4-11, as least the 300 Hz quantity may appear on the dc-bus voltage, so that it can be imagined that the Bode diagram in Figure 4-12 will be superposed a certain spike at 300 Hz. The interpretation is that the electrical torque may have the unneglectable 300 Hz harmonic component.

The similar phenomenon happens on the speed sensitivity, which can be seen from the plotted Bode diagrams in Figure 4-13. The difference, compared with the torque sensitivity, is the effect of G_p (cf. (4.27) and (4.28)) which leads to a -40 dB/Dec above the middle frequency range. It means the speed sensitivity is better due to the high frequency noise suppression given by the slow dynamic.

4.6. Experimental Results

To verify the effectiveness of the theoretical analysis, a SynRM drive system is considered, and the schematic is shown in Figure 4-14. The system parameters are:

- Motor: rated speed = 1500 rpm, rated current = 13.9 A, poles = 4, original dq-axis inductor = 0.049 mH/0.01 mH (c.f Figure 3-4), stator resistor = 0.38 Ω , inertia = 0.019 kg·m^2.
- Drive: input voltage = 380 Vac, dc-link capacitor = 14.0 μ F, grid inductor = 1.47 mH (marked as Choke 1)/0.46 mH (marked as Choke 2).
- High BW: current controller bandwidth = 200 Hz /1500 Hz, gain of Cur_inj = 0.05, gain of Vol_inj = 1.00, gain of VPI = 1.00.
- Low BW: current controller bandwidth = 60 Hz /200 Hz, gain of Cur_inj = 0.2, gain of Vol_inj = 1.00, gain of VPI = 1.00.
- Test 1: Choke 1 + High BW.
- Test 2: Choke 1 + Low BW.
- Test 3: Choke 2 + High BW.

The test setup is shown in Figure 4-15. The slim dc-link is achieved by replacing the conventional dc-link by a 14.0 μF film capacitor. Considered that the standard has different harmonic requirement for R_{sce} above or below 120, two chokes (i.e., Choke 1 &2) are thus used to represent the grid inductor. The corresponding R_{sce} to these two chokes equals to around 100 and 320 in respectively. Accordingly, the standard requirement of the THD/PWHD is 40%/40% and 48%/46% separately. The motor

current and rotor position are measured by a sensor box that includes three closed-loop Hall-effect current transducers and an incremental position encoder.

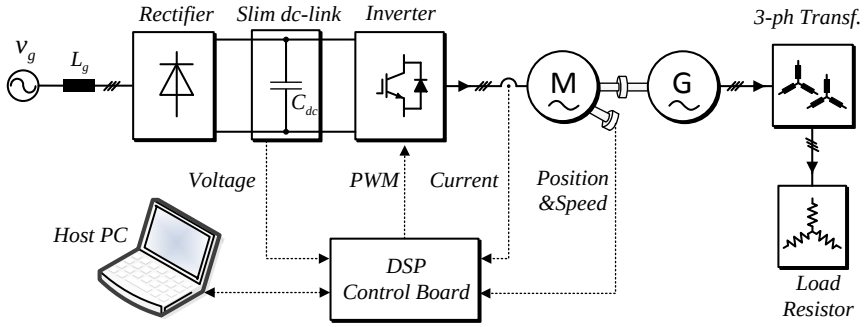

Figure 4-14 Schematic diagram of test setup

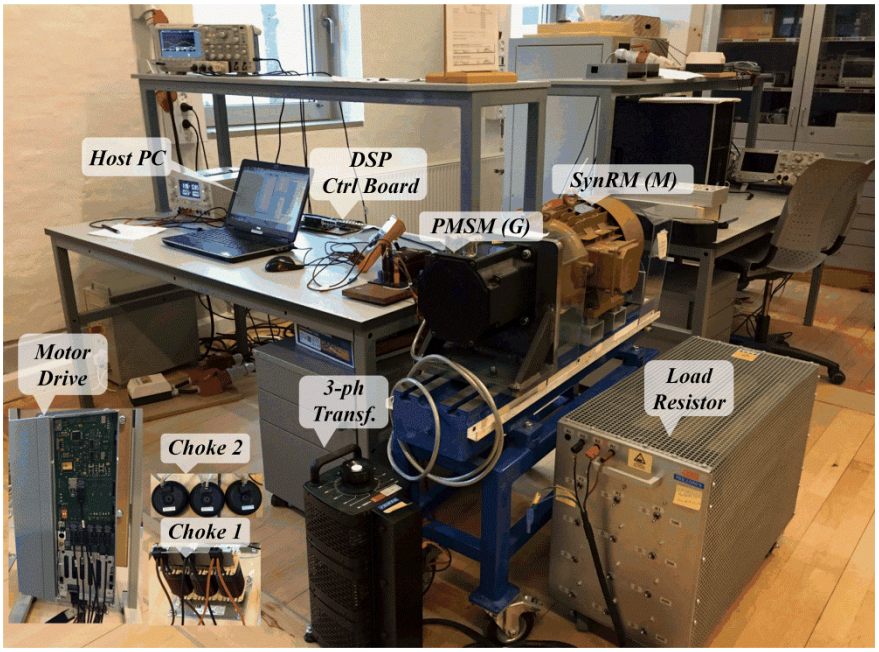

Figure 4-15 Test setup

4.6.1. Stability and Harmonics (Choke 1)

4.6.1.1 Test 1 (Choke 1 + High BW)

Figure 4-16 and Figure 4-17 show the slim dc-link drive performance under the load condition of 1500 rpm/12 A (RMS) in the case of high current controller bandwidth. Firstly, the drive without active damping control is tested, as shown in Figure 4-16 (a). Due to the effects of both a negative impedance character and low dc-link capacitance, it is seen that the dc-link voltage has oscillations whose half-period is around 700 us (715 Hz), and the peak-peak voltage variation is around 244 V. In addition, the rectifier side operates at discontinuous conduction mode (DCM), which means a bad harmonic performance to the line.

Figure 4-16 (b) shows the experimental results by using Cur_inj method under the same load conditions. By comparing with Figure 4-16 (a), the extra 715 Hz oscillations on the dc-link voltage disappear by using Cur_inj method with the gain of 0.05. Another effect is that the peak-peak dc-link voltage variation is reduced to 156 V. The interpretation of this phenomenon is that by adopting the active damping method, the unstable issue caused by CPL and reduced C_{dc} can be compensated. Furthermore, the grid current is operating in continuous conduction mode (CCM) which means an improved harmonic performance is obtained.

Similarly, the slim dc-link motor drive performance can be improved by using the active damping method of either Vol_inj or VPI. The experimental results are shown in Figure 4-16 (c) and (d) in which both the voltage gains are 1.0. Also, the extra 715 Hz oscillation disappears and the peak-peak dc-link voltage variation is reduced to 148 V and 160 V respectively, both the grid current change to flow at CCM, which means the harmonic performance is enhanced as well.

Figure 4-17 shows the FFT results of the dc-link voltage, grid current and motor current in the cases of with and without active damping control. Without active damping, the dc-link voltage has high harmonics at the order of 12^{th} and 14^{th} caused by the above mentioned oscillations. The grid current THD/PWHD is measured as 67.2% and 82.0%, and the motor current THD is 4.38%. According to the IEC 61000-3-12 standard, the harmonics requirements of the grid current cannot pass.

As seen from the harmonic analysis results in Figure 4-17 (a), the first advantage by using the active damping control is that the oscillations close to the 12^{th} and 14^{th} harmonics are effectively eliminated. The second advantage is that the grid current harmonic performance is improved dramatically, as shown in Figure 4-17 (b). The produced harmonic currents of the order of 11^{th}, 13^{th}, and 15^{th} are observed to be reduced a lot, where it is close to the oscillation frequency. However, it is still being hard to pass the specification of PWHD. Moreover, as observed from Figure 4-17 (c), the motor current THD is sacrificed, where the harmonic current at the order of 5^{th},

7th and 17th, 19th are increased to high value, so the dominant harmonic currents performance become worse.

From Figure 4-17(c), an interesting result comes out from the observation of the motor harmonics current at the order of 5th and 7th. By using Vol_inj, the motor current THD was the highest in these three types of active damping method, which means the torque performance will be the worst. In the meantime, the grid current has the lowest THD by using the same active damping method, which can be seen from Figure 4-17 (b). The interpretation of this phenomenon is that the better grid harmonic performance, the worse motor harmonic performance.

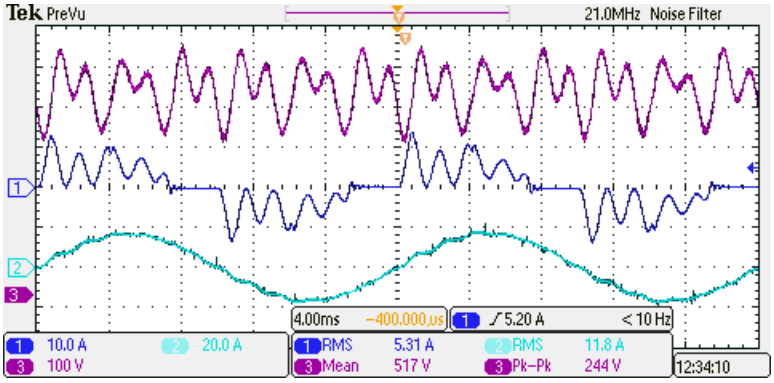

(a)

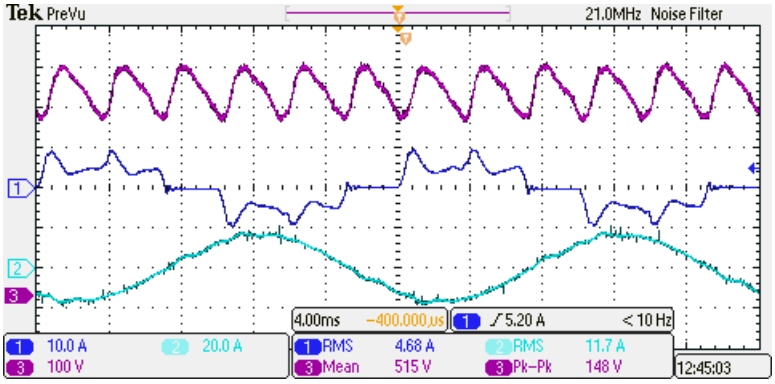

(b)

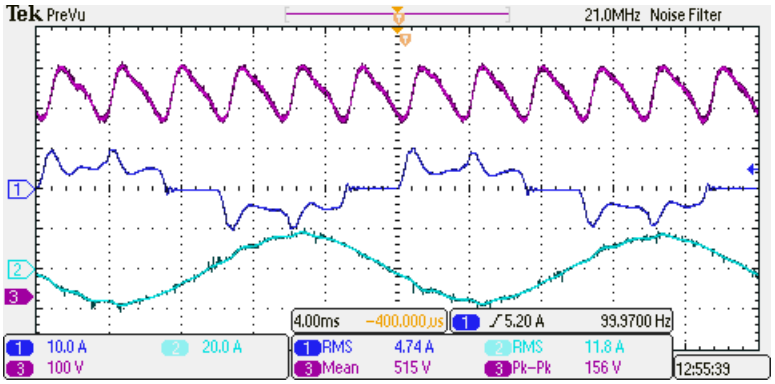

(c)

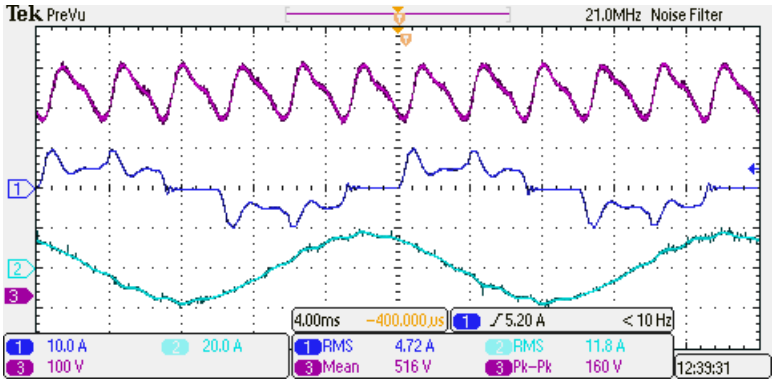

(d)

Figure 4-16 Drive performance w./o and w./ active damping control in the case of high current loop bandwidth of Test 1 (CH1: grid current; CH2: motor current; CH3: dc-link voltage). (a) w./o ADMP. (b) Cur_inj. (c) Vol_inj. (d) VPI.

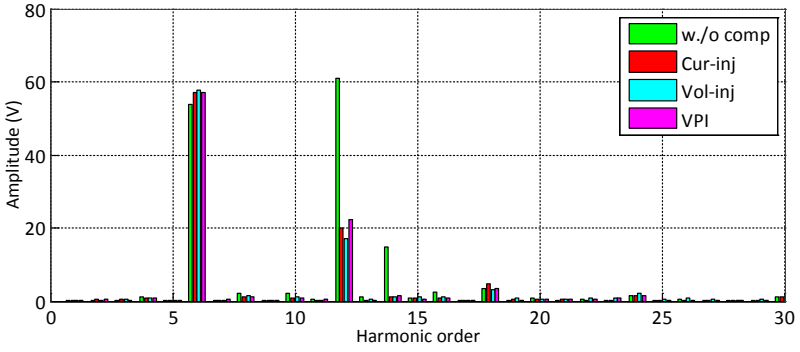

(a)

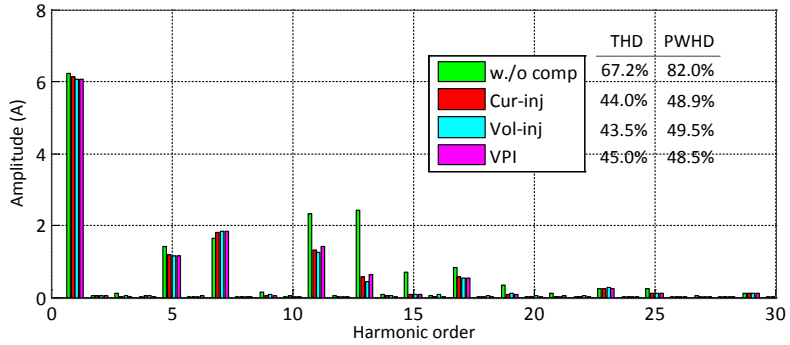

(b)

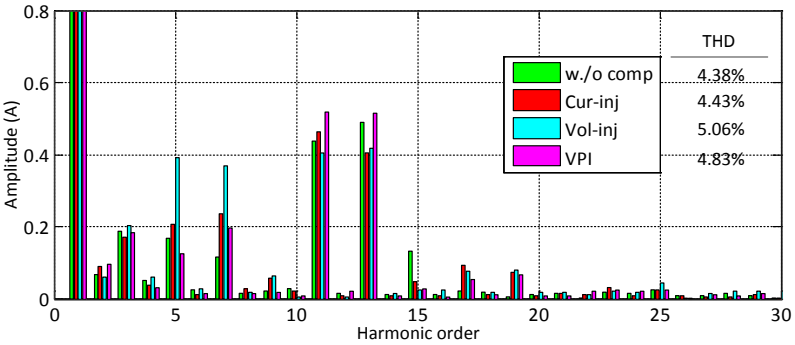

(c)

Figure 4-17 Harmonic analysis w./o and w./ the active damping control in Test 1 and $f_g = 50Hz$. *(a) DC-link voltage (only ac component). (b) Grid current. (c) Motor current.*

4.6.1.1 Test 2 (Choke 1 + Low BW)

Figure 4-18 and Figure 4-19 show the slim dc-link drive performance under the load condition of 1500 rpm/12 A in the case low current loop bandwidth. Similarly, the drive without active damping control is firstly tested, where the result is shown in

Figure 4-18 (a). Compared with *(c)* (a), the oscillation, due to both the low dc-link capacitor and negative impedance characteristic, is also observed on the dc-link voltage. But its peak-peak voltage variation is reduced to around 184 V. Besides, the grid current flows in CCM, which means an improved harmonic performance of the input current is obtained. The interpretation arises from the influence of the input impedance characteristic. As shown in Figure 4-20, when using the reduced current loop bandwidth, the input impedance characteristic changes to behave partly as the

passive impedance attribute during the middle frequency range. Therefore the drive performance is enhanced in a certain extent even without any active damping control.

Similarly, after using any of the active damping control methods, the slim dc-link motor drive performance is improved, as seen from

Figure 4-18 (b), (c) and (d). The 715 Hz oscillation in the dc-link voltage is effectively suppressed as well as the peak-peak voltage variation is reduced to around 140 V. At the same time, the grid current operates in CCM and with fewer oscillations. Moreover, the motor current distortion can easily be recognized when using the active damping control. It is worth to point out that the gain of Cur_inj is increased to 0.2 in order to obtain similar damping performance as the other two active damping methods. This means that the Cur_inj method works even under low current controller bandwidth, which is a little bit conflict with the comments as given in [82]-[84], [133].

Figure 4-19 shows the harmonic analysis results of the dc-link voltage, grid current and motor current in the cases of without and with active damping control. After activated the active damping control, the oscillation at the same frequency as Test 1 is damped greatly so that the amplitude is reduced remarkably. Consequently, seen from Figure 4-19(b), the harmonic performance of grid current is enhanced mainly at the order of 11^{th}, 13^{th}, and 15^{th}, so that the value of THD/PWHD is decreased from 51.7%/59.1% to 38.2%/51.8%, 37.9%/ 45.5%, and 37.9%/52.1% respectively. This shows that it is hard to pass the specification of PWHD by using active damping control. Likewise, the harmonics performance of motor current is getting worse, which is one disadvantage of using active damping control.

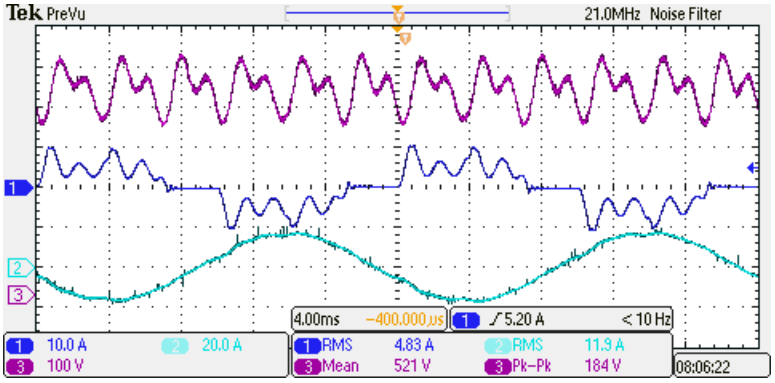

(a)

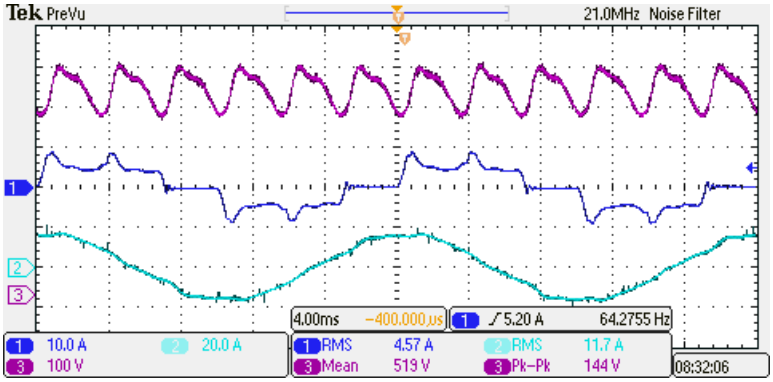

(b)

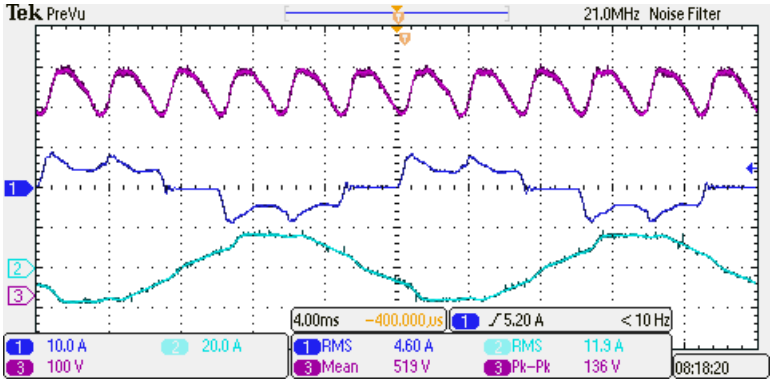

(c)

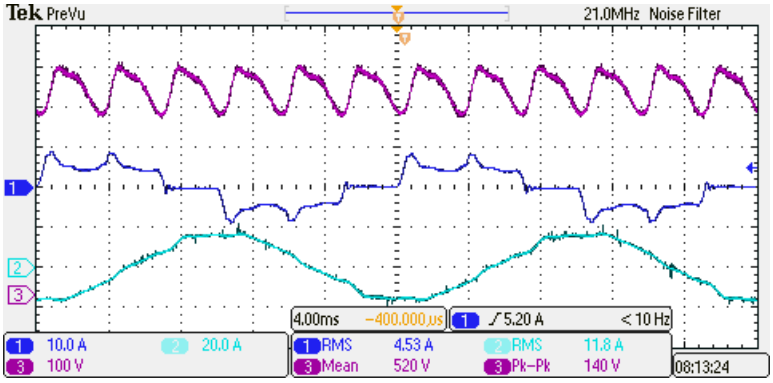

(d)

Figure 4-18 Drive performance w./o and w./ active damping control in the case of low current loop bandwidth of Test 2 (CH1: grid current; CH2: motor current; CH3: dc-link voltage). (a) w./o active damping. (b) Cur_inj. (c) Vol_inj. (d) VPI.

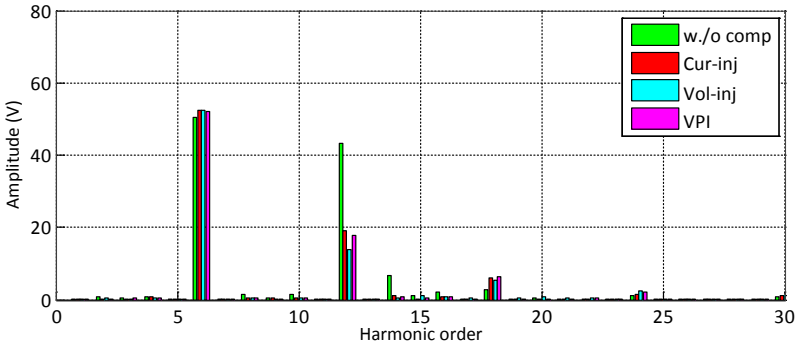

(a)

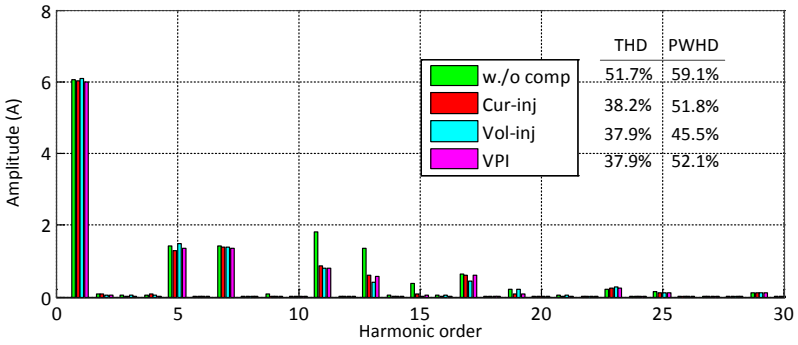

(b)

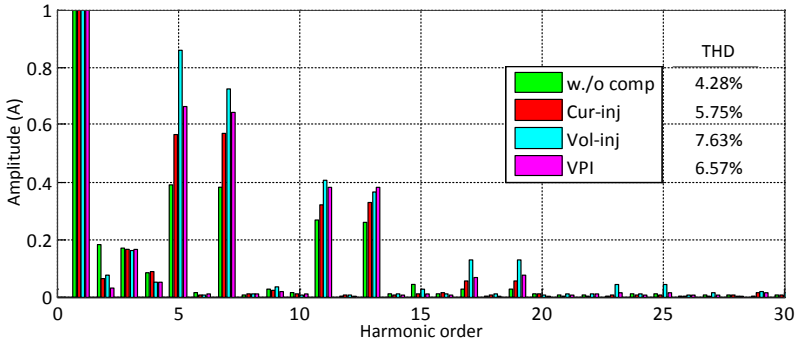

(c)

Figure 4-19 Harmonics analysis w./o and w./ active damping control of Test 2, and $f_g = 50Hz$. *(a) DC-link voltage (only ac component). (b) Grid current. (c) Motor current*

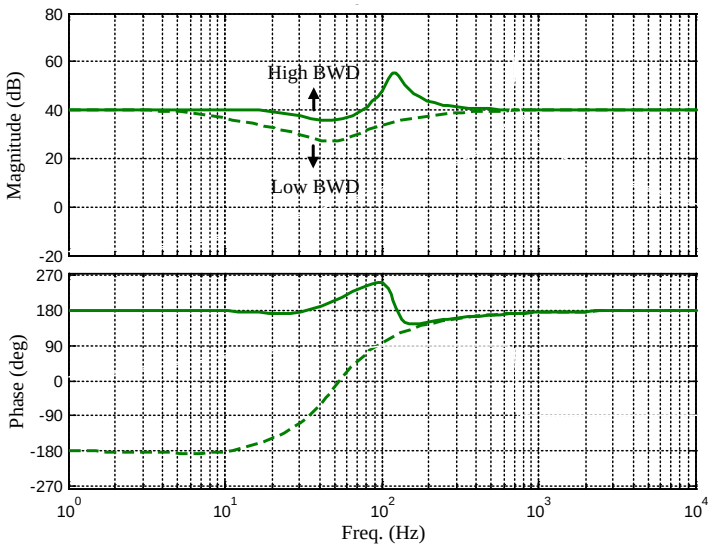

Figure 4-20 Input impedance Z_{in} with different current loop bandwidth

4.6.2. Stability and Harmonics (Choke 2)

Figure 4-21 and Figure 4-22 show the slim dc-link drive performance under the load condition of 1500 rpm 12A in the case of a low inductance Choke 2 of design 3. A significant phenomenon can be observed from Figure 4-21 that the dc-link voltage has a higher frequency oscillation but with very small amplitude. Also, it can be seen that there is not so much difference of peak-peak voltage variations between with and without active damping control. The reason is that the line resistance is large enough, which is true in some real application of low voltage grid, to damp the possible oscillation. The evidence is the very small resonant current as shown in Figure 4-21 (a).

The harmonic analysis is also performed and the results are shown in Figure 4-22. In contrast, when using the active damping control, the harmonics of dc-link voltage is slightly improved, but the harmonics current performance of grid side is greatly enhanced especially on the indicator of PWHD. At the same time, the motor current harmonic performance gets worse without any surprise.

As above mentioned, the input current harmonic THD/PWHD requirement is 48%/46%. Apparently, the Test 3 still cannot pass this requirement, and mainly because of the obtained high PWHD results. Therefore, some extra efforts are still needed in order to meet the harmonic specification. Similarly, the motor current harmonic performance goes worse as well.

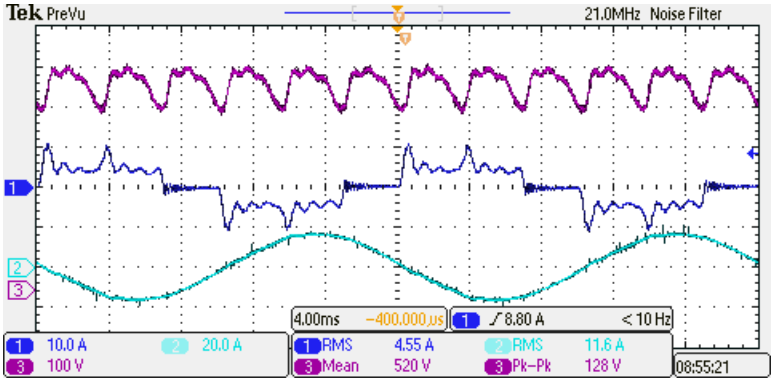
Tek PreVu
21.0MHz Noise Filter
4.00ms −400.000 µs
8.80 A
< 10 Hz
10.0 A
20.0 A
RMS 4.55 A
RMS 11.6 A
100 V
Mean 520 V
Pk-Pk 128 V
08:55:21

(a)

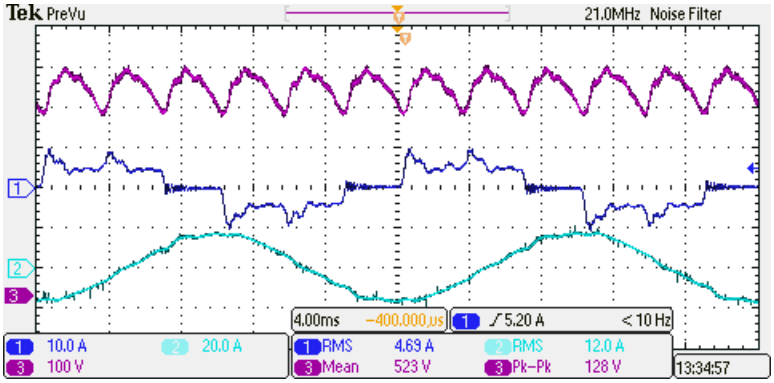
Tek PreVu
21.0MHz Noise Filter
4.00ms −400.000 µs
5.20 A
< 10 Hz
10.0 A
20.0 A
RMS 4.69 A
RMS 12.0 A
100 V
Mean 523 V
Pk-Pk 128 V
13:34:57

(b)

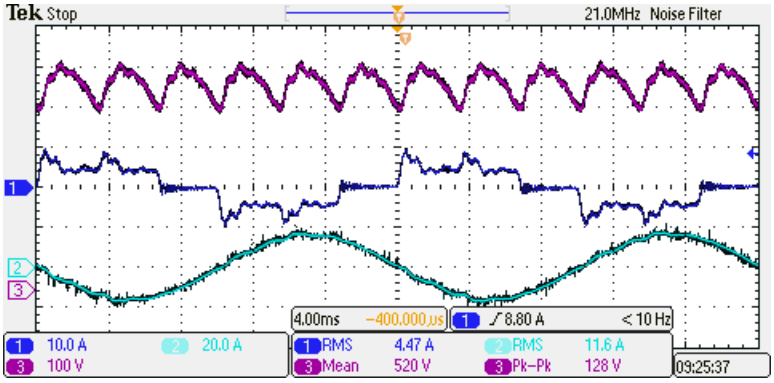
Tek Stop
21.0MHz Noise Filter
4.00ms −400.000 µs
8.80 A
< 10 Hz
10.0 A
20.0 A
RMS 4.47 A
RMS 11.6 A
100 V
Mean 520 V
Pk-Pk 128 V
09:25:37

(c)

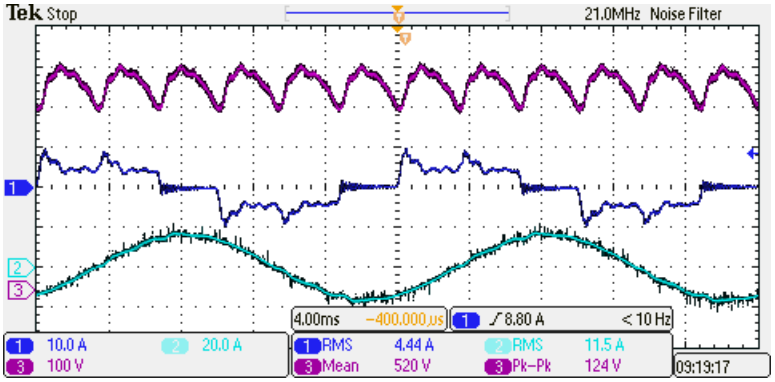

(d)

Figure 4-21 Drive performance w./o and w./ active damping control in the case of low grid inductance of Test 3 (CH1: grid current; CH2: motor current; CH3: dc-link voltage). (a) w./o active damping. (b) Cur_inj. (c) Vol_inj. (d) VPI.

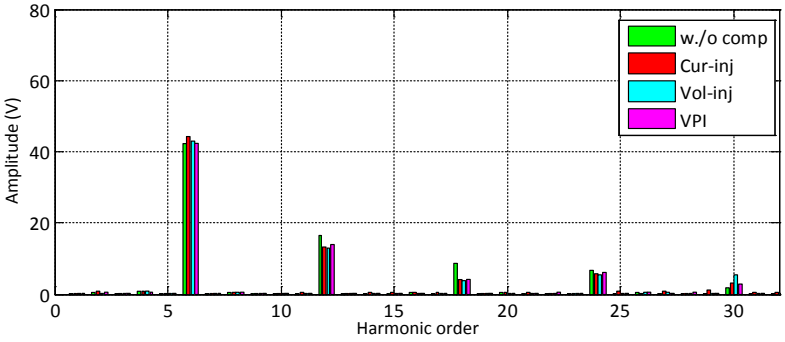

(a)

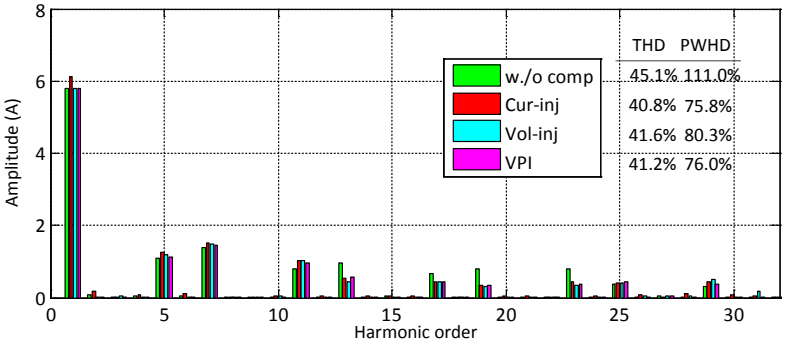

(b)

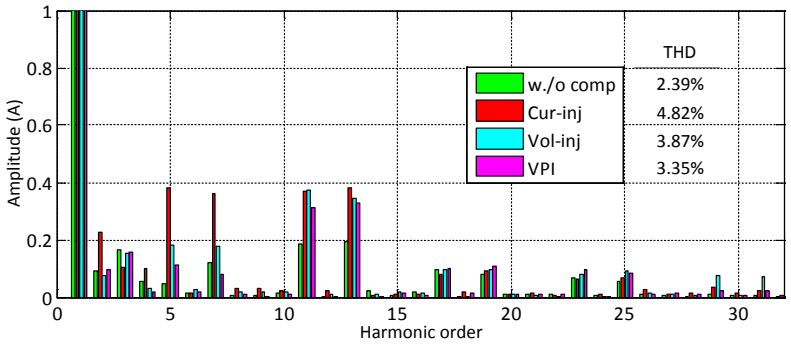

(c)

Figure 4-22 Harmonics analysis results w./o and w./ active damping control of Test 3, and $f_g = 50Hz$. (a) DC-link voltage (only ac component). (b) Grid current. (c) Motor current.

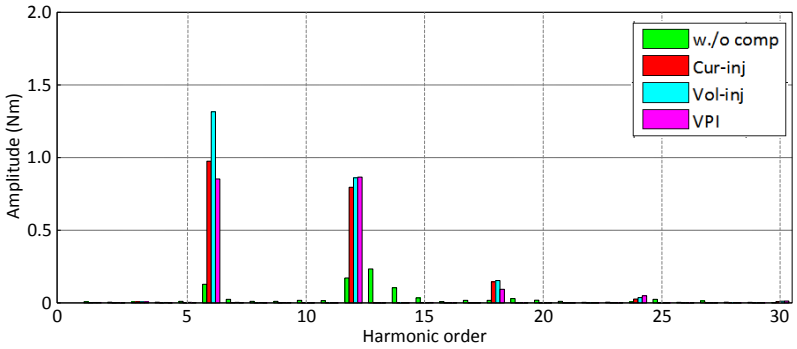

Figure 4-23 FFT analysis of electrical torque w./o and w./ active damping control of Test 1, and $f_g = 50Hz$.

4.6.3. Torque Pulsation

As previously analysed, using active damping control will increase the variation of the electrical torque. To better analyse this, Test 1 is taken as an example to be implemented in the simulation, where the cases without and with active damping control are included. Figure 4-23 shows the FFT analysis results of the electrical torque. The harmonics are intensified at the orders of $6k$, such as 6^{th}, 12^{th} and 18^{th}, which is because of the introduced dc-link voltage variation. This matches well the previous sensitivity analysis.

4.7. Summary

Two main issues (i.e., the drive system stability and the input current harmonics) of the slim dc-link drive system have been discussed in this chapter. It firstly starts with a

review of the stability criterion and how to estimate the stability performance of the slim dc-link drive system.

Then the frequency response analysis is presented to show that the active damping control can dramatically improve such drive performance. Specifically, it can effectively stabilize the drive system, and greatly enhance the grid side harmonic performance. However, one of the disadvantages of this technique is that the motor current harmonic performance goes worse. The sensitivity analyses for the motor stator voltage, electrical torque and speed have been performed due to the influence of using active damping control. According to the studies of the state-of-the-art active damping methods, the effect of the dc-link voltage variation can be seen in the slim dc-link drive.

Finally, some experimental and simulation results are selected to demonstrate the effectiveness of the theoretical analysis.

Chapter 5. Active Damping Control for Sensorless Controlled Slim DC-Link Drive

5.1. Introduction

Besides using film capacitor, using the sensorless control technique in motor drive is an additional way to achieve the benefits like high reliability, long lifetime, and cost reduction. Plenty of studies have been done to eliminate the position sensors (encoder, or resolver) started from around forty years ago [147], and many of them are being widely used today in industry.

In terms of PM machine drive, extensive sensorless control methods have been provided as well [148]. They can be classified into two categories according to rotor speed range: the high frequency signal injection based methods [149]-[152], and the fundamental frequency model based methods [153]-[161]. The first category is normally used in the low speed range, with the capability to provide high performance control even in standstill [152]. It measures the machine response after injecting a high frequency signal voltage signal, and extracts certain signals (i.e. the motor currents) having the position and speed information. The main drawbacks of the first category method are the possible acoustical noise, the losses or the decreased inverter output voltage margin [158]. The second category method is based on the fundamental frequency model of the motor drive, and it is feasible for the machine running in the middle and high rotor speed range. In this speed range, the back-EMF is high enough and can easily be detected without additional signal injection.

Specifically, the rotor information can be detected in two ways in the second category of the sensorless control methods. The first way is to use the back electromotive force (EMF) produced on the stator windings. One of the methods is shown in [154], [155], the so-called extended back-EMF method, in which the salient motor is transferred to be equivalent to a non-salient motor. When using this method, a major concern is the anti-noise-interface capability, where the back-EMF becomes low compared with a certain unknown noise in the case of a relative low rotor speed. Therefore, a proper design of an extra LPF is needed [158].

The second way is to use the stator flux linkage produced on the stator windings, which can be obtained by integration of the $\alpha\beta$-frame voltage, or by the manipulation of the dq-frame current. Compared with the method of voltage integration, the current manipulation is parameter dependent in order to obtain the flux linkage. For this reason, an adaptive disturbance observer can be used [157]. However the dynamic performance may be sacrificed in order to estimate the speed [158]. The active flux concept proposed in [156] is therefore attractive, in which a reduced order

flux observer is used to combine pros of both the voltage and current method. This principle can be understood intuitively that it presents a unified form to align the torque producing flux to the rotor axis [132].

Considering that the SynRM is one of special cases of PMSM, the sensorless control method based on active-flux concept is therefore applicable for such system. The theoretical analysis is feasible for the PM machine and SynRM, while the experiments are carried on the SynRM only. In terms of flux observer, the variable inductance as function of load is used to minimize the inductor-leaded sensitivity [159].

As stated in the previous chapters, by using the active damping control, the sensor controlled slim dc-link motor drive system can be stabilized as well as the input harmonic performance is improved. When using the sensorless control, both the stator flux observer and a phase-locked loop (PLL) are used for the controller to synchronize with the rotor so that the drive system can operate stable and smooth. Therefore, in order to study the stability and harmonic issues, it is essential to develop the model of the sensorless controlled drive system.

It is worth to note that some works have already been performed on the grid-connected power electronics converter to study the system impedance characteristic [160], [161]. Although in certain situations, the obtained small-signal model can be treated as an equivalent sensorless control model. However, the big difference is the method to obtain the "rotor" position and speed information before sending it to the PLL. It can be detected from the dq-frame voltage information in the grid converter, while an $\alpha\beta$-frame flux observer (estimator) must be employed in the motor drive. Besides, the target frequency in the grid converter is at a fixed value (50 or 60 Hz) although with some small variations.

In addition, the function of $atan2$ is commonly used to estimate the rotor position as the input to the PLL. Its small-signal model can be obtained by using the total differential formula [162]. Although the result is the same as the developed model in this chapter, the mathematical principle behind is different.

In this chapter, the small-signal model is developed for the sensorless controlled slim dc-link motor drive. The derived model is extended to the cases with the aforementioned state-of-the-art active damping methods. Following that, the system stability and harmonic performance are analyzed with the proposed model. Finally, the experimental tests are implemented to validate the effectiveness of the theoretical analysis.

5.2. System Model under Sensorless Control

The block diagram of sensorless controlled drive system is shown in Figure 5-1, in which both the motor current and dc-link voltage are measured. The superscript c

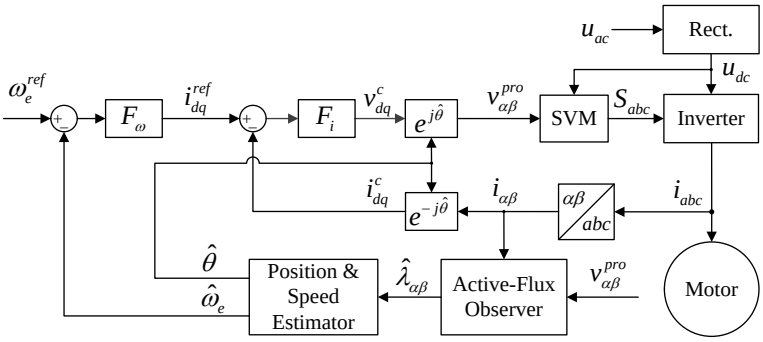

Figure 5-1 block diagram of motor drive under sensorless control

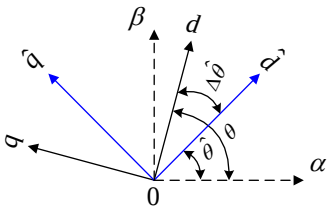

Figure 5-2 Relationship between different frame of axis for sensorless control.

means the quantity on the estimated frame, and the superscript *pro* means the quantity just before transmitting to the PWM (or SVM) block.

Under the sensorless control, there commonly exist three coordinate systems: the real $\alpha\beta$-frame, the real dq-frame and the estimated dq-frame (i.e., $\hat{d}\hat{q}$-frame). Their relationships are shown in Figure 5-2, where θ, $\hat{\theta}$ and $\Delta\hat{\theta}$ represent the real rotor position, estimated rotor position and the position error respectively.

5.2.1. Stator Flux Observer

In Figure 5-3, a stator flux observer based on the active-flux concept [156] is built on the $\alpha\beta$-frame. The rotor position θ_{cal} is calculated by the obtained active flux $\hat{\lambda}_{dAF}$ by

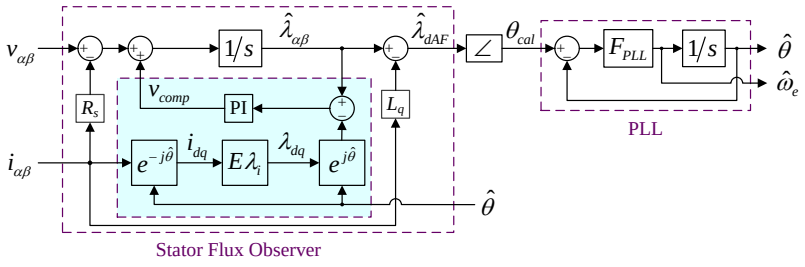

Figure 5-3 Active flux based stator flux observer and PLL used for sensorless control.

the function of "$atan2$". Thanks to the PLL, the estimated position and rotor electrical speed can be estimated accordingly. Seen from Figure 5-3, the active flux principle may be expressed as:

$$\hat{\lambda}_{dAF} = \hat{\lambda}_{\alpha\beta} - L_q i_{\alpha\beta} \tag{5.1}$$

$$\hat{\lambda}_{\alpha\beta} = \frac{1}{s}\left(v_{\alpha\beta}^{c} - R_s i_{\alpha\beta} + v_{comp}\right) \tag{5.2}$$

Substitute (5.2) into (5.1), then the active-flux can be simplified as,

$$\hat{\lambda}_{dAF} = \frac{1}{s}\left(\underbrace{v_{\alpha\beta}^{c} - Z_q i_{\alpha\beta} + v_{comp}}_{v_{\alpha\beta,AF}}\right) \tag{5.3}$$

According to the active flux principle, the calculated rotor positon can be obtained, as well as its small-signal model.

$$\theta_{cal} + \Delta\theta_{cal} = -\frac{\pi}{2} + \underbrace{\operatorname{atan2}\left(\frac{v_{\beta,AF}+\Delta v_{\beta,AF}}{v_{\alpha,AF}+\Delta v_{\alpha,AF}}\right)}_{\theta_v+\Delta\theta_v} \tag{5.4}$$

where,

$$\theta_v = \operatorname{atan2}\left(\frac{v_{\beta,AF}}{v_{\alpha,AF}}\right) \tag{5.5}$$

From (5.4), the small-signal $\Delta\theta_{cal}$ is decided by the function of $atan2$, which is introduced in computer programming language [162]. Therefore, it is a must to deduce the small signal model of $atan2$. Note that compared with the function "$atan$", the output range of $atan2$ is $(-\pi, \pi]$, not the $\left[-\frac{\pi}{2}, \frac{\pi}{2}\right]$. Therefore $atan2$ is often adopted to calculate the rotor position.

The small-signal model can be obtained according to the Taylor theorem, which is different with the partial differential equation [162]. Therefore the active voltage position $\theta_v + \Delta\theta_v$ can be extended as,

$$\theta_v + \Delta\theta_v = \operatorname{atan2}\left(\frac{v_{\beta,AF}}{v_{\alpha,AF}} + \frac{\Delta v_{\beta,AF}}{v_{\alpha,AF}} - \frac{AF}{v_{\alpha,AF}^2}\Delta v_{\alpha,AF}\right) \tag{5.6}$$

The second and third part of the right hand side in (5.6) represents the small-signal quantity. By using the Taylor theorem again, the small-signal model can be obtained as shown in (5.7). After rearranging (5.7), the small-signal model can be expressed in another form as shown in (5.8).

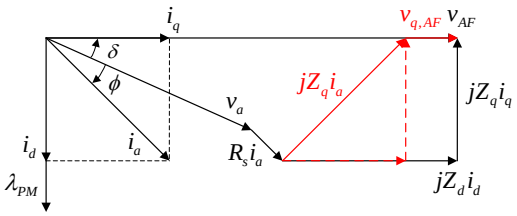

Figure 5-4 Phasor diagram for a synchronous machine showing the active-flux concept

$$\Delta\theta_v = \frac{1}{\left|v_{\alpha\beta,AF}\right|^2}\left(-v_{\beta,AF}\Delta v_{\alpha,AF} + v_{\alpha,AF}\Delta v_{\beta,AF}\right) \tag{5.7}$$

$$\Delta\theta_v = \frac{1}{\left|v_{\alpha\beta,AF}\right|}\left(-\sin\theta_v \Delta v_{\alpha,AF} + \cos\theta_v\, \Delta v_{\beta,AF}\right) \tag{5.8}$$

Besides, the voltage relationship between dq-frame and $\alpha\beta$-frame can be expressed in (5.9) according to the Park transformation.

$$\Delta v_{dq}^c = e^{-j\hat{\theta}}\Delta v_{\alpha\beta}^c = \left(\cos\hat{\theta}\,\Delta v_\alpha^c + \sin\hat{\theta}\,\Delta v_\beta^c\right) + j\left(-\sin\hat{\theta}\,\Delta v_\alpha^c + \cos\hat{\theta}\Delta v_\beta^c\right) \tag{5.9}$$

Therefore according to (5.9), (5.8) can be transferred into (5.10).

$$\Delta\theta_{cal} = \Delta\theta_v = \frac{\Delta v_{q,AF}}{\left|v_{\alpha\beta,AF}\right|} \tag{5.10}$$

In addition, the active-flux principle can be understood intuitively as shown in Figure 5-4, where the relationship between the voltage and current on the dq-frame can be observed clearly. Therefore, there exist the voltage expressions as in (5.11) and (5.12). Substitute both (5.11) and (5.12) into (5.10), then (5.13) can be obtained.

$$\left|\mathrm{v}_{\alpha\beta,\mathrm{AF}}\right| = \hat{\omega}_\mathrm{e}\left(\left(L_d - L_q\right)I_d + \lambda_\mathrm{PM}\right) \tag{5.11}$$

$$\Delta v_{q,AF} = \hat{\omega}_e\left(L_d - L_q\right)\Delta i_d^c \tag{5.12}$$

$$\Delta\theta_{cal} = \underbrace{\begin{bmatrix}\dfrac{L_d - L_q}{\left(L_d - L_q\right)I_d + \lambda_\mathrm{PM}} & 0\end{bmatrix}}_{K_{\Delta\theta\_\Delta idq}}\Delta i_{dq}^c \tag{5.13}$$

5.2.2. Phase Locked Loop (PLL)

According to Figure 5-3, the small-signal model of the PLL can be obtained by using the feedback theory.

$$\Delta\hat{\theta} = \frac{sF_{PLL}}{1 + sF_{PLL}}\Delta\theta_{cal} \tag{5.14}$$

$$\Delta\hat{\omega}_e = \frac{F_{PLL}}{1 + sF_{PLL}}\Delta\theta_{cal} \tag{5.15}$$

By substituting (5.13), the small-signal model is updated as,

$$\Delta\hat{\theta} = \underbrace{\frac{sF_{PLL}}{1 + sF_{PLL}}\begin{bmatrix}\frac{L_d - L_q}{(L_d - L_q)I_d + \lambda_{PM}} & 0\end{bmatrix}}_{G_{PLL}^{\theta}}\Delta i_{dq}^{c} \tag{5.16}$$

$$\Delta\hat{\omega}_e = \underbrace{\frac{G_{PLL}^{\theta}}{s}}_{G_{PLL}^{\omega}}\Delta i_{dq}^{c} \tag{5.17}$$

It shows that the small-signal models of the estimated position and estimated speed are a function of the estimated current in the dq-frame.

5.2.3. Current (Voltage) Transformation

In Figure 5-2, the steady-state estimated quantity can be assumed to be equal to steady-state real quantity, i.e., $\hat{\theta} = \theta$. Consequently the small variation $\Delta\hat{\theta}$ is considered as the small-signal disturbance. Therefore, the Park transformation between the estimated dq-frame and real dq-frame can be simplified as the expression in (5.18) due to a small value of $\Delta\hat{\theta}$. Therefore the small-signal model of the current and voltage vectors between the different coordinate systems can be expressed according to the relationship between two dq-frames as shown in Figure 5-2.

$$e^{-j\Delta\hat{\theta}} \approx 1 - j\Delta\hat{\theta} \tag{5.18}$$

$$i_{dq} + \Delta i_{dq} = e^{-j\Delta\hat{\theta}}\left(i_{dq}^{c} + \Delta i_{dq}^{c}\right) \tag{5.19}$$

$$\Delta i_{dq} = \Delta i_{dq}^{c} - j i_{dq}\Delta\hat{\theta} \tag{5.20}$$

$$\Delta v_{dq}^{pro} = \Delta v_{dq}^{c} - j v_{dq}^{c}\Delta\hat{\theta} \tag{5.21}$$

According to (5.14) and the small-signal voltage equation in the estimated dq-frame (which is omitted here for simplification), the expressions of the small-signal current and voltage in dq-frame can be:

$$\Delta i_{dq} = \Delta i_{dq}^{c} - j i_{dq} G_{PLL}^{\theta} \Delta i_{dq}^{c} = \underbrace{\left(I - J i_{dq} G_{PLL}^{\theta}\right)}_{\hat{G}_{PLL}^{i}} \Delta i_{dq}^{c} \tag{5.22}$$

$$\Delta v_{dq}^{pro} = F_i K F_\omega \Delta \omega_e^{ref} - \underbrace{\left(PT_1 + PT_2 + PT_3 + PT_4\right)}_{\hat{G}_{PLL}^{v}} \Delta i_{dq}^{c} \tag{5.23}$$

where,

$$PT_1 = (F_i K F_\omega - \lambda_0) G_{PLL}^{\omega} + (F_i - W) \tag{5.24}$$

$$PT_2 = J F_i K F_\omega \omega_e^{ref} G_{PLL}^{\theta} \tag{5.25}$$

$$PT_3 = J F_i K F_\omega G_p T_L G_{PLL}^{\theta} \tag{5.26}$$

$$PT_4 = -J\left(F_i K F_\omega K_T G_p + (F_i - W)\right) i_{dq}^{c} G_{PLL}^{\theta} \tag{5.27}$$

5.2.4. Motor Current, Rotor Speed and Input Impedance

According to the above small-signal models, the small-signal model of motor current Δi_{dq} can be obtained as (5.28).

$$\Delta i_{dq} = G_{\Delta i_{dq}\_\Delta \omega_e^{ref}}^{new} \cdot \Delta \omega_e^{ref} + G_{\Delta i_{dq}\_\Delta T_L}^{new} \cdot \Delta T_L + G_{\Delta i_{dq}\_\Delta U_{dc}}^{new} \cdot \Delta U_{dc} \tag{5.28}$$

where,

$$G_{\Delta i_{dq}\_\Delta \omega_e^{ref}}^{new} = \frac{D F_i K F_\omega}{\underbrace{Z_M + \lambda_0 K_t G_p + D G_{PLL}^{v}\left(G_{PLL}^{i}\right)^{-1}}_{Den\_\Delta i_{dq}\_new}} \tag{5.29}$$

$$G_{\Delta i_{dq}\_\Delta T_L}^{new} = \frac{\lambda_0 G_p}{Den\_\Delta i_{dq}\_new} \tag{5.30}$$

$$G_{\Delta i_{dq}\_\Delta U_{dc}}^{new} = \frac{G_{dc}}{Den\_\Delta i_{dq}\_new} \tag{5.31}$$

Similar with the sensored control, the motor current Δi_{dq} under sensorless control is the sum of three products between the input quantities $\Delta \omega_e^{ref}$, ΔT_L, ΔU_{dc} and their corresponding transfer functions.

Moreover, the closed-loop transfer function of the current Δi_{dq} and estimated speed $\Delta \hat{\omega}_e$ can be derived as well as shown in (5.32) and (5.33).

$$G^{new}_{cl\_\Delta i_{dq}\_\Delta i^{ref}_{dq}} = \frac{DZ_M F_i}{Z_M + \lambda_0 K_t G_p + G^{v,cl\_i_{dq}}_{PLL}/G^{i}_{PLL}} \tag{5.32}$$

$$G^{new}_{cl\_\Delta\widehat{\omega}_e\_\Delta\omega^{ref}_e} = G^{new}_{cl\_\Delta i_{dq}\_\Delta i^{ref}_{dq}} DKF_w / \left(1 + G^{new}_{\Delta\widehat{\omega}_e\_\Delta\omega^{ref}_e}\right) \tag{5.33}$$

where,

$$G^{v,cl\_i_{dq}}_{PLL} = (F_i - W) - \lambda_0 G^{\omega}_{PLL} + JW i_{dq} G^{\theta}_{PLL} \tag{5.34}$$

$$G^{new}_{\Delta\widehat{\omega}_e\_\Delta\omega^{ref}_e} = G^{\omega}_{PLL} G^{i}_{PLL} G^{new}_{cl\_\Delta i_{dq}\_\Delta i^{ref}_{dq}} KDF_\omega K_t N_{pp}/J_t \tag{5.35}$$

In addition, the small-signal model of rotor speed can be obtained as well.

$$\Delta\omega_e = G^{new}_{\Delta\omega_e\_\Delta\omega^{ref}_e} \cdot \Delta\omega^{ref}_e + G^{new}_{\Delta\omega_e\_\Delta T_L} \cdot \Delta T_L + G^{new}_{\Delta\omega_e\_\Delta U_{dc}} \cdot \Delta U_{dc} \tag{5.36}$$

where,

$$G^{new}_{\Delta\omega_e\_\Delta\omega^{ref}_e} = K_t G_p G^{new}_{\Delta i_{dq}\_\Delta\omega^{ref}_e} \tag{5.37}$$

$$G^{new}_{\Delta\omega_e\_\Delta T_L} = K_t G_p G^{new}_{\Delta i_{dq}\_\Delta T_L} - G_p \tag{5.38}$$

$$G^{new}_{\Delta\omega_e\_\Delta U_{dc}} = K_t G_p G^{new}_{\Delta i_{dq}\_\Delta U_{dc}} \tag{5.39}$$

Substitute the collection of these models into the power balance equation as shown in Chapter 4, then the input impedance model can be obtained as given in (5.40).

$$Y^{new}_{in} = Y_{CPL} + \underbrace{C_{Yctrl} G^{new}_{\Delta idq\_\Delta Udc}}_{Y^{new}_{ctrl}} \tag{5.40}$$

Figure 5-5 shows the block diagram of the relationship of (5.28) and (5.36). Also, the interpretation of (5.40) is shown in Figure 5-6. Together with the incremental negative

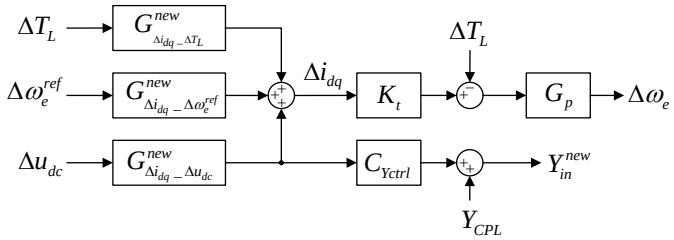

Figure 5-5 Small-signal model of motor drive system under sensorless control

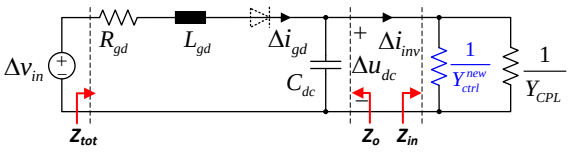

Figure 5-6 Equivalent system impedance under sensorless control

impedance due to CPL characteristic, the influence of sensorless control based on the active-flux concept is highlighted in the input admittance (or impedance) of the drive system.

5.2.5. Output Impedance

For the sake of completeness, the output impedance Z_o in (4.16), as shown in Figure 5-6, can be re-written here.

$$Z_o = \frac{sL_{gd} + R_{gd}}{s^2 L_{gd} C_{dc} + sR_{gd} C_{dc} + 1} \tag{5.41}$$

5.3. Small-Signal Model with Active Damping Control

Still, the state-of-the-art active damping control methods mentioned in last chapter are investigated here but now the motor drive system is under sensorless control. Figure 5-7 shows the block diagram of the small-signal model in the case of with active damping control methods. Similarly, compared with the original case without active damping control, the transfer function in terms of Δu_{dc} is reasonably changed due to the dc-link voltage Δu_{dc} is directly injected into the motor controller. A good example is the case when using the active damping method of VPI. However, when using the other two active damping methods (i.e. Cur_inj, Vol_inj), the introduced Δu_{dc} will affect the small-signal transfer functions on the load ΔT_L as well as the rotor speed reference $\Delta \omega_e^{ref}$. As shown in Figure 5-7, the highlighted red block means that its

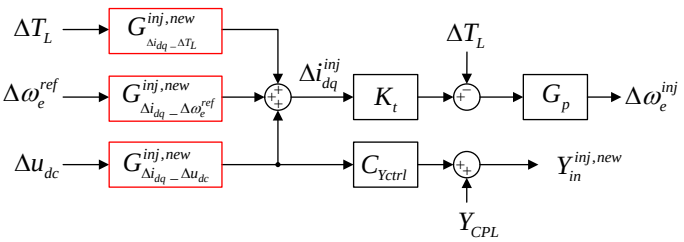

Figure 5-7 Small-signal model of motor drive system w./ active damping control under sensorless control

transfer function is updated as well in a sensorless controlled drive system.

The new transfer functions of the highlighted block due to the active damping control are shown in the (4.17)-(5.46).

$$G_{\Delta i_{dq}\_\Delta u_{dc}}^{inj,new} = \begin{cases} \dfrac{G_{dc} + DF_i g_{iq}}{Den\_\Delta i_{dq}\_new + DG_{PLL}^{vdc,cur\_inj}\left(G_{PLL}^{i}\right)^{-1}}, & (if\ Cur\_inj) \\ \dfrac{G_{dc} + Dg_{vq}}{Den\_\Delta i_{dq}\_new + DG_{PLL}^{vdc,vol\_inj}\left(G_{PLL}^{i}\right)^{-1}}, & (if\ Vol\_inj) \\ \dfrac{G_{dc\_VPI}}{Den\_\Delta i_{dq}\_new}, & (if\ VPI) \end{cases} \tag{5.42}$$

where,

$$G_{PLL}^{vdc,cur\_inj} = JF_i g_{iq} U_{dc} \tag{5.43}$$

$$G_{PLL}^{vdc,vol\_inj} = Jg_{vq} U_{dc} \tag{5.44}$$

and

$$G_{\Delta i_{dq}\_\Delta \omega_e^{ref}}^{inj,new} = \begin{cases} \dfrac{DF_i KF_\omega}{Den\_\Delta i_{dq}\_new + DG_{PLL}^{vdc,cur\_inj}\left(G_{PLL}^{i}\right)^{-1}}, & (if\ Cur\_inj) \\ \dfrac{DF_i KF_\omega}{Den\_\Delta i_{dq}\_new + DG_{PLL}^{vdc,vol\_inj}\left(G_{PLL}^{i}\right)^{-1}}, & (if\ Vol\_inj) \\ \dfrac{G_{dc}}{Den\_\Delta i_{dq}\_new}, & (if\ VPI) \end{cases} \tag{5.45}$$

and

$$G_{\Delta i_{dq}\_\Delta T_L}^{inj,new} = \begin{cases} \dfrac{\lambda_0 G_p}{Den\_\Delta i_{dq}\_new + DG_{PLL}^{vdc,cur\_inj}\left(G_{PLL}^{i}\right)^{-1}}, & (if\ Cur\_inj) \\ \dfrac{\lambda_0 G_p}{Den\_\Delta i_{dq}\_new + DG_{PLL}^{vdc,vol\_inj}\left(G_{PLL}^{i}\right)^{-1}}, & (if\ Vol\_inj) \\ \dfrac{\lambda_0 G_p}{Den\_\Delta i_{dq}\_new}, & (if\ VPI) \end{cases} \tag{5.46}$$

By means of these equations, the small-signal model of the dq-frame current and rotor speed using active damping control can be derived by the following (5.47) and (5.48) separately.

$$\Delta i_{dq}^{inj} = G_{\Delta i_{dq}\_\omega_e^{ref}}^{inj,new} \cdot \Delta\omega_e^{ref} + G_{\Delta i_{dq}\_\Delta T_L}^{inj,new} \cdot \Delta T_L + G_{\Delta i_{dq}\_\Delta u_{dc}}^{inj,new} \cdot \Delta U_{dc} \tag{5.47}$$

$$\Delta\omega_e^{inj} = \underbrace{K_t G_p G_{\Delta i dq\_\omega_e^{ref}}^{inj,new}}_{G_{\Delta\omega_e\_\omega_e^{ref}}^{inj,new}} \cdot \Delta\omega_e^{ref} + \underbrace{(K_t G_{\Delta i_{dq}\_\Delta T_L}^{inj,new} - 1) G_p}_{G_{\Delta\omega_e\_\Delta T_L}^{inj,new}} \cdot \Delta T_L + \underbrace{K_t G_p G_{\Delta i_{dq}\_\Delta u_{dc}}^{inj,new}}_{G_{\Delta\omega_e\_\Delta U_{dc}}^{inj,new}} \cdot \Delta U_{dc} \tag{5.48}$$

Thereafter, the input impedance using active damping control for the sensorless controlled motor drive system, according to Figure 5-7, can be derived where the unified expression is shown in (5.49).

$$Y_{in}^{new,inj} = Y_{CPL} + \underbrace{C_{Yctrl} G_{\Delta i_{dq}\_\Delta u_{dc}}^{inj,new}}_{Y_{ctrl}^{inj,new}} \tag{5.49}$$

5.4. Analysis of System Stability and Input Current Harmonics

5.4.1. Frequency Characteristic of Open-Loop Model

Applying the derived model for a SynRM drive system gives the Nyquist diagram of the open-loop transfer function for the current control loop, whose results are shown in Figure 5-8. Each of the trajectories is not encircling the (-1, j0) under both heavy and light load conditions, as shown in Figure 5-8 (a) and (b). It means that the current loop is stable not only at light load but also at heavy load.

As shown in Figure 5-2, the position error may exist between the estimated rotor position and the real when using sensorless control. Besides the inductance variation, the fact of mismatched estimated rotor position may lead to the effect that the coupling between the d-axis and q-axis cannot be totally eliminated, when using the decoupling function block W. This can be seen from Figure 5-8 (b), in which the trajectories of G_{idq} and G_{iqd} are plotted. Therefore, the coupling block is not a must as well as when the drive system operates with sensorless control.

From above analysis, it can be seen that there are two speed loops during sensorless control. One is the real speed loop whose output is the real rotor speed $\Delta\omega_e$. The other is the estimated speed loop whose output is the estimated rotor speed $\Delta\widehat{\omega}_e$. And the inputs of both speed loops are the same. Figure 5-9 shows the Bode diagrams of these two open speed loops under sensorless control. The blue curve is the frequency characteristic of the open loop gain of the real speed loop, which can be thought close to the sensored control. The green curve is the frequency characteristic of the open loop gain of the estimated speed loop. One can see that both the speed loops are stable. In addition, the bandwidth of the estimated speed loop is slightly smaller than the real at high load conditions, and the magnitude of the estimated is also steeper. The interpretation of the difference is that using sensorless control may increase the stability performance and the ability of high frequency suppression.

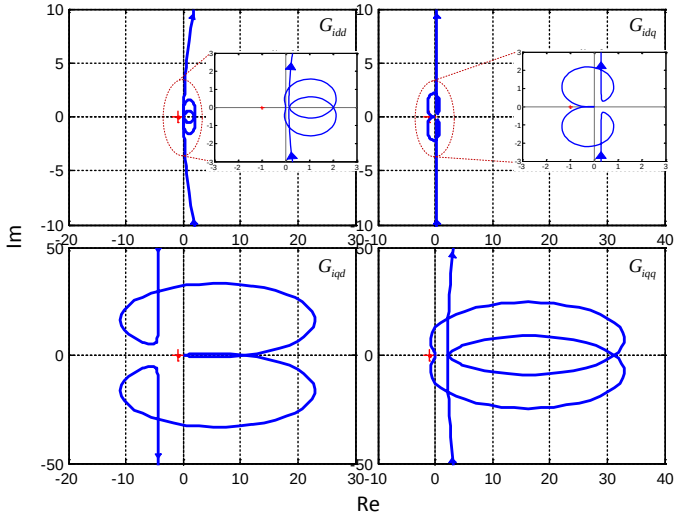

(a)

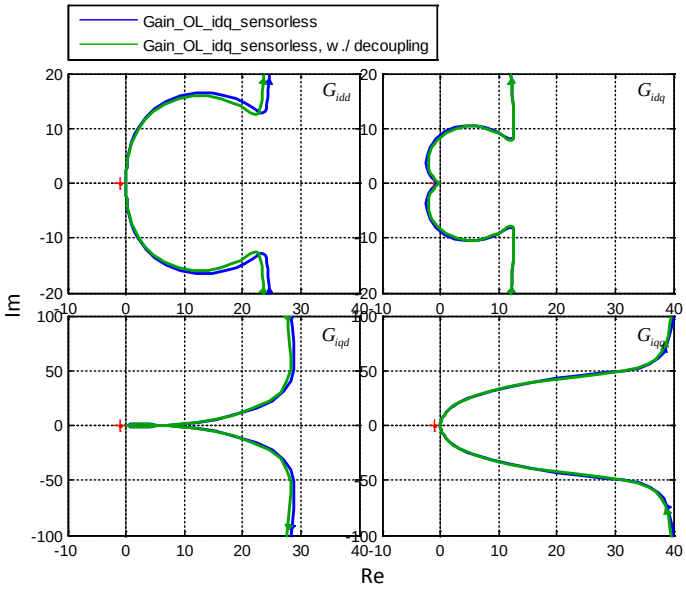

(b)

Figure 5-8 Nyquist plot of the current-loop under sensorless control. (a) 1500 rpm/15 N·m. (b) 100 rpm/2 N·m w./o and with decoupling function.

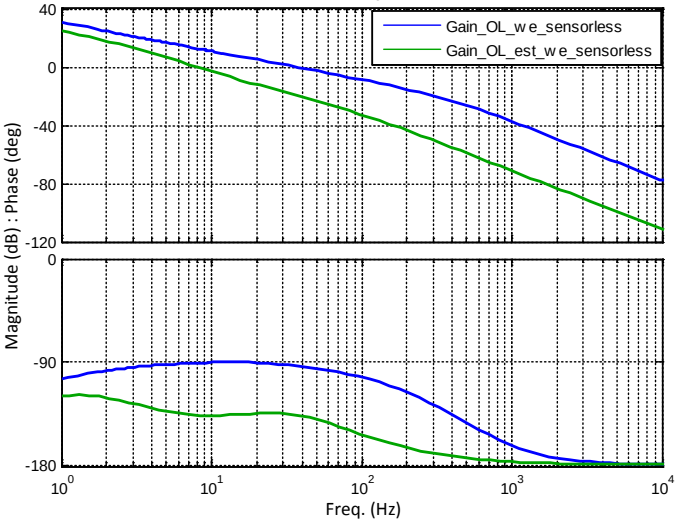

(a)

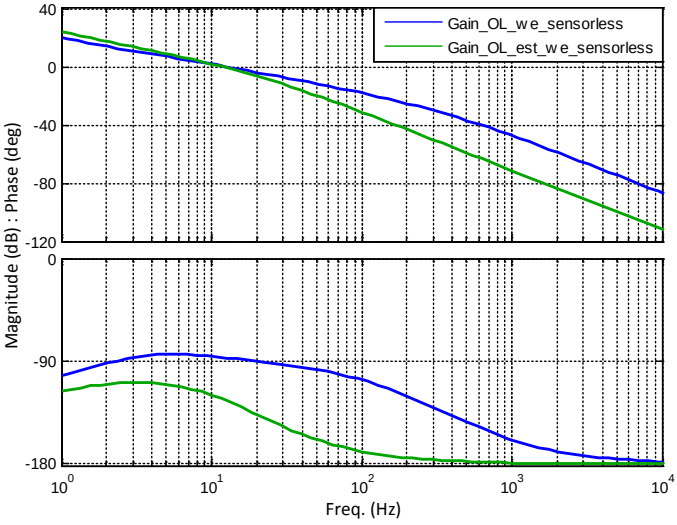

(b)

Figure 5-9 Bode diagram of speed loop under sensorless control. (a) 1500 rpm/15 N·m. (b) 100 rpm/2 N·m.

5.4.2. System Stability Analysis

In terms of the sensorless controlled slim dc-link drive, same as Chapter 4, it is also possible to use the criterion of ESAC [137] to do the stability analysis by checking the ratio between the source output impedance and the load input impedance. Compared

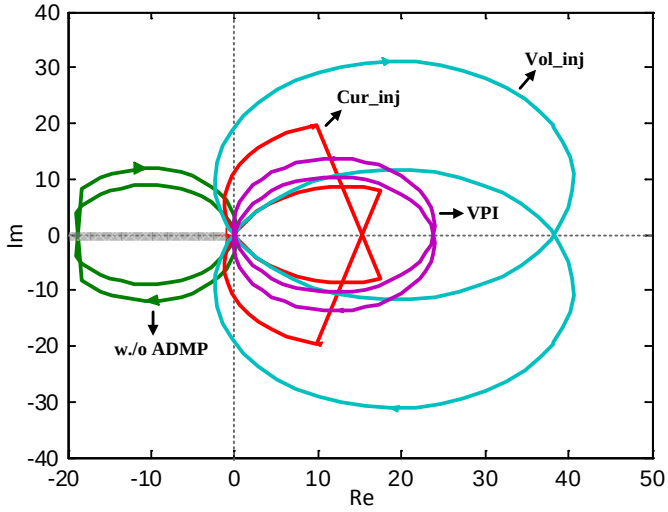

Figure 5-10 Nyquist diagram of the minor-loop gain for the cases of w./o and w./ active damping control, where the system is under sensorless control.

with the sensored control, only the input impedance is changed when using sensorless control according to the developed model in (4.21).

Figure 5-10 shows the Nyquist diagram of the minor-loop gain for the cases of with and without active damping control under sensorless control. It can be seen that the green curve is located at left side plane, and intersects with the ESAC defined forbidden area, which means that the slim dc-link motor drive system behaves unstable in this situation. In the opposite situation, when activating any active damping method, the Nyquist trajectory shifts away to the right side plane, so that there is no intersection with the ESAC defined forbidden area. It means that the sensorless controlled slim dc-link drive system will be operating in stable state if using any active damping control.

The stability analysis can also be done from the relationship between the input impedance and output impedance. Figure 5-11 shows the frequency characteristic of the input and output impedances. It can be observed that when the active damping control is not activated, the input impedance behaves as the negative impedance, and when compared with the output impedance, the phase difference is larger than 180 degree above the resonant frequency (seen from the output impedance). This means that the system is unstable. On the contrary, when using any active damping control, the input impedance tends to be passive, and the phase difference becomes nearly 90 degree above the resonant frequency of the output impedance. This means that the system is in stable operation. Moreover, if compared with Figure 4-9, it also can be seen that the phase and resonance at low frequency range is changed as well in the case without active damping control, which is the effect of sensorless control.

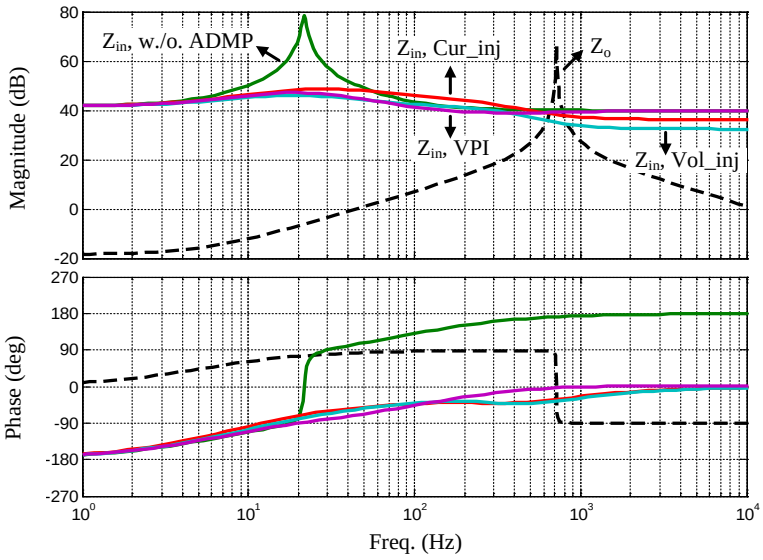

Figure 5-11 Simulated input impedance Z_{in} and output impedance Z_o in the cases w./ and w./o active damping control, where the drive system is under sensorless control.

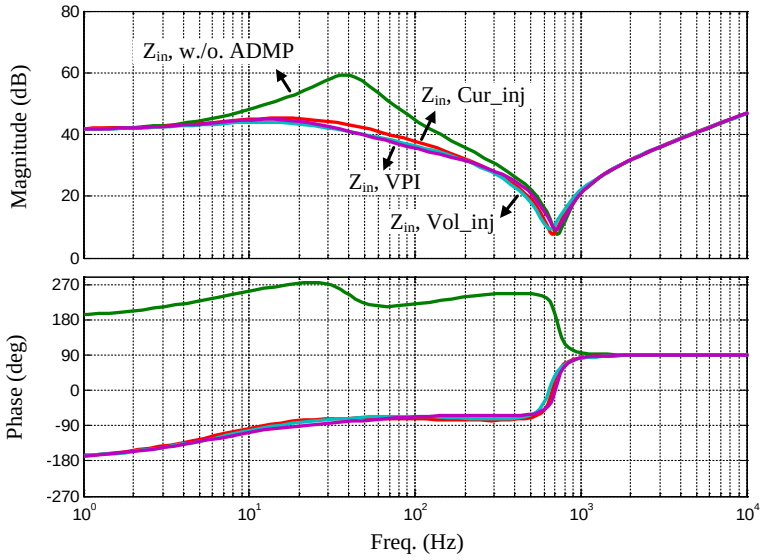

Figure 5-12 Simulated total impedance Z_{tot} in the cases w./ and w./o active damping control, where the drive system is under sensorless control.

5.4.3. Input Harmonics Performance

After using active damping control in the sensorless controlled slim dc-link drive system, the load input impedance is reshaped to be passive above the resonant frequency of output impedance, which is similar with the analysis of the sensored controlled slim dc-link drive in Chapter 4. Therefore, the characteristic of total input impedance Z_{tot} (Seen from Figure 5-6) will subsequently be changed. Eventually, the input harmonic performance might be influenced.

Figure 5-12 is the frequency characteristic of the total input impedance based on the derived model. It can be seen that after using active damping control, the amplitude of total impedance becomes smaller as well as the frequency range is below the resonant frequency of Z_o. Also, the resonance is suppressed by the induced passivity of Z_{in}, so that the amplitude of the harmonic voltage source caused by LC resonance is attenuated. Therefore compared with the sensored control, similar results of are obtained when analyzing the input harmonic performance when using sensorless control in the slim dc-link drive.

The difference of total input impedance between sensorless and sensor controlled slim dc-link drive (cf. Figure 4-10), is the increased amplitude in the middle frequency range and increased phase angle in the low frequency range. The main reason is the influence of the bandwidth of PLL when using the sensorless control. The following experimental results will bring much help to understand the impact on the input harmonic performance due to the sensorless control in a slim dc-link drive.

5.5. Sensitivity Analysis

5.5.1. Torque/Speed Sensitivity

The electrical torque and speed are influenced by the active damping control. Similar as the analysis in Chapter 4, the root cause is that the induced harmonics on the stator voltage will transferred to the electrical torque and speed eventually. The expressions of the resulting torque and speed sensitivity can be derived as:

$$S_{T_e} = \begin{cases} K_t G^{new}_{\Delta i_{dq}\_\Delta u_{dc}} \ (if\ w./o\ ADMP) \\ K_t G^{inj,new}_{\Delta i_{dq}\_\Delta u_{dc}} \ (if\ w./\ ADMP) \end{cases} \tag{5.50}$$

$$S_{\omega_e} = \begin{cases} K_t G_p G^{new}_{\Delta i_{dq}\_\Delta u_{dc}} \ (if\ w./o\ ADMP) \\ K_t G_p G^{inj,new}_{\Delta i_{dq}\_\Delta u_{dc}} \ (if\ w./\ ADMP) \end{cases} \tag{5.51}$$

The frequency response of the torque sensitivity in the cases with and without active damping control is shown in Figure 5-13. In the low frequency region, there is no much difference in these cases. By comparing with Figure 4-12 where the sensor

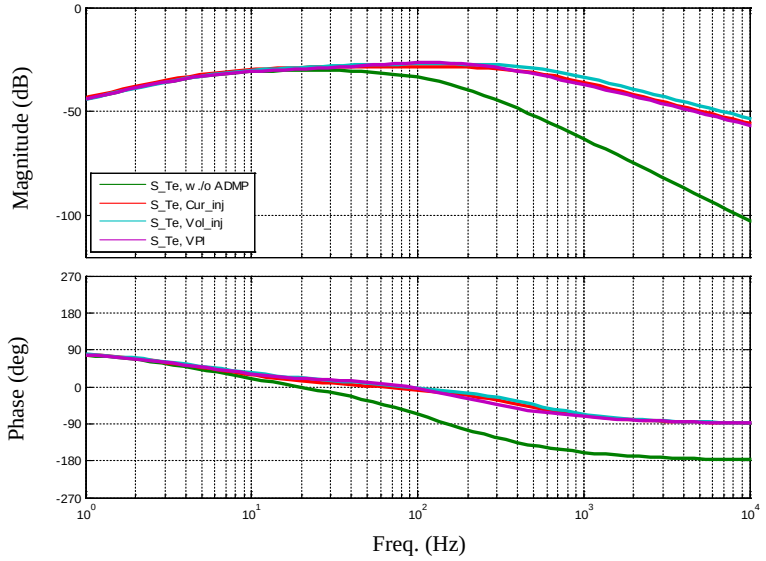

Figure 5-13 Electrical torque sensitivity in the cases w./ and w./o. active damping when using sensorless control

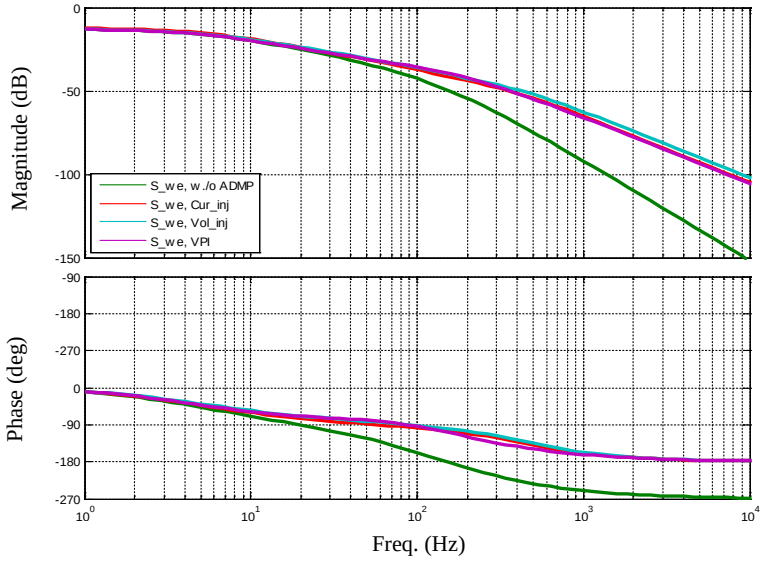

Figure 5-14 Electrical speed sensitivity in the cases w./ and w./o. active damping when using sensorless control

control is used, the amplitude and phase characteristics are changed, which is because of the effect of the sensorless control. In the middle to high frequency region, the torque sensitivity is increased which is because of the active damping control. However, the maximum sensitivity is still below -20 dB even in the worst case.

As for the speed sensitivity, the main difference, compared with the torque sensitivity, is the effect of a first–order system G_p which can be seen from the difference between (5.50) and (5.51). Figure 5-14 shows the Bode diagrams of the speed sensitivity.

Similarly, the $6kf_g$-order harmonics, such as 600 Hz, 900 Hz, may appear on the dc-bus voltage when using active damping control, so that the Bode diagram of electrical torque/speed sensitivity may content the corresponding harmonics component.

5.6. Experimental and Simulation Results

A sensorless controlled slim dc-link SynRM drive system is used to verify the effectiveness of above theoretical analysis. The system parameters are:

- Motor: same as the parameters in Chapter 4.
- Drive: same as the parameters in Chapter 4, and the grid inductor uses the Choke 1(=1.47 mH) as well.
- High BW: current controller bandwidth = 200 Hz /1500 Hz, gain of Cur_inj = 0.05, gain of Vol_inj = 1.00, gain of VPI = 1.00.
- Test 5: Choke 1 + high BW.

The test setup is reused the one in Chapter 4, as shown in Figure 4-15. The slim dc-link capacitor is a 14.0 μF film capacitor.

5.6.1. Stability and Harmonics

5.6.1.1 Experimental Results Analysis

Figure 5-15 and Figure 5-16 show the experimental results of the sensorless controlled slim dc-link drive under the load condition of 1500 rpm, 12 A (RMS). As can be seen from Figure 5-15 (a) in the case without active damping control, the dc-link voltage has oscillations and the peak-to-peak voltage variation is around 232 V, as well as the grid current is flowing in DCM. Same as the previous analysis, the oscillations are caused by both the negative impedance character of Z_{in} and the low dc-link capacitance.

Figure 5-15 (b)-(d) show the experimental results by using three active damping control methods under same load condition. The oscillations on the dc-link voltage are eliminated effectively so that only a 300 Hz voltage variation is mainly kept at the first glance. The peak-to-peak dc-link voltage variation is also reduced to 156 V, 144 V and 156 V for each corresponding active damping method. Also, the grid current flow

changes from DCM to CCM with any of the active damping control, which will be very helpful to improve the input harmonic performance. The motor current has some changes with or without active damping control, but it is hard to distinct the difference only by pure observations.

Figure 5-16 shows the FFT results of the dc-link voltage, grid current and motor current in the cases of with and without active damping control in the sensorless controlled slim dc-link drive. In Figure 5-16 (a), the harmonics with active damping control are reduced greatly in the range of from 10^{th} to 17^{th}, i.e. [500, 850] Hz. The interpretation is the dc-link voltage oscillation caused by LC resonance is effectively suppressed. In Figure 5-16 (b), the grid current THD/PWHD are also reduced from 67.2%/82.0% to 44.5%/50.7%, 43.2%/48.1% and 46.0%/50.6% for each of the active damping method respectively. However, the THD of motor current is certainly increased as it can be seen from Figure 5-16 (c).

Based on the experimental results, it can be concluded that by using any of the active damping control in the sensorless controlled slim dc-link drive, the oscillation caused by CPL and low dc-link capacitance can be compensated so that the system stabilization target can be realized. The dc-link voltage oscillation can be effectively suppressed, and the input current harmonic performance can be greatly improved as well. However, the harmonic performance of the motor current becomes worse. This matches with the above theoretical analysis.

Similarly, the estimated short circuit ratio R_{sce} is nearly 100 in this test, and the requirement of THD/PWHD of the input current is that it should be lower than 40.0%/40.0%. From the experimental results, although the harmonic performance is greatly improved, the standard requirement is not achieved.

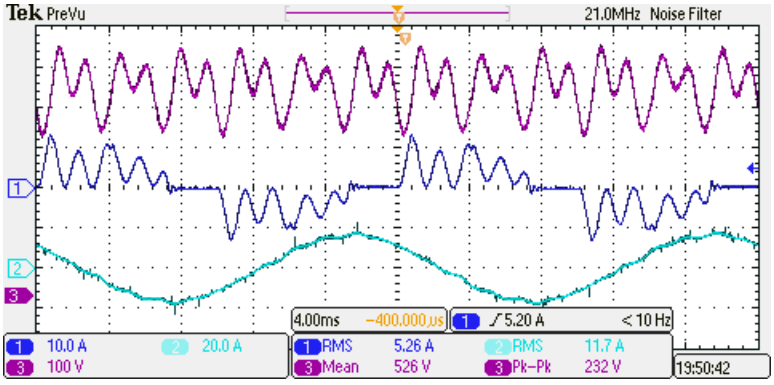

(a)

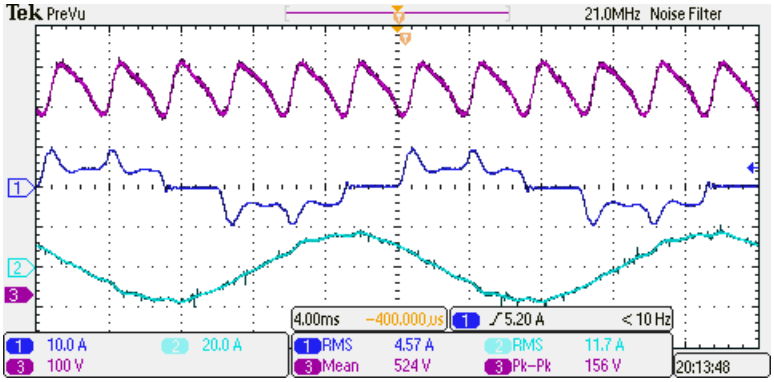

(b)

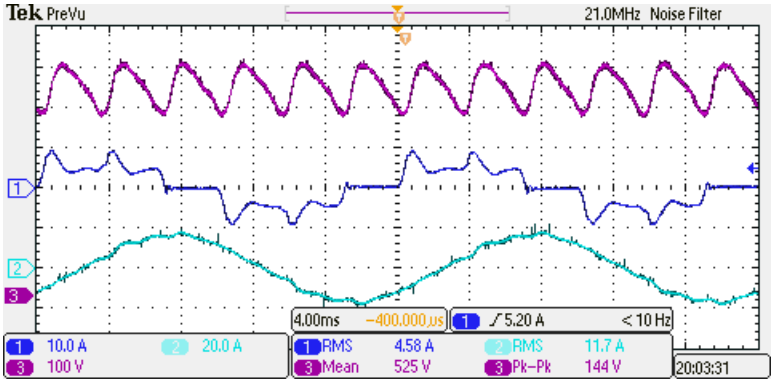

(c)

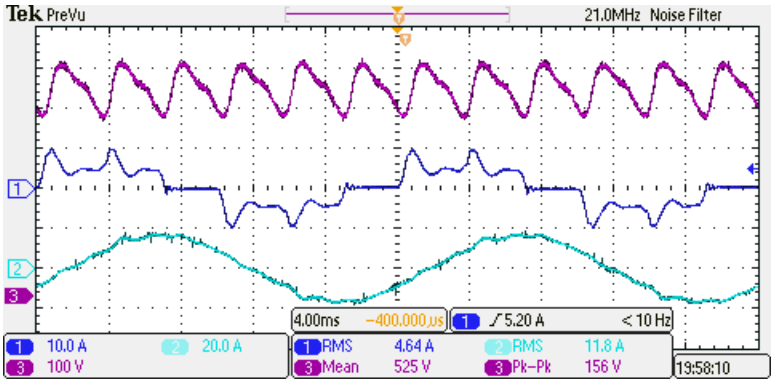

(d)

Figure 5-15 Drive performance w./o and w./ active damping control in Test 5 under sensorless control (CH1: grid current; CH2: motor current; CH3: dc-link voltage). (a) w./o ADMP. (b) Cur_inj. (c) Vol_inj. (d) VPI.

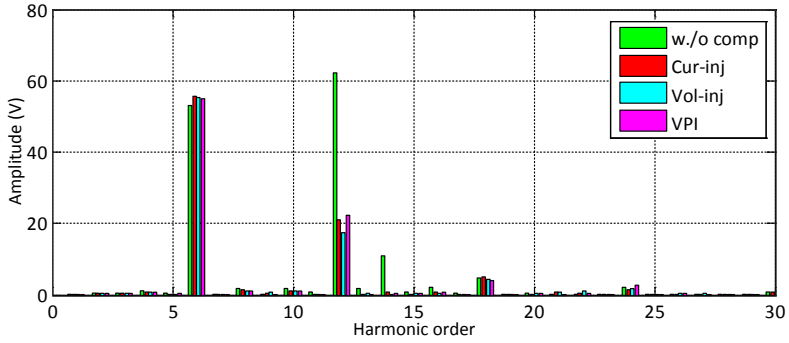

(a)

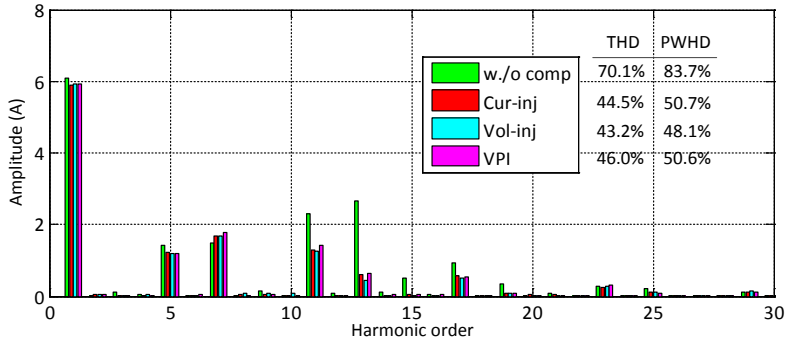

(b)

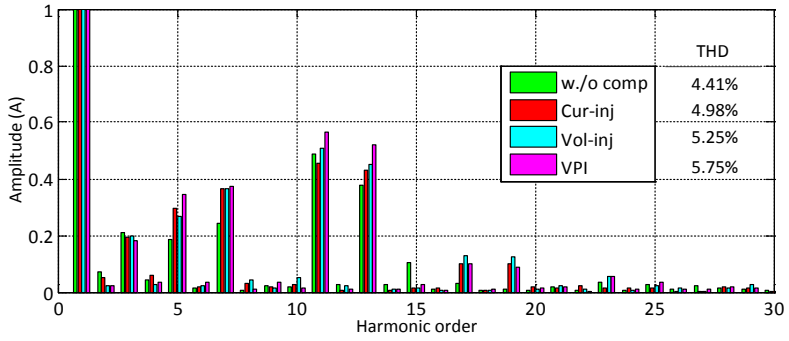

(c)

Figure 5-16 Harmonics analysis results w./o and w./ ADMP control of Test 5 when using sensorless control, and $f_g = 50\text{Hz}$. (a) DC-link voltage (only ac component). (b) Grid current. (c) Motor current.

5.7. Summary

This chapter proposes a modeling method for the sensorless controlled slim dc-link motor drive, and extends it for the cases when using the state-of-the-art active damping methods. Based on the developed small-signal model, both the impact of the induced dc-link voltage variation and the effect of the active damping control are detailed analyzed in terms of the stability and harmonic issues.

The experimental tests are carried out to verify the theoretical analysis on a slim dc-link SynRM drive system test setup. According to the test results, using active damping control can stabilize the sensorless controlled slim dc-link drive system, and improve the input harmonics performance dramatically. But, it may still need some more effort to improve the gaps if to pass the standard requirement of the input current harmonics. Besides, the motor current performance is sacrificed a little bit as well.

Chapter 6. Active Circuit Scheme for Slim DC-Link Drive

6.1. Introduction

As already known, the root causes of the instability issue in slim dc-link drive are the incremental negative impedance characteristic for a CPL [64], [73], [78] and the extra reduced dc-link capacitance [75], [86], [108], [133]. Using active damping control can stabilize slim dc-link drive system under both sensored and senseless control. However, the resulting input harmonics performance, especially the PWHD, still needs to be improved in order to meet the harmonic standard requirement. Besides, the harmonic performance of the motor current is degraded to some degree as well.

Besides the active damping control schemes (i.e. software-based), the hardware-based schemes are proposed as well to attempt to solve one or two issues in the recent years. For example, either the passive damping [70] or using shunt compensator [88] are presented in order to improve the stability performance, and either the dc-link APF [163] or the EI together with silicon controlled rectifier (SCR) [164] are addressed to improve the harmonic performance. However, the parameters of the scheme in [70] are not flexible when the different system specifications are used, the harmonic performance in [88] may not be good enough in the case of weak grid or large grid impedance. Generally, the scheme in [163] or [164] can be used for the high-end application with high demanded harmonic performance, but the total physical cost and the system lifetime may be the main concern if used for the other applications.

A new hardware-based scheme is therefore proposed to solve the instability and the harmonic issues along with the benefit of low cost and also being electrolytic capacitor free. In this chapter, the principle of the proposed scheme is present firstly. Then, the verified simulations are implemented for both cases (i.e., using the active damping methods and using the proposed scheme). In the meantime, the comparative results are given to show their pros and cons. Finally, the sensitivity analyses are done in terms of both the stator voltage and torque sensitivity.

6.2. Principle of Proposed Scheme

From Figure 6-1, the principle of active damping control can be understood intuitively that it employees the motor inductor into the resonant tank (i.e. L_{gd} and C_{dc}), so that the resonant tank operates like a LCL circuit. As explained in [108] and [86], part of the resonant energy is transferred back and forth between the motor winding and the equivalent dc-link, so that the system damping factor is increased and the resonance is damped. Because the motor inductor (i.e., L_d or L_q) involves in the resonant tank,

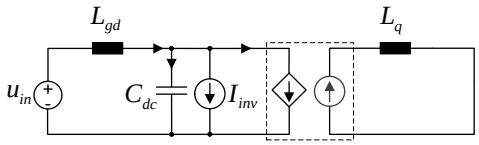

Figure 6-1 Equivalent resonant tank involved the L_q using active damping control [108], [86]. I_{inv} represents the avearage dc current load of inverter.

part of resonance current inevitably superimposes to the motor current (Note that both two windings L_d and L_q are involved in when using the VPI method). In this way, the resonance of the input current is reduced, so that the input harmonic performance is improved. However, the torque/speed will subsequently be influenced and the sensitivity is thus increased. Nevertheless, as discussed in previous chapters, the PWHD performance of input current may still be a problem when feeding with a large grid inductance.

Therefore, it is essential to find a solution to the instability and harmonics issue without the above mentioned shortcomings. The first idea comes out by producing an equivalent voltage variation to compensate the voltage difference between the output of rectifier and the dc-link capacitor (or dc-bus voltage closed to inverter), which is classified as Voltage-Source (VS) scheme. Since this scheme does not involve the motor windings, the motor shaft performance will not be affected. A similar concept has been implemented in ac-dc-dc converter [165], and good results are achieved.

Another idea is to introduce an extra power circuit to run with dc-link capacitor directly. The first concept is to using an equivalent "inductor" to mimic the function of motor winding, which can be realized by a power circuit as shown in Figure 6-2 (a). In this way, the motor winding is replaced by the extra "inductor", so that the system can be stable and it does not affect the torque/speed performance. The second concept is to compensate the resonant current directly by using the power circuit as shown in Figure 6-2 (b). In this way, the resonances on the dc-link voltage can be effectively compensated, so that the targets, including the system stability and without impact on

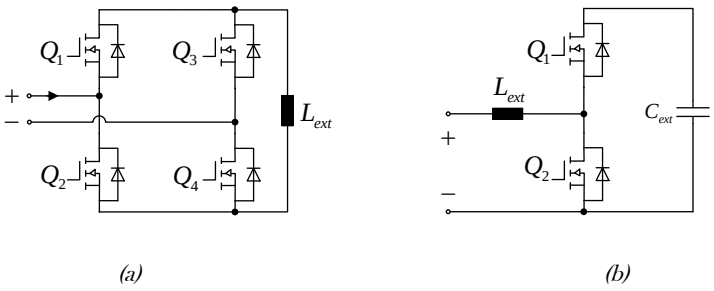

Figure 6-2 Current-source concept. (a) Full Bridge circuit. (b) Boost circuit.

the torque/speed performance, can be achieved.

According to the second idea, each output current in each circuit, as shown in Figure 6-3, is provided to be equal to the resonant current of the dc-link capacitor, so that the resonance is subsequently transferred into the power circuit and there is no resonance in the dc-link capacitor under ideal conditions. These two concepts can be classified as the current-source (CS) scheme. Due to a patent pending proposal, the design details will not be discussed here, but part of the simulation results are shown in the following section.

6.3. Simulation Studies

To verify the effectiveness of the proposed scheme, the simulations are carried on via a slim dc-link SynRM drive system. The system parameters are close to the test setup in Chapter 4, which are:

- Motor: Same as Section 4.6 but the load torque = 15 Nm.
- Drive: Same as Section 4.6, but a different grid inductor L_g (= 0.70 mH) is used (marked as Choke 3).
- Low current controller BW: only in the case of BW = 60 Hz /200 Hz.
- Case 1: Choke 1 + Active Circuit.
- Case 2: Choke 3 + Active Circuit.

When using Choke 1 and Choke 3, the corresponding R_{sce} is estimated as 100 and 205 respectively, therefore the THD/PWHD requirements are 40.0%/40.0% and 48.0%/46.0% separately (c.f. IEC 61000-3-12). Based on the same system parameters, the simulations of the state-of-the-art active damping methods are also implemented. By comparing with using the active damping control, the benefits of the proposed scheme can be seen from the simulation results.

6.3.1. Stability and Harmonics Analysis

Figure 6-4 shows the simulation results of the slim dc-link drive for the case of a low R_{sce} , where a load condition of 1500 rpm/15 Nm with the Choke 1 is used. It can be seen that, without any compensation, the harmonics appeared on the dc-bus and input current are very high, but the harmonics in motor current is low. The measured THD/PWHD of the input current harmonic is 93.0%/235.6%. After using the active damping control, these resonant harmonics are effectively suppressed and the input harmonic performance is dramatically improved, as shown in Figure 6-4 (b). Simultaneously, the motor current harmonic performance becomes worse.

In comparison, seen from Figure 6-4, when using the proposed active circuit scheme, the harmonics are greatly eliminated in the dc-link voltage, the input current, and the motor current. Thus, the harmonic performance of the dc-link voltage and input

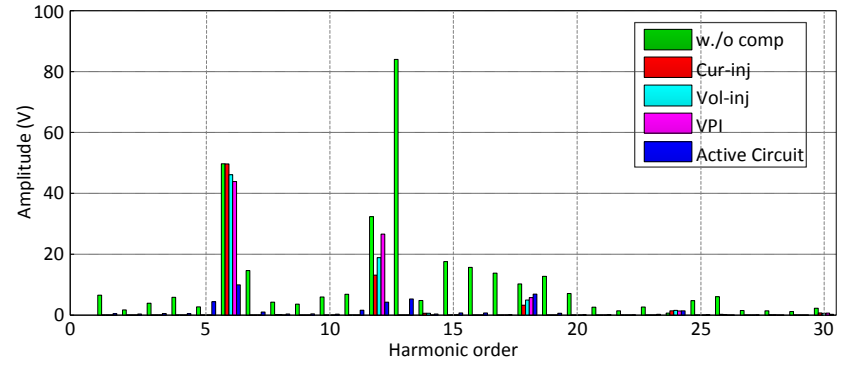

(a)

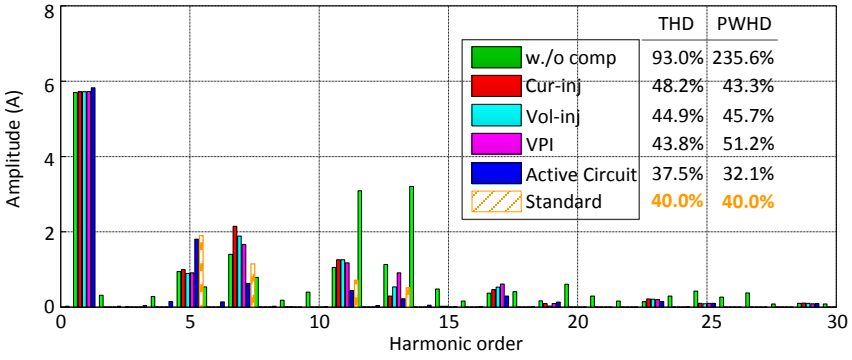

(b)

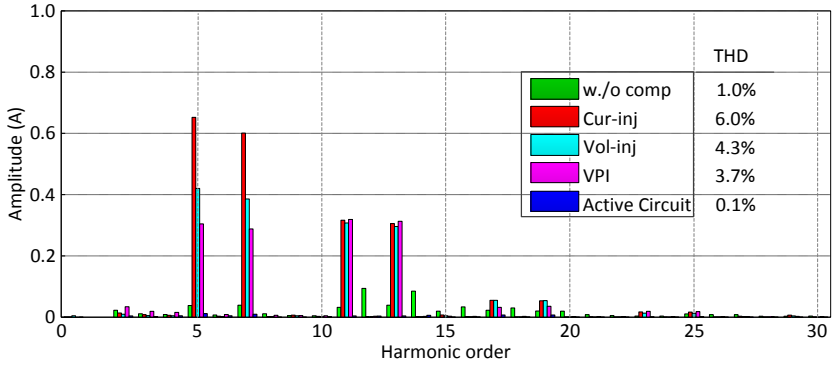

(c)

Figure 6-4 Harmonic analysis results comparison by using active damping control and proposed scheme in Case 1, and $f_g = 50\text{Hz}$. *(a) DC-link voltage (only ac component). (b) Grid current. (c) Motor current.*

current are dramatically improved. Besides, the harmonic performance of the motor current becomes better as well. Specifically, compared with the case of using the active damping method, a much better harmonics performance of input current can be achieved when using the proposed active circuit scheme, so that the harmonics requirement of the standard can be passed, even for the relevant harmonic current. In addition, the motor current harmonic performance is not influenced.

It is worth noting that these results are similar as the theoretical analysis and experimental results in Chapter 4, but still there exist some differences. One difference is the values of improved input harmonics are higher than the experimental results. Another difference is the values of the sacrificed motor current harmonics are lower than the experimental results. The main reason could be the equivalent resistance of the smaller equivalent series resistors are underestimated in both the grid impedance and line cable, which will increase the damping effect for the resonance on the dc-link.

Figure 6-5 shows the simulation results of the slim dc-link drive performance in the case of a high R_{sce}, where it is a load condition of 1500 rpm/15 Nm and the Choke 3 is used. It can be seen that the similar results can be gotten compared with Case 1.

When using active damping control, the resonance on the dc-link voltage can be eliminated, but there is not so much improvement on the 6^{th} and 12^{th} harmonics. The THD of the input current is reduced similarly which can pass the standard requirement, but the PWHD, as the the results of remaining high harmonics current (e.g. 7^{th}, 11^{th} and 13^{th}), is still one of the weak points which cannot pass the standard requirement. Same as in previous case, the motor current harmonics performance becomes worse.

In comparison, all of the harmonics performance becomes better when using the proposed active circuit scheme. The 6^{th} and 12^{th} harmonics are reduced, and the PWHD of the input harmonics is improved so that the system input harmonics performance can meet the standard requirement. Again, the motor current harmonic performance is very good. These results match with the above discussion of the original idea as well.

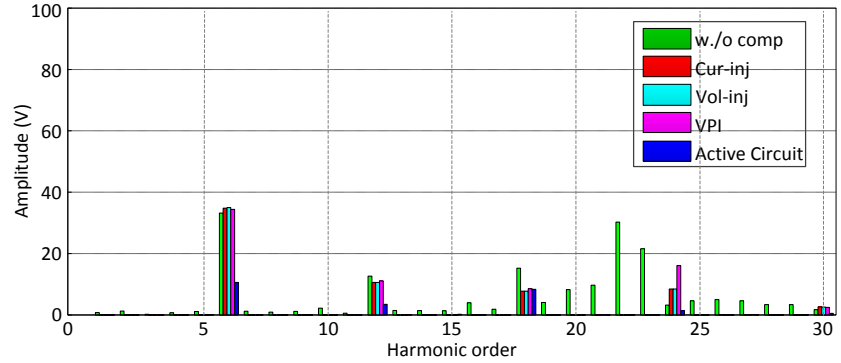

(a)

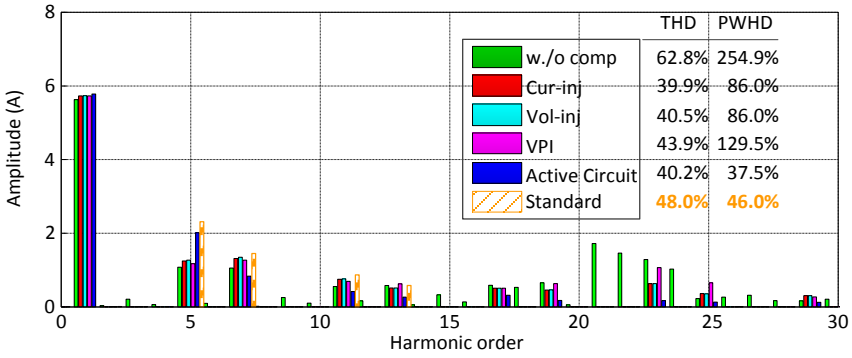

(b)

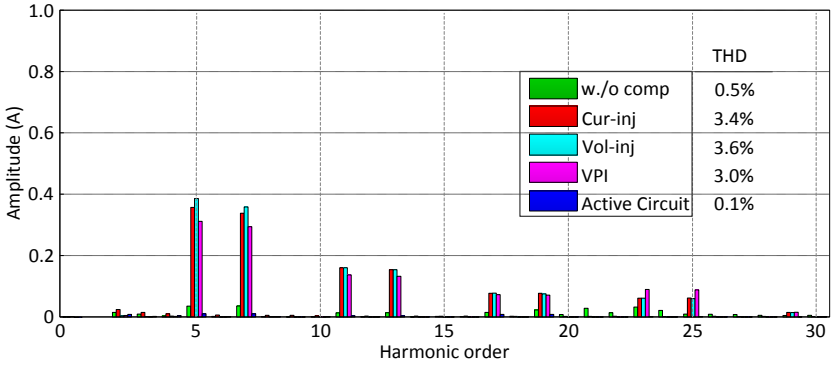

(c)

Figure 6-5 Harmonic analysis results comparison by using active damping control and proposed active circuit in Case 2, and $f_g = 50Hz$. (a) DC-link voltage (only ac component). (b) Grid current. (c) Motor current.

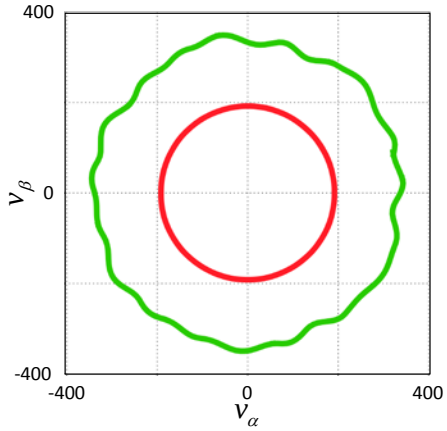

Figure 6-6 Stator voltage and dc-link voltage under the proposed scheme of Case 1. Green: dc-bus voltage. Red: stator voltage command.

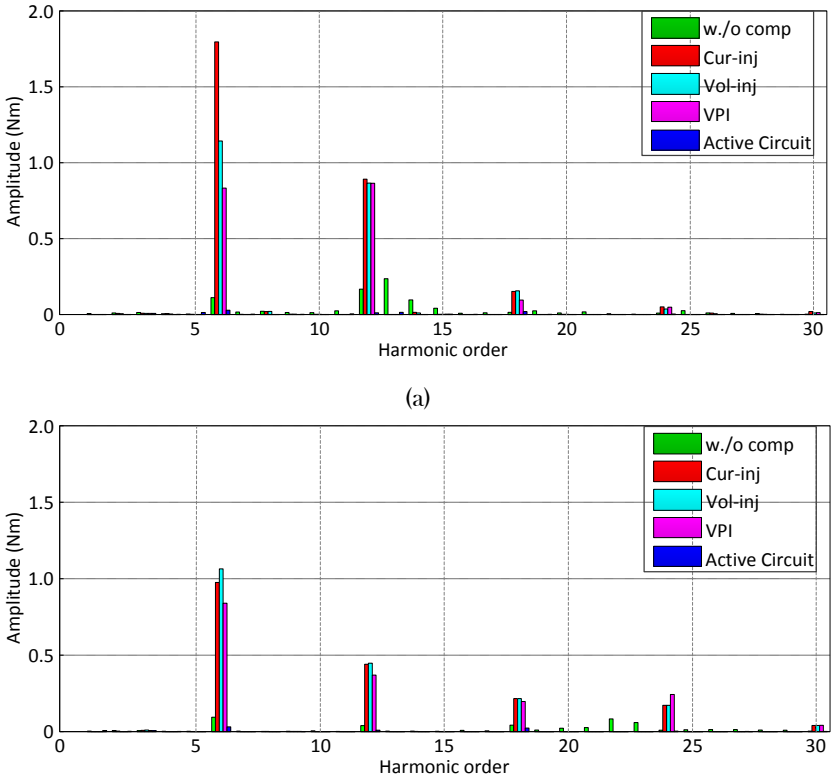

Figure 6-7 Electrical torque ripple comparison when using active damping control and proposed active circuit scheme, and $f_g = 50Hz$. (a) Case 1. (b) Case 2.

6.3.2. Sensitivity of Stator Voltage and Electrical Torque

Figure 6-6 shows the simulated stator voltage and dc-link voltage in $\alpha\beta$-frame when using the proposed active circuit scheme. In this figure, the voltage command (i.e., the red cycle) is smooth, which means there is no command to produce harmonics on the stator voltage. Accordingly, a motor current with a good harmonic performance can be obtained. Along with that, the variation of the dc-link voltage is also smaller as shown in the green cycle, compared with the results when using the active damping control (seen from Chapter 4).

Figure 6-7 shows the comparison of the resulting torque ripples between using the active damping control and using the proposed scheme. When using the active damping control, the torque harmonics (or ripples) are increased in both cases, which is same as the theoretical analysis and experimental results as given in Chapter 4. In contrast, when using the proposed active circuit scheme, the resulting torque harmonics (or ripples) are very small so that they almost cannot be seen.

6.4. Summary

This chapter proposes an active circuit scheme to solve both the instability and harmonics issues comprehensively in a slim dc-link drive. It analyzes the root cause of the shortcomings when using the active damping control. Then it addresses the principle of the proposed active circuit scheme. Finally, the simulations on two different R_{sce} cases are implemented in order to verify the effectiveness of the proposed scheme. The simulation results match with the theoretical analyses, and show its advantages compared with using the active damping methods.

In summary, when using the proposed scheme, a low dc-link voltage variation and a good input harmonic performance can be achieved along with a good motor current harmonic performance in the slim dc-link motor drive. Therefore, both the system instability and harmonics issues may be solved simultaneously by using the proposed active circuit scheme.

Chapter 7. Conclusion

The purpose of this chapter is to conclude the PhD work, summarize the main scientific contributions, and give the possible future work.

7.1. Summary

Slim dc-link drive is a hot application in order to obtain the high input harmonics performance, combined with the benefits of cost-effectiveness and long lifetime. This research project mainly focuses on two challenging techniques in such type of drive, i.e. the system instability and input current harmonic, especially when feeding by a large grid inductor.

In Chapter 1, the background was presented for this project. The research scope and objectives were listed as well as the thesis organization.

In Chapter 2, the state-of-the-art literatures were overviewed on the slim dc-link motor drive especially regarding the two issues. It started from the active damping control, to the harmonic analysis method, and the harmonic performance improvement methods. This overview described the background and provided also a bench mark for this research.

In Chapter 3, a general TFM-based model was developed for the cases that the current controller bandwidth is same and different between d- and q-axis. The derived model is also feasible for both the PMSM and SynRM application. The developed model considers the influence of the decoupling function (used for treating with the inherent coupling effect of the motor), the PWM delay, and the dc-link voltage variation. A full modeling procedure was provided starting from the current control loop, then to the speed control loop. This model provided the base for the following chapters.

In Chapter 4, the state-of-the-art active damping control was comprehensively investigated with reference to the Cur_inj, Vol_inj and VPI technologies. All of the impedance models of the slim dc-link drive were developed for the cases with and without using active damping control. The impedance-based method was addressed to study the drive system instability and input current harmonics. The effects of the different grid impedance as well as the current controller bandwidth were assessed based on the developed impedance model. In addition, the sensitivity analyses were done on the stator voltage, the electrical torque and the rotor speed. The obtained results show that by using active damping control, the instability issue can be solved, the input current harmonic performance can be improved, but still, its PWHD performance cannot pass the standard requirement, and the motor current harmonics

performance becomes a little bit worse. Finally, the lab experiment results were shown to verify the effectiveness of the theoretical analysis.

In Chapter 5, a mathematical model was proposed for the sensorless controlled slim dc-link motor drive system, where the sensorless control strategy was based on the active-flux concept. Similarly, all of the impedance models of the sensorless controlled slim dc-link drive were developed for the cases with and without using active damping control. In this model, the effects of the stator flux observer, the PLL together with the dc-link voltage were considered. According to the developed model, the frequency response of both the current loop and speed loop was discussed individually. Moreover, the instability issue, the input current harmonic issue, as well as the sensitivity of the electrical torque and speed were investigated thereafter. In the end of the chapter, the experimental tests were carried out to verify the theoretical analysis.

In Chapter 6, an active circuit scheme was proposed to solve both the instability and input current harmonic issues simultaneously, as well as the motor current harmonic performance can be improved. The principle of the proposed scheme was discussed. Then, simulations were carried out to verify the effectiveness of the proposed scheme. According to the simulation results, a superior performance can be achieved by using the proposed scheme, compared with using the active damping control. The slim dc-link drive system can be stabilized, and the input current harmonics performance can pass the standard requirement including the PWHD requirement. Besides, the results also show that the dc-link voltage variation becomes much smaller, and a better motor current harmonics performance is achieved.

7.2. Contributions

The main contributions of this research thesis are as below:

- By using Transfer Function Matrix (TFM) principle, a comprehensive generalized mathematic model was developed of the current loop for the both the PMSM and SynRM drive system. Moreover, the developed model was extended to the speed loop.
- The impedance models were developed for the slim dc-link drive system, which considered the effects of the speed loop, the current loop, the PWM delay as well as the dc-link voltage. Based on the developed model, both the instability and harmonic issues were fully investigated.
- A mathematic model was proposed for the sensorless controlled motor drive system, where the sensorless control strategy was based on the active-flux concept.
- Impedance models were developed for the sensorless controlled slim dc-link drive system as well with the consideration of the effects of the speed loop, the current loop, and the dc-link voltage.

- An active circuit scheme was proposed to completely solve the issues regarding the instability, the input current harmonic as well as the torque and speed sensitivity for the slim dc-link drive system.

7.3. Future Work

Further research may be of interesting in some of the following areas:

- A general fully digitalized model of current loop based on the TFM principle can be developed to guide the digital current controller design.
- Based on the developed sensorless model, a comprehensive theoretical analysis can be done on the system performance by comparing with the sensored model.
- The experimental tests of the proposed active circuit scheme can be done to further verify its effectiveness of theoretical analysis.
- The impact on the field weakening performance can be investigated by using active damping, then a feasible field weakening scheme may be founded.
- The system EMI performance can be estimated when using the proposed active circuit scheme.
- The study could be done to improve the input harmonic performance for a multi slim dc-link drives system when feeding by a soft grid.

Bibliography

[1] Marketsandmarkets.com, [online], "AC drive market by voltage, power rating, application, end-use industry and region – globe trends & forecast to 2021," Nov. 2016. http://www.marketsandmarkets.com/Market-Reports/ac-drives-market-131149781.html.

[2] M. Sakui, H. Fujita, "An Analytical Method for Calculating Harmonic Currents of a Three-Phase Diode-Bridge Rectifier with dc Filter", IEEE Trans. on Power Electro., Vol. 9, No. 6, pp. 631-637, Nov. 1994.

[3] G. W. Chang, S.-K. Chen, H.-J. Su, and P.-K. Wang, "Accurate assessment of harmonic and interharmonic currents generated by VSI-fed adjustable speed drives," IEEE Trans. Power Delivery, vol. 20, no. 4, pp. 2585–2593, Oct. 2005.

[4] P. Davari, Y. Yang, F. Zare, F. Blaabjerg, "A review of electronic inductor technique for power factor correction in three-phase adjustable speed drives," in Proc. IEEE ECCE-2016, pp. 1-8, Sep. 2016.

[5] P. Pejovic, "Three-phase diode rectifiers with low harmonics," Springer, 2007.

[6] J. W. Kolar, and T. Friedli, "The essence of three phase PFC rectifier systems: part I," IEEE Trans. Power Electron., vol. 28, no. 1, pp. 176–198, Jan. 2013.

[7] Y. Feng, U. Jaeger, P. Wang, H. Huang, "A Choke and EMI Filter", CN patent, 103578691 , Aug. 2016.

[8] M. Zuccherato, F. Zare, "Analysis and modeling of a permanent magnets biased inductor used in motor drive system," in Proc. EPE-2015 ECCE-Euro, pp. 1-7, Sep. 2015.

[9] C. Klumpner, F. Blaabjerg, and P. Thoegersen, "Alternate ASDs, evaluation of the converter topologies suited for integrated motor drives," IEEE Trans. Ind. App. Magazine, pp. 71-83, Mar./Apr. 2006.

[10] K. Sangshin and H. A. Toliyat, "Design and rating comparisons of PWM voltage source rectifiers and active power filters for AC drives with unity power factor," IEEE Trans. Power Electron., vol. 20, no. 5, pp. 1133–1142, Sep. 2005.

[11] M. Liserre, R. Teodorescu, and F. Blaabjerg, "Multiple harmonics control for three-phase grid converter systems with the use of PI-RES cur-rent controller in a rotating frame," IEEE Trans. Power Electron., vol. 21, no. 3, pp. 836–841, May 2006.

[12] X. H. Wu, S. K. Panda, and J. X. Xu, "Design of a plug-in repetitive control scheme for eliminating supply-side current harmonics of three phase PWM Boost rectifier under generalized supply voltage conditions," IEEE Trans. Power Electron., vol. 25, no. 7, pp. 1800–1810, Jul. 2010.

[13] S. Hiti, V. Vlatkovic, D. Borojevic, and F. Lee, "A new control algorithm for three-phase PWM buck rectifier with input displacement factor compensation," IEEE Trans. Power Electron., vol. 9, no. 2, pp. 173–180, Mar. 1994.

[14] A. Stupar, T. Friedli, J. Miniboeck, T. Friedli, and J. W. Kolar, "Towards a 99% efficient three-phase buck-type PFC rectifier for 400 V dc distribution systems," IEEE Trans. Power Electron., vol. 27, no. 4, pp. 1732–1744, Apr. 2012.

[15] T. Nussbaumer and J. W. Kolar, "Improving mains current quality for three-phase three-switch buck-type PWM rectifiers," IEEE Trans. Power Electron., vol. 21, no. 4, pp. 967–973, Jul. 2006.

[16] T. C. Green, M. H. Taha, N. A. Rahim, and B. W. Williams, "Three-phase step-down reversible ac-dc power converter," IEEE Trans. Power Electron., vol. 12, no. 2, pp. 319–324, Mar. 1997.

[17] H. Mao, F.C. Lee, D. Borojevie, and S. Hiti, "Review of HighPerformance Three-Phase Power-Factor Correction Circuits," IEEE Trans. Ind. Electron., vol. 44, pp. 437–446, Aug. 1997.

[18] M. Malinowski, M. Jasinski, and M. P. Kazmierkowski, "Simple direct power control of three-phase PWM rectifier using space vector modulation (DPC-SVM)," IEEE Trans. Ind. Electron., vol. 51, no. 2, pp. 447–454, Apr. 2004.

[19] Y. Jiang, H. Mao, F. C. Lee, and D. Borojevic, "Simple high performance three-phase boost rectifiers," in Proc. IEEE PESC-1994, pp. 1158–1163, 1994.

[20] V. Vlatkovic, D. Borojevic, F. C. Lee, C. Cuadros, and S. Gataric, "A new zero-voltage-transition, three-phase PWM rectifier/inverter circuit," in Proc. PESC-1993, pp. 868–873, 1993.

[21] S. Mao, T. Wu, X. Lu, J. Popovic, J . A. Ferreira, "Three-phase active front-end rectifier efficiency improvement with silicon carbide power semiconductor devices," in Proc. IEEE ECCE-2016, pp. 1-8, Sep. 2016.

[22] L. Malesani, L. Rossetto, P. Tenti, and P. Tomasin, "AC/DC/AC PWM converter with reduced energy storage in the DC link," IEEE Trans. Ind. App., vol. 31, no. 2, pp. 287–292, Mar./Apr. 1995.

[23] B. Gu, and K. Nam, "A DC link capacitor minimization method through direct capacitor current control," IEEE Trans. Ind. Appl., vol. 42, no. 2, pp. 573–581, Mar. 2006.

[24] A. Mallik, W. Ding, and A. Khaligh, "A comprehensive design approach to an EMI filter for a 6-kW three-phase Boost power factor correction rectifier in avionics vehicular systems," IEEE Trans. Vehic. Tech., vol. 66, no. 4, pp. 2942–2951, Apr. 2017.

[25] N. Mohan, "A novel approach to minimize line current harmonics in interfacing renewable energy source with 3-phase utility systems," in Proc. IEEE APEC-1992, pp. 852–858, Mar. 1992.

[26] S. Kim, P. N. Enjeti, P. Packbush, and I. J. Pitel, "A new approach to improve power factor and reduce harmonics in a three-phase diode rectifier type utility interface," IEEE Trans. Ind. App., vol. 30, no. 6, pp. 1557–1564, Nov./Dec. 1994.

[27] R. Naik, M. Rastogi, and N. Mohan, "Third-harmonic modulated power electronics interface with three-phase utility to provide a regulated dc output and to minimize line-current harmonics," IEEE Trans. Ind. App., vol. 31, no. 3, pp. 598–601, May/June 1995.

[28] S. Hansen, P. N. Enjeti, J.-H. Hahn, and F. Blaabjerg, "An integrated single-switch approach to improve harmonic performance of standard PWM adjustable-speed drives," IEEE Trans. Ind. App., vol. 36, no. 4, pp. 1189–1196, Jul./Aug. 2000.

[29] J. C. Salmon, "Operating a three-phase diode rectifier with a low-input current distortion using a series-connected dual boost converter," IEEE Trans. Power Electron., vol. 11, no. 4, pp. 592–603, Jul. 1996.

[30] J. W. Kolar, H. Ertl, and F. C. Zach, "Space vector-based analytical analysis of the input current distortion of a three-phase discontinuous-mode boost rectifier system," in Proc. IEEE PESC-1993, pp. 696–703, Jun. 1993.

[31] M. Hartmann, T. Friedli, and J. W. Kolar, "Swiss rectifier – A novel three-phase buck-type PFC topology for Electric Vehicle battery charging," in Proc. IEEE APEC-2012, pp. 2617-2624, Feb. 2012.

[32] H. Yoo and S.-K. Sul, "A new circuit design and control to reduce input harmonic current for a three-phase ac machine drive system having a very small dc-link capacitor," in Proc. IEEE APEC-2010, pp. 611–618, Feb. 2010.

[33] M. L. Heldwein and J. W. Kolar, "Impact of EMC filters on the power density of modern three-phase PWM converters," IEEE Trans. Power Electron., vol. 24, no. 6, pp. 1577–1588, Jun. 2009.

[34] J. W. Kolar, H. Ertl, and F. C. Zach, "Realization considerations for unidirectional three-phase PWM rectifier systems with low effects on the mains," in Proc. 6th Conf. Power Electronics and Motion Control (PEMC), vol. 2, pp. 560–565, Oct. 1990.

[35] P. Davari, Y. Yang, F. Zare, and F. Blaabjerg, "A multi-pulse pattern modulation scheme for harmonic mitigation in three-phase multi-drives," IEEE Journal. Emerging and Select. Topics in Power Electron, vol. 4, no. 1, pp. 174-185, 2016.

[36] Y. Yang, P. Davari, F. Zare, and F. Blaabjerg, "A dc-link modulation scheme with phase-shifted current control for harmonic cancellation in multi-drive applications," IEEE Trans. Power Electron., vol. 31, no. 3, pp. 1837-1840, Mar. 2016.

[37] H. Ertl, J. W. Kolar, and F. C. Zach, "A constant output current three-phase diode bridge employing a novel "electronic smoothing inductor"," in Proc. 39th Int. Power Conversion Conf. (PCIM), Nuremberg, Germany, Jun. 22–24, 1999, pp. 645–651.

[38] J. C. Das, "Passive filters – potentialities and limitations," IEEE Trans. on Ind. Appl., vol. 40, no. 31, pp. 232–241, Jan./Feb. 2004.

[39] H. Akagi, "Active harmonic filters," in Proc. of IEEE, Vol. 93, no. 12, pp. 2128–2141, Dec. 2005.

[40] S. Yang, A. Bryant, P. Mawby, D. Xiang, R. Li, and P. Tavner, "An Industry-Based Survey of Reliability in Power Electronic Converters," IEEE Trans. on Ind. Appl., vol. 47, no. 3, pp. 1441-1451, 2011.

[41] F. Souza, P.Pereira, H. d. Paula, B. Filho, and A. V. Rocha, "Motor drive systems reliability: impact of the environment conditions on the electronic component failure rates," in Proc. IEEE IAS-2014, pp.1-8, 2014.

[42] T. Fujihira, M. Otsuki, O. Ikawa, A. Nishiura, N. Fujishima, "The state-of-the-art and future trend of power semiconductor divices," in Proc. IEEE PCIM-2015, pp. 27-34, May, 2015.

[43] X. She, A. Q. Huang, O. Lucia, B. Ozpineci, "Review of silicon carbide power devices and their applications," IEEE Trans. on Ind. Electro., vol. 64, Iss. 10, pp. 8193-8205, 2017.

[44] P. Ning, Z. Liang, and F. Wang, "Double-sided cooling design for novel planar module," in Proc. IEEE APEC-2013, pp. 616–621. Mar. 2013.

[45] R. Bayerer, "Advanced packaging yields higher performance and reliability in power electronics," Microelectron. Rel., vol. 50, no. 9-11, pp. 1715–1719, Sep.-Nov., 2010.

[46] P. Paret, D. DeVoto, and S. Narumanchi, "Reliability of emerging bonded interface materials for large-area attachments," IEEE Trans. on Component, Packaging, and Manufacturing Tech., vol. 6, no. 1, pp. 40-49, Jan., 2016.

[47] Takahashi, I., Itoh, Y. "Electrolytic capacitor-less PWM inverter", in Proc. of Inter. Power Electro. Conf. (IPEC), pp. 131-138, Tokyo, 1990.

[48] H. Wang and F. Blaabjerg, "Reliability of capacitors for dc-link applications in power electronic converters - an overview," IEEE Trans. Ind. Appl., vol. 50, no. 5, pp. 3569–3578, Sep. 2014.

[49] L. L. Maccomber, "Aluminum electrolytic capacitors in power electronics," in Proc. IEEE APEC-2011, pp. 1–14, Mar. 2011.

[50] I. Takahashi, R. Itoh, "Electrolytic capacitor-less PWM inverter", in proc. of International Power Electronics Conference, pp. 131-138, Tokyo, 1990.

[51] W.-J. Lee and S.-K. Sul, "DC-link voltage stabilization for reduced dc-link capacitor inverter," IEEE Trans. Ind. Appl., vol. 50, no. 1, pp. 404–414, Jan. 2014.

[52] Low harmonic techonology, reducing harmonic currents for SED2. https://www.siemens.be/cmc/upload/cms/docs/sbt/hvac/Brochures_Datasheets_manuals/NL/14_Aandrijvingen_Variabele_Snelheid/Brochures/brochure_Low%20Harmonic%20Technology_EN.pdf.

[53] Vacon 100 flow, http://vacon-100-flow.vacon.com/.

[54] M. Salcone, J. Bond, "Selecting film bus link capacitors for high performance inverter applications," in Proc. IEEE Electric Machines and Drives Conference (IEMDC), pp. 1692–1699, Jun. 2009.

[55] S. Parler, L. L. Maccomber, "DC-link capacitors for inverter applications," in Proc. IEEE APEC-2013 (Industrial session 1.3), pp. 1–6, Mar. 2013.

[56] R. Maheshwari, "The use of active elements to reduce the size and weight of passive components in adjustable speed drives," PhD thesis, Aalborg University, Denmark, 2017.

[57] H. Saren, O. Pyrhonen, K. Rauma, O. Laakkonen, "Overmodulation in voltage source inverter with small dc-link capacitor," in Proc. PESC-2005, pp. 892-898, Jun. 2005.

[58] X. Chen, and M. Kazerani, "Space vector modulation control of an ac-dc-ac converter with a frond-end diode rectifier and reduced dc-link capacitor," IEEE trans. Power Electron., vol. 21, no. 5, pp. 1470-1478, Sep., 2006.

[59] H. R. Andersen, R. Tan, and K. Cai, "3-phase ac-drives with passive front-ends with focus on the slim dc-link topology," in Proc. IEEE PESC-2008, pp. 3248-3254, Jun. 2008.

[60] R. Maheshwari, S. Munk-Nielsen, "Performance analysis of active damped small DC-link capacitor based drive for unbalanced input voltage supply," in Proc. IEEE EPE-2011, pp.1-10, Sep. 2011.

[61] J. Itoh, W. Aoki, G. T. Chiang, A. Toba, "Suppression method of rising DC voltage for the halt sequence of an inverter in the motor regeneration," in Proc. IEEE ECCE-2013, pp. 188-195, Oct. 2013.

[62] A. Yoo, S.-K. Sul, H. Kim, and K.-S. Kim, "Flux-weakening strategy of an induction machine driven by an electrolytic-capacitor-less inverter," IEEE Trans. Ind. Appl., vol. 47, no. 3, pp. 1328-1336, May/Jun. 2011.

[63] S. D. Sudhoff, K. A. Corzine, S. F. Glover, H. J. Hegner, and H. N. Robey, Jr., "DC link stabilized field oriented control of electric propulsion systems," IEEE Trans. Energy Convers., vol. 13, no. 1, pp. 27-33, Mar., 1998.

[64] A. Emadi, A. Khaligh, C. H. Rivetta, and G. A. Williamson, "Constant power loads and negative impedance instability in automotive systems: Definition, modeling, stability, and control of power electronic converters and motor drives," IEEE Trans. Veh. Technol., vol. 55, no. 4, pp. 1112–1125, Jul. 2006.

[65] X. Feng, J. Liu, and F. C. Lee, "Impedance specifications for stable DC distributed power systems," IEEE Trans. Power Electron., vol. 17, no. 2, pp. 157-162, Mar. 2002.

[66] R. D. Middlebrook, "Input flter considerations in design and application of switching regulators," in Proc. of IEEE IAS-1976, pp. 366-382.

[67] B. Mellitt, and J. Allan, "Stability characteristics of a constant power chopper controller for traction drives," IEE Jour. on Electric Power Appl., vol.1, issue 3, pp. 100-104, Aug. 1978.

[68] Y. Feng, D. Wang, F. Blaabjerg, X. Wang, P. Davari, K. Lu, "Active Damping Control for Three-Phase Slim DC-link Drive System – overview and investigation," in Proc. IEEE IFEEC-ECCE Asia, 2017, pp. 1-6, Jun. 2017.

[69] R. W. Erickson, "Optimal single resistor damping of input filters," in Proc. of 14th IEEE Appl. Power Electron. Conf., 1999, pp. 1073–1079.

[70] M. Cespedes, T. Beechner, L. Xing, and J. Sun, "Stabilization of constant-power loads by passive impedance damping," IEEE Trans. on Power Electro., Vol. 26, No. 7, pp. 1832–1836, Aug 2011.

[71] M. Janecke, "Control method for inverter with induction machine - varing torque generating demand value with ripple on dc intermediate circuit voltage," EU patent DE 4110225 A1, Oct. 1992.

[72] A. M. Walczyna, K. Hasse, and R. Czarnecki, "Input filter stability of drives fed from voltage inverters controlled by direct flux and torque control methods," IEE proc. Electro. Power Appl., vol. 143, no. 5, pp. 396–402, Sep. 1996.

[73] K. Pietiläinen, L. Harnefors, A. Petersson, and H.-P. Nee, "DC-link stabilization and voltage sag ride-through of inverter drives," IEEE Trans. Ind. Electron., vol. 53, no. 4, pp. 1261–1268, Jun. 2006.

[74] H. Mosskull, J. Galic, and B. Wahlberg, "Stabilization of induction motor drives with poorly damped input filters," IEEE Trans. Ind. Electron., vol. 54, no. 5, pp. 2724–2734, Oct. 2007.

[75] M. Hinkkanen, and J. Luomi, "Induction motor drives equipped with diode rectifier and small dc-link capacitance," IEEE Trans. Ind. Electron., vol. 55, no. 1, pp. 312–320, Jan. 2008.

[76] P. Magne, D. Marx, B. Nahid-Mobarakeh, and S. Pierfederici, "Large-signal stabilization of a dc-link supplying a constant power load using a

virtual capacitor: Impact on the domain of attraction," IEEE Trans. Ind. Appl., vol. 48, no. 3, pp. 878–887, May/Jun. 2012.

[77] B. H. Bae, B. H. Cho, and S. K. Sul, "Damping control strategy for the vector controlled traction drive," in Proc. 9th Eur. Conf. Power Electron. and Appl., pp. 1-9, Graz, Austria, 2001.

[78] X. Liu, A. J. Forsyth, and A. M. Cross, "Negative input-resistance compensator for a constant power load," IEEE Trans. Ind. Electron., vol. 54, no. 6, pp. 3188–3196, Dec. 2007.

[79] X. Liu, and A. J. Forsyth, "Active stabilization of a PMSM drive system for aerospace applications," Proc. IEEE PESC-2008, pp. 283–289, Jun. 2008.

[80] B. Delemontey, B Jacquot, C Iung, B De Fornel, J Bavard, "Stability analysis and stabilization of an induction motor drive with input filter," Proc. 6th Euro. Conference on Power Electro. and Appl. (EPE-1995), pp: 121-126, 1995.

[81] H. Mosskull, "Robust control of an induction motor drive," Ph.D. dissertation, Royal Inst. Technol., Stockholm, Sweden, 2006.

[82] M. Hinkkanen, L. Harnefors, and J. Luomi, "Control of induction motor drives equipped with small dc-link capacitance," in Proc. EPE-2007, pp. 1–10.

[83] Y. A.-R. I. Mohamed, A. A. A. Radwan, and T. K. Lee, "Decoupled reference-voltage-based active dc-link stabilization for PMSM drives with tight-speed regulation," IEEE Trans. Ind. Electron., vol. 59, no. 12, pp.4523–4536, Dec. 2012.

[84] R. Maheshwari, S. Munk-Nielsen, and K. Lu, "An active damping technique for small dc-link capacitor based drive system," IEEE Trans. on Industrial Informatics, vol. 9, no. 2, pp. 848-858, May 2013.

[85] L. Mathe, H. R. Anderson, R. Lazar, and M. Ciobotaru, "DC-link compensation method for slim dc-link drives fed by soft grid," in Proc. IEEE International Symposium on Industrial Electronics (ISIE), 2010, pp. 1236–1241, Jun. 2010.

[86] D. Wang, K. Lu, P. O. Rasmussen, L. Mathe, Y. Feng, "Voltage modulation using virtual positive impedance concept for active damping of small dc-link drive system," in Proc. IEEE ECCE-2015, pp. 20-24, Oct. 2015.

[87] L. Math, L. Torok, D. Wang, D. Sera, "Resonance reduction for ac drives with small capacitor in the dc-link," in Proc. IEEE Environ. and Electri. Eng. (EEEIC), 2016, pp.1-6, Sep. 2016.

[88] H. Shin, H. G. Choi and J.I. Ha, "DC-link shunt compensator for three phase system with small dc-link capacitor," in Proc. of IEEE ECCE Asia-2015, pp.33–39, 2015.

[89] J. Y. Lee, and Y.Y. Sun, "Adaptive harmonic control in PWM inverters with fluctuating input voltage," IEEE Trans. on Ind. Electron., vol. 33, no. 1, pp. 92–98, Feb. 1986.

[90] P. Enjeti, W. Shireen, "A new technique to reject dc-link voltage ripple for inverters operating programmed PWM waveforms," IEEE Trans. on Power Electro., vol. 7, no. 1, pp. 171–180, Jan. 1992.

[91] J. K. Pedersen, F. Blaabjerg, J. W. Jensen, and P. Thogersen, "An ideal PWM-VSI inverter with feedforward and feedback compensation," in Proc. Power Electronics and Applications, (EPE-1993), vol.5, pp. 501-507, 1993.

[92] Y. Feng, J. B. Kwon, X. Wang, and F. Blaabjerg, "Input harmonic analysis of slim dc-link drive using harmonic state space," in Proc. IEEE IFEEC-ECCE Asia 2017, pp. 1-6, Jun. 2017.

[93] H. Soltani, P. Davari, D. Kumar, F. Zare, and F. Blaabjerg, "Effects of dc-link filter on harmonic and interharmonic generation in three-phase adjustable speed drive system," in Proc. of IEEE ECCE-2017, pp.1-7, Oct. 2017.

[94] F. Zare, H. Soltani, D. Kumar, P. Davari, H. A. M. Delpino, and F. Blaaberg, "Harmonic emissions of three-phase diode rectifiers in distribution networks," IEEE Access, vol. 5, pp. 2819-2833, Feb. 2017.

[95] Y. Feng, L. Mathe, K. Lu, F. Blaabjerg, X. Wang, K. Lu, and P. Davari, "Analysis of harmonics Suppression by Active Damping Control on Multi Slim DC-link Drives," in Proc. IEEE IECON-2016, pp. 5001-5006, Nov. 2016.

[96] H.M. Delpino, Dinesh Kumar, "Line harmonics on system using reduced dc-link capacitor," in Proc. of IEEE IECON 2013, Vienna, Austria, pp. 961-966, 2013.

[97] D. Kumar, F. Zare, "Harmonic analysis of grid connected power electronic systems in low power distribution networks," IEEE Journal of

Emerging and Selected Topics in Power Electronics, vol.4, no.1, pp. 70-79, Mar. 2016.

[98] M. Grötzbach and R. Redmann, "Line current harmonics of VSI-fed adjustable-speed drives," IEEE Trans. Ind. Applicat., Vol. 36, pp. 683–690, Mar./Apr. 2000.

[99] W. Xu, H. W. Dommel, M. B. Hughes, G. W. Chang, and L. Tan, "Modeling of adjustable speed drives for power system harmonic anal- ysis," IEEE Trans. Power Syst., vol. 14, no. 2, pp. 595–601, Apr. 1999.

[100] G. Carpinelli, F. Iacovone, A. Russo, P. Varilone and P. Verde, "Analytical modelling for harmonic analysis of line current of VSI-fed drives," IEEE Trans. on Power Del., Vol. 19, No. 3, pp. 1212–1224, Jul., 2004.

[101] T. Yang, S. V. Bozhko, G. M. Asher, "Modeling of uncontrolled rectifiers using dynamic phasors," in Proc. of Electrical Systems for Aircraft, Railway and Ship Propulsion (ESARS), pp. 1-6, 2012.

[102] S. R. Sanders, J. M. Noworolski, X. Z. Liu, and G. C. Verghese, "Generalized averaging method for power conversion circuits," IEEE Trans. Power Electron., vol. 6, no. 2, pp. 251-259, Apr. 1991.

[103] N. M. Wereley and S. R. Hall, "Linear Time Periodic Systems: Transfer Function, Poles, Transmission Zeroes and Directional Properties," Am. Control Conf., pp. 1179–1184, Jun. 1991.

[104] J. Kwon; X. Wang; C.L., Bak,; F. Blaabjerg, "The modeling and harmonic coupling analysis of multiple-parallel connected inverter using Harmonic State Space (HSS)", in Proc. of ECCE-2015, pp. 6231- 6238, Sep. 2015.

[105] M.S. Hwang and A.R. Wood, "Harmonic State-Space Modelling of an HVdc Converter," in the Proc. of 15th IEEE Harmonics and Quality of Power, pp. 573-580, June 2012.

[106] E. Mollerstedt, B. Bemhardsson, "A harmonic transfer function model for a diode converter train," in Proc. of IEEE Power Engin. Society Winter Meeting, Vol. 2, pp. 957-962, Jan. 2000.

[107] Y. Feng, J. B. Kwon, X. Wang, and F. Blaabjerg, "Harmonic coupling analysis of multi-drive system with slim dc-link drive," in Proc. IEEE Ind. Symposium on Ind. Electro. (ISIE), 2017, pp. 1-6, Jun. 2017.

[108] Y. Feng, D. Wang, F. Blaabjerg, X. Wang, K. Lu, and P. Davari, "Active damping control for three-phase slim dc-link drive system, — overview and investigation," in Proc. IEEE IFEEC-ECCE Asia 2017, pp. 1-6, Jun. 2017.

[109] Y. V. Singh, P. O. Rasmussen, T. O. Anderson, "Performance improvement of three phase rectifier by employing electronic smoothing inductor," in Proc. IEEE IECON-2014, pp. 1713-1719, Oct. 2014.

[110] Y. V. Singh, "Motor integrated variable speed drives," Ph.D. thesis, Aalborg University, Aalborg, Denmark, 2016.

[111] S. Hiti, D. Boroyevich, C. Cuadros, "Small-signal modelling and control of three-phase PWM converters," in Proc. of IEEE IAS-1994, pp. 1143-1150.

[112] D. M. Van de Sype, K. D. Gusseme, A. P. V. Bossche, and J. A. Melkebeek, "Small-signal Laplace-domain analysis of uniformly-sampled pulse-width modulators," in Proc. of IEEE PESC 2004, pp. 4292-4298.

[113] B. H. Bae and S. K. Sul, "A compensation method for time delay of full-digital synchronous frame current regulator of PWM AC drives," IEEE Trans. Ind. Appl., vol. 39, no. 3, pp. 802–810, May/Jun. 2003.

[114] H. Mosskull, J. Galic and B. Wahlberg, "Stabilization of an induction motor drive with resonant input filter," in Proc. of IEEE EPE-2005, pp.1-10.

[115] F. Briz del Blanco, M. W. Degner, and R. D. Lorenz, "Dynamic analysis of current regulators for ac motors using complex vectors," IEEE Trans. Ind. Appl., vol. 35, no. 6, pp. 1424–1432, Nov./Dec. 1999.

[116] D. W. Novotny, T. A. Lipo, "Vector control and dynamics of ac drives," Clarendon Press, Oxford, 1996.

[117] Y. S. Jeong and S. K. Sul, "Analysis and design of a decoupling current controller for AC machines," in Conf. Rec. IEEE IAS Annu. Meeting, Hong Kong, 2005, pp. 751–758.

[118] L. Harnefors, "Modeling of three-phase dynamic systems using complex transfer functions and transfer matrices," IEEE Trans. Ind. Electron., vol. 54, no. 4, pp. 2239–2248, Aug. 2007.

[119] R. Krishnan, "Permanent magnet synchronous and brushless DC motor drives," CRC Press, 2010.

[120] P. C. Krause, O. Wasynczuk, and S. D. Sudhoff, Analysis of Electric Machinery and Drive Systems, Piscataway, NJ: IEEE Press, 2002.

[121] J. Holtz, Q. Juntao, J. Pontt, J. Rodriguez, P. Newman, and H. Miranda, "Design of fast and robust current regulators for high-power drives based on complex state variables," IEEE Trans. Ind. Appl., vol. 40, no. 5, pp. 1388–1397, Sep./Oct. 2004.

[122] J. Holtz, "The representation of AC machine dynamics by complex signal flow graphs," IEEE Trans. Ind. Electron., vol. 42, pp. 263–271, June 1995.

[123] F. Briz, M. W. Degner, and R. D. Lorenz, "Analysis and design of current regulators using complex vectors," IEEE Trans. Ind. Appl., vol. 36, no. 3, pp. 817–825, May/Jun. 2000.

[124] H. Kim and R. D. Lorenz, "Synchronous frame PI current regulators in a virtually translated system," in Conf. Rec. 2004 IEEE IAS, pp. 856–863.

[125] M. Hinkkanen, H. A. A. Awan, Z. Qu, T. Tuovinen, and F. Briz, "Current control for synchronous motor drives: direct discrete-time pole-placement design," IEEE Trans. Ind. Appl., vol. 52, no. 2, pp. 1530–1541, Aug. 2016.

[126] L. Harnefors and H. P. Nee, "Model-based current control of AC machines using the internal model control method," IEEE Trans. Ind. Appl., vol. 34, no. 1, pp. 133–141, Jan./Feb. 1998.

[127] J.-W. Choi and S.-K. Sul, "New control concept-minimum time current control in the three-phase PWM converter," IEEE Trans. Power Electron., vol 21, pp. 124–131, Jan. 1997.

[128] C.-M. Liaw, "Design of a two-degree-of-freedom controller for motor drives," IEEE Trans. Autom. Control, vol. 37, no. 8, pp. 1215–1220, Aug. 1992.

[129] J.-S. Yim, S.-K. Sul, B.-H. Bae, N. R. Patel, and S. Hiti, "Modified current control schemes for high-performance permanent-magnet ac drives with low sampling to operating frequency ratio," IEEE Trans. Ind. Appl., vol. 45, no. 2, pp. 763–771, Mar./Apr. 2009.

[130] L. Harnefors, "Design and analysis of general rotor-flux-oriented vector control systems," IEEE Trans. Ind. Electron., vol. 48, no. 2, pp. 383–390, Apr. 2001.

[131] L. Harnefors, S. E. Saarakkala, M. Hinkkanen, "Speed control of electrical drives using classical control methods," IEEE Trans. Ind. Appl., vol. 49, no. 2, pp. 889–898, Mar./Apr. 2013.

[132] K. Lu, "Modern machines and drive system," PhD course, Energy Technology Department, Aalborg University, Denmark, 2014.

[133] W.-J Lee, S.-K. Sul, "DC-Link Voltage Stabilization for Reduced DC-Link Capacitor Inverter", IEEE Trans. Ind. App., vol.50, no. 1, pp. 404-414, Jan./Feb. 2014.

[134] M. Belkhayat, "Stability criteria for ac power system with regulated loads," PhD thesis, Purdue University, USA, 1997.

[135] R. D. Middlebrook, "Input filter considerations in design and application of switching regulators," in Proc. of IEEE IAS-1976, pp. 366-382.

[136] C. M. Wildrick, F. C. Lee, B. H. Cho, and B. Choi, "A method of de fining the load impedance specification for a stable distributed power system," IEEE Trans. Power Electron., vol. 10, no. 3, pp. 280-285, May 1995.

[137] S. D. Sudhoff, S. F. Glover, P. T. Lamm, D. H. Schmucker, and D. E. Delisle, "Admittance space stability analysis of power electronic systems," IEEE Trans. Aerosp. Electron., vol. 36, no. 3, pp. 965–973, Jul. 2000.

[138] X. Feng, Z. Ye, K. Xing, F. C. Lee, and D. Borojevic, "Individual load impedance specification for a stable dc distributed power system," in Proc. of IEEE APEC-1999, vol. 2, pp. 923–929.

[139] J. Sun, "Impedance-based stability criterion for grid-connected inverters," IEEE Trans. Power Electron. vol. 26, no.11, pp. 3075-3078, Nov., 2011.

[140] S. Vesti, T. Suntio, J. A. Oliver R. Prieto, and J. A. Cobos, "Impedance-based stability and transient-performance assessment applying maximum peak criteria," IEEE Trans. Power Electron. vol. 28, no.5, pp. 2099-2104, May, 2013.

[141] E. D. Fasse, "Stability robustness of impedance controlled manipulators coupled to passive environments," Master's thesis, MIT, June, 1987.

[142] A. Riccobono, and E. Santi, "A novel passivity-based stability criterion (PBSC) for switching converter DC distribution systems," in Proc. of IEEE APEC-2012, pp. 2560-2567.

[143] J. Wang, A. Griffo, L. Han, and D. Howe, "Input admittance characteristics of permanent magnet brushless AC motor drive systems," in Proc. of IEEE VPPC-2007, pp. 191–196.

[144] O. Wallmark, S. Lundberg, and M. Bongiorno, "Input admittance expressions for field-oriented controlled salient PMSM drives," IEEE Trans. Power Electron., vol. 27, no. 3, pp. 1514–1520, Mar. 2012.

[145] Y. Feng, M. Laszlo, K. Lu, F. Blaabjerg, X. Wang, and P. Davari, "Analysis of Harmonics Suppression by Active Damping Control on Multi Slim DC-link Drives," in Proc. of IEEE IECON-2016, pp. 5001-5006.

[146] Y. Feng, J. B. Kwon, F. Blaabjerg, X. Wang, "Input Harmonic Analysis on the Slim DC-Link Drive Using Harmonic State Space Model," in Proc. of IFEEC – ECCE Asia 2017, pp. 1-6.

[147] J. R. Frus and B. C. Kuo, "Closed-loop control of step motors using waveform detection feedback," in Proc. Intern. Conf. Stepping Motors and Systems, pp. 77-84, Leeds, UK, 1976.

[148] R. Bojoi, M. Pastorelli, J. Bottomley, P. Giangrande, and C. Gerada, "Sensorless control of PM motor drives - a technology status review," in IEEE Workshop on Electrical Machines Design Control and Diagnosis (WEMDCD), 2013, pp. 168-182, Mar. 2013.

[149] Jansen, P.L.; Lorenz, R.D. "Transducerless position and velocity estimation in induction and salient AC machines," IEEE Trans. Ind. Appl., vol.31, no.2, pp.240-247, Mar/Apr. 1995.

[150] J.I. Ha, K. Ide, T. Sawa, S.K. Sul "Sensorless rotor position estimation of an interior permanent magnet motor from initial states," IEEE Trans. Ind. App., vol.39, no.3, pp. 761-767, May/Jun. 2003.

[151] W. Hammel and R. M. Kennel, "Position sensorless control of PMSM by synchronous injection and demodulation of alternating carrier voltage," in Proc. 1st Symp. SLED, pp. 56–63, Jul. 2010.

[152] L.M. Gong and Z.Q. Zhu, "Robust initial rotor position estimation of permanent magnet brushless AC machines with carrier-signal-injection-based sensorless control," IEEE Trans. Ind. Appl., vol. 49, no. 6, pp. 2602-2609, Nov/Dec. 2013.

[153] R. Wu, G. R. Slemon, "A permanent magnet motor drive without a shaft sensor," IEEE Trans. Ind. Applicat., vol. 27, pp. 1005-1011, Sept./Oct. 1991.

[154] Z. Chen, M. Tomita, S. Doki, and S. Okuma, "An extended electromotive force model for sensorless control of interior permanent-magnet synchronous motors," IEEE Trans. Ind. Electron., vol. 50, pp. 288-295, Apr. 2003.

[155] S. Morimoto, K. Kawamoto, M.Sanada, and Y. Takeda, "Sensorless Control Strategy for Salient-Pole PMSM Based on Extended EMF in Rotating Reference Frame," IEEE Tran. Ind. Applicat., vol. 38, no. 4, pp. 1054-1061, July/August 2002.

[156] I. Boldea, M. Paicu, and G. Andreescu, "Active flux concept for motion-sensorless unified AC drives," IEEE Trans. Power Electron., vol. 23, no. 5, pp. 2612-2618, Sept 2008.

[157] Y. Park and S.-K. Sul, "Sensorless control method for PMSM based on frequency-adaptive disturbance observer," IEEE Journal of Emerging and Selected Topics in Power Electron., vol. 2, no. 2, pp. 143-151, Jun. 2014.

[158] Y. Lee, Y. C. Kwon, and S. K. Sul, "Comparison of rotor position estimation performance in fundamental-model-based sensorless control of PMSM," in Proc. of IEEE ECCE-2015, pp. 5624-5633, Sep. 2015.

[159] S. Bolognani, L. Ortombina, F. Tinazzi, M. Zigliotto, "Model sensitivity assessment for sensorless PM and Reluctance Motor drives," in Proc. of IEEE IECON-2016, pp. 2851-2856, Oct. 2016.

[160] L. Harnefors, M. Bongiorno, and S. Lundberg, "Input-admittance calculation and shaping for controlled voltage-source converters," IEEE Trans. Ind. Electron., vol. 54, no. 6, pp. 3323–3334, Dec. 2007.

[161] B. Wen, D. Dong, D. Boroyevich, R. Burgos, P. Mattavelli, Z. Shen, "Impedance-Based Analysis of Grid-Synchronization Stability for Three-Phase Paralleled Converters," IEEE Trans. on Power Electron., vol.31, no.1, pp. 26-38, Apr. 2016.

[162] https://en.wikipedia.org/wiki/Atan2.

[163] X. Du, L. Zhou, H. Lu, and Tai H.-M., "DC link active power filter for three-phase diode rectifier," IEEE Trans. Ind. Electron., vol. 59, no. 3, pp. 1430–1442, Mar. 2012.

[164] P. Davari, Y. Yang, F. Zare, and F. Blaabjerg, "A multi-pulse pattern modulation scheme for harmonic mitigation in three-phase multi-motor drives," IEEE J. Emerg. Selec. Top. Power Electron., vol. 4, no. 1, pp. 174-185, Mar. 2016.

[165] H. Wang, H. S.-H. Chuang, and W. Liu, "Use of a series voltage compensator for reduction of the dc-link capacitance in a capacitor-supported system," IEEE Trans. Power. Electron., vol. 29, no. 3, pp. 1163–1175, Mar. 2014.

ISSN (online): 2446-1636
ISBN (online): 978-87-7210-096-8

AALBORG UNIVERSITY PRESS